Magnetotransport in two-dimensional electron systems in high Landau levels

A THESIS
SUBMITTED TO THE FACULTY OF THE GRADUATE SCHOOL
OF THE UNIVERSITY OF MINNESOTA
BY

Xiaojun Fu

IN PARTIAL FULFILLMENT OF THE REQUIREMENTS
FOR THE DEGREE OF
Doctor of Philosophy

Advisor: Michael Zudov

Nov, 2021

Acknowledgements

Over the years at University of Minnesota, I have been fortunate to have numerous support from too many people to list, who not only contributed to the work in this thesis, but also helped me become the person that I am.

First and foremost, I thank my advisor Michael Zudov for his outstanding mentorship. I am grateful for his generous guidance. He encouraged me to ask questions but answered my questions by asking more questions until I found the path. From many questions, good or stupid, he guided me how to unmask the puzzles with critical reasoning and creativity. Benefiting from his guidance, I started to build the intuitions knowing which paths to try when confronted a problem, and when to abandon the path and when to keep moving. Working with Michael, I was touched by his great passion and persistence in getting deep in the field. I am also thankful for the opportunities that he gave me to interact with many great physicists working on a broad range of research, from which I broadened my vision and was able to have a view perhaps not limited to a typical prospective of a graduate student. Outside the physics, Zedong and I enjoyed the hangouts with Anna and Michael, and we liked their fun stories and loved the best borscht in the world that Anna made.

I am grateful to the support and encouragement of the other members of my dissertation committee, Vlad Pribiag, Alex Kamenev, and Joseph Talghader. I was inspired by Vlad at many aspects, directly and indirectly, throughout my entire graduate career. He is an inspiration for the integration of kindness and humility, breadth of knowledge, and thoughtfulness in both physics and life. I am grateful for his generous help especially many times I asked in the last minutes. From Alex's class, I broadened my views and learnt a large part of the advanced condensed matter outside my own field. I am

thankful to Alex and Joey for being in my pre-oral and final-oral committees, for always helpful and uplifting conversations, and for their support throughout my graduate studies.

I was fortunate to collaborate with Boris Shklovskii in two research projects. I was touched by his unlimited passion exploring the problems and the kid-like happiness whenever any progress was made. I was also inspired by his distinguished creativity to jump out of the standard pictures and view the problems from a slight offbeat prospective. I thank Yi Huang and Michael Sammon for their efforts in bridging the theories and experiments, and for together sharing the frustrations and excitements.

I collaborated with Qianhui Shi on most of my PhD projects. I joined the group during Qianhui's almost final year as a PhD student. She was a great mentor guiding me everything from how to use lock-in amplifiers to how to give a good talk. Later on when she was a postdoc at Columbia, luckily we continued our collaborations. It was fun to dig deep into her thesis and notebooks. I also appreciate that our work friendship extends to the personal life. I thank all members in Zudov's lab, Quentin Ebner, Mikhail Borisov, Austin Riedl, Brendan King, Haoyue Sun, and Elliot Bell for carrying on the work together.

I thank Kirk Baldwin, Edwin Chung, Geoff Gardner, Michael Manfra, Loren Pfeiffer, Qi Qian, John Watson, and Ken West, for their efforts in improving sample quality, which made the work in this thesis possible and led to the progress of the whole field. I appreciate the team at National High Magnetic Field Laboratory, especially Hongwoo Baek, Ali Bangura, Elizabeth Green, Glover Jones, and Ju-Hyun Park, for their kind technical support.

I appreciate the friendly and supportive environment in the department of physics at University of Minnesota. I thank the Head Paul Crowell and the Director of Graduate Studies Jorge Vinals for their efforts in making the department even better. I am especially grateful to Paul for his supportive guidance and wise thoughts during the time I cannot find a path. I thank Kristina Cibuzar, Shelley Frankel, Tina Garofolo, Amanda Hawkinson, Jennifer Kroschel, Julie Murphy, Amy Nordlander, and Mette Stewart for their efforts in making administrative process always run smooth. I thank Bill Voje and Michael Rother for their training and support in machine shop and nitrogen/helium filling. I thank Chad Sullivan for his expert help on IT. As an experimental student

who actually spent most of the time in the office, I thank Alex Hamill and Xi Zhang for being wonderful office mates. I enjoyed the discussions with Xinxin Cai when she was a postdoc at UMN. I felt it fortunate that our friendship extended from office to life. I thank Raymond Co, Alex Hamill and Zedong Yang for their help on proofreading this thesis. I am grateful to too many senior peers, who paved the road and generously shared their precious experience.

I thank Russ Funk for providing the opportunity of working on the topological data analysis projects and for encouraging me to explore beyond what I thought I was capable of. Working with him opened my visions and I was surprised to see the similarities rooting in the math and logical reasoning between physical sciences and social sciences. Moreover, it was enjoyable and impressing experience in watching how Russ led the group with members coming from completely different backgrounds, and sparked everyone's expertise to make the team stronger. More than that, facing the crazy life as a young professor, Russ wears a super friendly face full of humanity, empathy and kindness. I thank him for providing the role models, both personal and professional, and I hope I have learnt a little bit from him. I thank Tom Gebhart for leading the project and for inspiring me with his creativity, smartness, code cleanness and solid math skills.

Finally, I thank all my dear friends for their support. Special thanks to Tianqi Li for her companion along the entire journey. I am grateful to my parents for their efforts in educating me, and for always encouraging me to explore and pursue the life that I want to live and the person that I want to be. I thank my cousin Hechen for her support and for providing a role model since I was a kid. I thank Zedong for being with me in my life. I am always able to view science, history, and life from a unique prospective during our talks. On the life trails we have together hiked, some are smooth like the parks in the Twin Cities, and some are truly difficult but rewarding like the mountains in Bagnères-de-Luchon. With him, life was never boring when it was featureless, and was always filled of courage even if sometimes it seemed endless full of clouds.

Dedication

To everyone who has the faith and courage to hold onto the goodness in themselves and in each other [1]

[1] Adapted from Chloe Zhao's acceptance speech for the Best Director Oscar

Abstract

The field of condensed matter physics explores the macroscopic and microscopic properties of matter that makes up most of the usual (and unusual) stuff that surrounds us every day. Since the discoveries of integer and fractional quantum Hall effects [1, 2] (Nobel Prizes 1985 and 1999), quantum transport in two-dimensional (2D) carrier systems subjected to low temperatures and magnetic fields has become a fundamental branch in condensed matter physics, intriguing quantum phases arising from the strong electron-electron interaction. Thanks to the advances in nanostructure growth techniques, devices with unparalleled quality allow for new experimental observations and the exploration of the underlying physics. Among many fascinating discoveries, in this thesis, we focus on magnetotransport in 2D electron systems at high Landau levels, specifically the broken-symmetry states [3, 4, 5, 6] at $N \geq 2$ Landau levels, and emergent transport phenomena at weak magnetic fields when the systems are exposed to microwave radiation [7, 8].

I organize the thesis into three parts. The first part includes Chapter 1, where we briefly introduce the fundamentals of magnetotransport in 2D electron systems. The second part includes Chapter 2, Chapter 3, and Chapter 4, where we focus on the transport in the quantum Hall stripe and bubble regimes. More specifically, we introduce our contribution to the experimental observations of three new quantum states. The third part includes Chapter 5 and Chapter 6, where we focus on the experiments related to microwave-induced resistance oscillations (MIRO). We show that MIRO gives us access to several physical parameters and understanding the underlying mechanisms. We summarize each chapter respectively as below.

Chapter 1 briefly introduces the fundamentals of magnetotransport in 2D electron systems. We review how to realize a clean two-dimensional electron gas in a GaAs quantum well and how to quantify the quality of a two-dimensional electron gas. Then we introduce the integer and fractional quantum Hall effects, the hallmarks of quantum Hall families. Finally, we review previous theoretical and experimental studies on the quantum Hall stripes and bubbles at $N \geq 2$ Landau levels and microwave-induced resistance oscillations at very high Landau levels.

Chapter 2 reports on transport signatures of eight distinct bubble phases in the $N = 3$ Landau level of a $Al_xGa_{1-x}As/Al_{0.24}Ga_{0.76}As$ quantum well with $x = 0.0015$. These phases occur near partial filling factors $\nu^\star \approx 0.2\,(0.8)$ and $\nu^\star \approx 0.3\,(0.7)$ and have $M = 2$ and $M = 3$ electrons (holes) per bubble, respectively. We speculate that a small amount of alloy disorder in our sample helps to distinguish these broken symmetry states in low-temperature transport measurements.

Chapter 3 reports on transport signatures of hidden quantum Hall stripe (hQHS) phases in high ($N > 2$) half-filled Landau levels of $Al_xGa_{1-x}As/Al_{0.24}Ga_{0.76}As$ quantum wells with varying Al mole fraction $x < 10^{-3}$. Residing between the conventional stripe phases (lower N) and the isotropic liquid phases (higher N), where resistivity decreases as $1/N$, these hQHS phases exhibit isotropic and N-independent resistivity. Using the experimental phase diagram, we establish that the stripe phases are more robust than theoretically predicted, calling for improved theoretical treatment. We also show that, unlike conventional stripe phases, the hQHS phases do not occur in ultrahigh mobility GaAs quantum wells but are likely to be found in other systems.

Chapter 4 reports the experimental observations on anomalous nemetic states in high half-filled Landau levels. It is well established that the ground states of a two-dimensional electron gas with half-filled high ($N \geq 2$) Landau levels are compressible charge-ordered states, known as quantum Hall stripe (QHS) phases. The generic features of QHSs are a maximum (minimum) in a longitudinal resistance R_{xx} (R_{yy}) and a non-quantized Hall resistance R_H. Here, we report on emergent minima (maxima) in R_{xx} (R_{yy}) and plateau-like features in R_H in half-filled $N \geq 3$ Landau levels. Remarkably, these unexpected features develop at temperatures considerably lower than the onset temperature of QHSs, suggesting a new ground state. Moreover, we demonstrate that a modest in-plane magnetic field, applied either along $\langle 110 \rangle$ or $\langle 1\bar{1}0 \rangle$ crystal axis of GaAs, destroys anomalous nematic states and restores quantum Hall stripe phases aligned along their native $\langle 110 \rangle$ direction. These findings confirm that anomalous nematic states are distinct from other ground states and will assist future theories to identify their origin.

Chapter 5 investigates how MIRO evolve with the carrier density n_e in a GaAs/AlGaAs quantum well equipped with an *in situ* grown back gate, an aspect which has not been previously explored. First, we show that the MIRO frequency monotonically decreases

with n_e. This finding can be linked to the renormalization of the effective mass by electron-electron interactions, which are sensitive both to n_e and to quantum confinement of our 2DEG. Second, we find that the MIRO amplitude substantially increases with n_e. Our analysis shows that the anticipated increase in the effective microwave power and quantum lifetime with density is *not* sufficient to explain the observed growth of the amplitude. We further observe that the fundamental oscillation extrema move towards cyclotron resonance with increasing density, which also contradicts theoretical predictions. These unexpected findings reveal that the density dependence is not properly captured by existing theories, calling for further studies.

Chapter 6 studies the effect of illumination on the quantum lifetime in GaAs quantum wells. Low-temperature illumination of a two-dimensional electron gas in GaAs quantum wells is known to greatly improve the quality of high-field magnetotransport. The improvement is known to occur even when the carrier density and mobility remain unchanged, but what exactly causes it remains unclear. Here, we investigate the effect of illumination on microwave photoresistance in low magnetic fields. We find that the amplitude of MIRO grows dramatically after illumination. Dingle analysis reveals that this growth reflects a substantial increase in the single-particle (quantum) lifetime, which likely originates from the light-induced redistribution of charge enhancing the screening capability of the doping layers.

Contents

List of Tables

List of Figures

Chapter 1

Introduction: fundamentals of magnetotransport in two-dimensional electron systems

Low-dimensional electron physics is an important field in condensed matter physics that provides an exceptional platform for exploring electron-electron interactions. In particular, two-dimensional electrons confined to GaAs quantum wells are hallmark platforms, due to their nearly defect-free nature coming from the lattice match between AlAs and GaAs and the development of molecular beam epitaxy techniques. Section 1.1 briefly introduces the structure of a modern GaAs quantum well, whose cleanliness nature allows exploration of the underlying physics. To date, only one residual impurity exists for every 10^{10} Ga/As atoms on average [9]. Section 1.2 introduces the metrics to quantify the quality of a two-dimensional electron gas (2DEG). Sections 1.3, 1.4 and 1.5 focus on the magneto-transport in the quantum Hall families. Specifically, we introduce the hallmark integer and fractional quantum Hall effects in Section 1.3, the quantum Hall stripe and bubble phases in Section 1.4, and the microwave-induced resistance oscillations (MIRO) in Section 1.5, where the quantum Hall stripe and bubble phases and MIRO two are the fields which my PhD research focuses on.

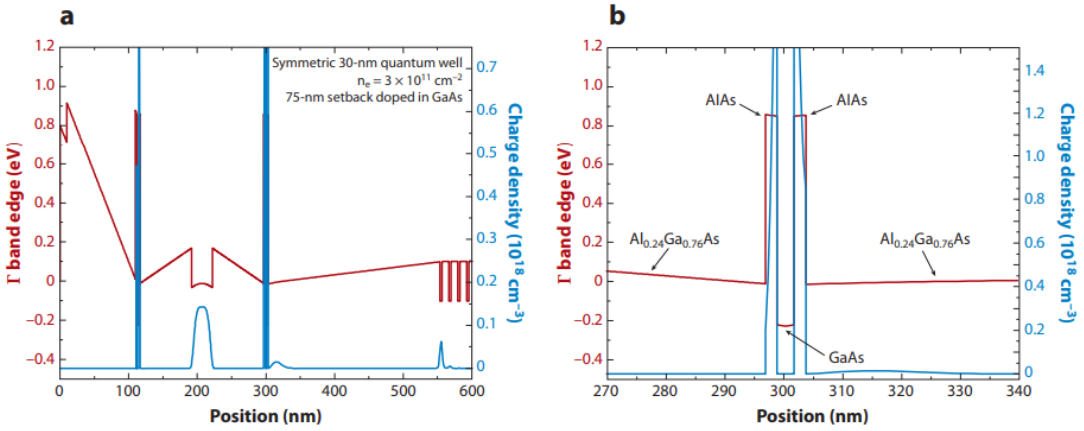

Figure 1.1: Band edge and charge density profiles in a GaAs quantum well. (a) A two-dimensional electron gas resides in a 30 nm GaAs quantum well confined by $Al_{0.24}Ga_{0.76}As$ barriers. The silicon impurities are in the center of a narrow 3 nm GaAs well and sandwiched by 2 nm of AlAs. (b) Γ point conduction band edge and free charge density in the immediate vicinity of the doping well. The figure is taken from Ref. [10].

1.1 A two-dimensional electron gas in a modern GaAs quantum well

Figure. 1.1 shows an example of band edge and charge density profiles in an ultra-high mobility GaAs quantum well. GaAs has a smaller band gap and lower conduction band energies than those of AlGaAs, and thus it forms a quantum well. The conducting carriers come from the donors. In early investigations, Si was doped into the AlGaAs barriers so that electrons in the GaAs quantum well experience a weak scattering potential from ionized donors. However, in modern devices, the silicon dopant atoms are placed in extremely narrow (3-nm) GaAs doping wells sandwiched by 2-nm pure AlAs barriers as shown in Figure. 1.1(b). Charge is transferred not only to the primary two-dimensional electron gas in the 30-nm GaAs quantum well, but also to the X point band edge of AlAs barriers. The heavy-mass X electrons exhibit a low mobility and therefore are expected to contribute less to the parallel conductance [11]. With an appropriate doping amount, they do not appear as a parallel conduction in the magnetotransport [10]. There are two main advantages of the doping well design. First, it is well known that the exchange of Al and Si atoms will lead to the formation of DX centers, which

act as additional scatterers [12]. Given that the silicon atoms are placed in GaAs, not AlGaAs, there are no associated DX centers. Second, the excess carriers in AlAs barriers still play an important role, presumably screening the potential of the parent ions [11, 10].

1.2 Quality of 2DEG

A conventional metric to evaluate the quality of a 2DEG is the electron mobility. In the field of the low temperature physics, mobility at 0.3 K is a basic measure for the initial examination [10]. Described by the Drude model, electrons are accelerated by an electric field E and then scattered by an impurity after a mean free time τ, which is also known as the transport scattering time. The electron mobility can be obtained from the (Drude) resistivity ρ_0 as

$$\mu = \frac{1}{e\rho_0 n_e} = \frac{e\tau}{m^\star}\,, \tag{1.1}$$

where e is electron charge, $m^\star$ is effective mass, n_e is electron density which can be obtained from classical Hall resistance $\rho_{\rm H}$ with a low magnetic field B,

$$\rho_{\rm H} = B/n_e e\,. \tag{1.2}$$

Considering an electron is scattered by an impurity from an initial state $\mathbf{k}$ to a final state $\mathbf{k}+\mathbf{q}$, which have an angle θ between two states on the Fermi surface and a scattering probability $|V_q|$, as shown in Figure. 1.2, τ can be defined as [13]

$$\frac{1}{\tau} = \frac{m^\star}{\pi\hbar^3}\int_0^\pi |V_q|^2.(1-\cos\theta)d\theta \tag{1.3}$$

The magnitude of the wave vector before the collision $|q|$ is the same as that after the collision $|k+q|$ due to energy conservation. Thus one has a wave vector $q = 2k_F\sin(\theta/2)$ where the 2D Fermi wave vector $k_F = \sqrt{2\pi n_e}$. Since small-angle scattering has a reduced weight due to the factor of $(1-\cos\theta)$ in the integral, we notice that mobility is particularly sensitive to large-angle scattering. This is also easy to understand from the physics picture: backscattering with $\theta = \pi$ has a much larger effect on current than small-angle scattering.

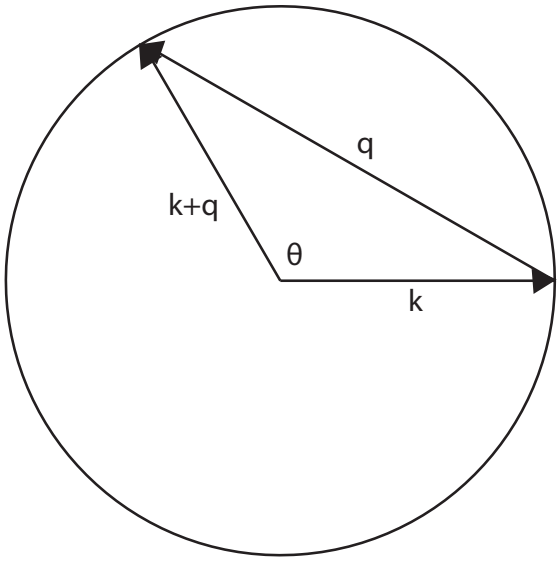

Figure 1.2: Illustration of an electron scattered by an impurity from an initial state $\mathbf{k}$ to a final state $\mathbf{k} + \mathbf{q}$ with angle θ between two states on the Fermi surface.

Mobility is straightforwardly obtained in experiments through measurement of the longitudinal and Hall resistivities in the van der Pauw contact geometry. High mobility corresponds to minimal electron scattering, which is essential in studies of many-body electron phases. To date, electron mobility values as high as $\mu \approx 44 \times 10^6$ cm^{2}V^{-1}s^{-1} have been observed in GaAs 2DEG with densities near $n_e \approx 2 \times 10^{11}$ cm^{-2} [9].

Although mobility is a useful metric for initial sample characterization, its correlation to the transport quality at high magnetic fields is not strong. For example, in 1990, in a $\mu \approx 7 \times 10^6$ cm^{2}V^{-1}s^{-1} sample, the energy gap at filling factor $\nu = 5/2$ was measured to be 105 mK; in 1999 in a $\mu \approx 17 \times 10^6$ cm^{2}V^{-1}s^{-1} sample with the same electron density and heterostructure design, the gap was still only 110 mK [14, 15]. Consequently, the 5/2 excitation gap was considered to be an important metric for magnetotransport at high magnetic fields. To date, the highest ever measured 5/2 excitation gap is 820 mK with a sample mobility of around 44 million [9].

However, magnetotransport in low magnetic fields, such as Shubnikov-de Haas oscillations (SdHO) and MIRO, may be insensitive to both low-temperature mobility and excitation gap. In such cases, the quantum (total) lifetime τ_{q} which determines the

broadening of energy levels such as Landau levels, is considered as an appropriate metric. The quantum lifetime is defined as [13]

$$\frac{1}{\tau_{\mathrm{q}}} = \frac{m^\star}{\pi\hbar^3}\int_0^\pi |V_q|^2 d\theta. \tag{1.4}$$

The quantum lifetime contains an equally weighted sum over all scattering processes. Small-angle scattering counts as much as backscattering in the quantum lifetime. Thus, it is sensitive to electron-remote impurity scattering. In chapter 6, we will discuss how to examine the effect of illumination on the sample quality by examining the change of the quantum lifetime employing MIRO.

1.3 Hallmark: the integer and fractional quantum Hall effect

1.3.1 Landau quantization

In the condition of $\omega_{\mathrm{c}}\tau \gg 1$ where ω_{c} is cyclotron frequency, the transport cannot be accurately described by the Drude theory as the quantum-mechanical effects become significant. In a physical picture, it can be illustrated as below. When $\omega_{\mathrm{c}}\tau \gg 1$, an electron can make many revolutions before being scattered by an impurity. This leads to appreciable self-interference such that the electron's wavelike nature must also be taken into account.

We first review Landau quantization of the electron energy spectrum in a magnetic field, which is a quantum description of 2D systems and gives rise to the complicated transport phenomena in the quantum Hall family. In the Landau gauge, the electromagnetic vector potential $\hat{A} = (0, Bx, 0)$, where $\hat{B} = B\hat{z}$ is the magnetic field pointing in the $\hat{z}$ direction, the Hamiltonian can be separated into H_z and H_{xy}. The eigenvalue in the z-direction leads to bound states independent of magnetic fields. On the other hand, H_{xy} is independent of the confinement potential but dependent on the magnetic fields, written as,

$$H_{xy} = \frac{(p_y + eBx)^2 + {p_x}^2}{2m^\star}. \tag{1.5}$$

By solving the Schrodinger equation, the energy spectrum is given by

$$E_N = \hbar\omega_{\mathrm{c}}(N + 1/2), \tag{1.6}$$

where $N = 0, 1, 2, ...$ and $\omega_c = eB/m^\star$ is the cyclotron frequency. The energy spectrum consists of equally-spaced levels called Landau levels (LLs), which are separated by $\hbar\omega_c$. From the spectrum, we can see the analog between a 2D electron in a magnetic field and a one-dimensional harmonic oscillator. Each LL can accommodate as many electrons as magnetic flux quanta $\phi = h/e$ penetrating the sample. The degeneracy, the number of states per unit area per spin in each LL, is given by

$$n_B = \frac{B}{\phi} = \frac{eB}{h}\,. \tag{1.7}$$

Accordingly, the filling factor ν, denoting how many LLs are filled with electrons, is defined as,

$$\nu = \frac{2E_F}{\hbar\omega_c} = \frac{n_e}{n_B}\,. \tag{1.8}$$

Another important fact is that spins of the electrons interact with the magnetic field. A Zeeman splitting is generated in each LL. The Zeeman energy is defined as $E_z = g\mu_B B$ where the g-factor $g = 0.44$ in GaAs, and μ_B is the Bohr magnon. Although Zeeman splitting is much smaller than the cyclotron gap, there is a essential spin gap associated due to the many-body physics. As a result, at large enough magnetic fields, electrons within each LL are generally spin-polarized. Also, in reality, instead of being delta functions, LLs are broadened due to the quantum fluctuations induced by thermal effects and disorder.

We summarize the Landau quantization in 2D systems in the schematic shown in Figure. 1.3. At zero magnetic fields, the density of states (DOS) per spin per unit area is a constant of energy $\nu_0 = m^\star/2\pi\hbar^2$. In the presence of magnetic fields, the energy spectrum splits into equally-spaced LLs with further splitting due to Zeeman energy splitting. When increasing magnetic fields, the degeneracy increases and the filling factor decreases.

In low magnetic fields, the disorder-induced broadening of the LLs starts to dominate and thus LLs start to overlap. In the limit of overlapping LLs, the DOS at energy ε can be approximated by cosine functions

$$\nu_\varepsilon = \nu_0[1 - 2\lambda\cos(2\pi\varepsilon/\hbar\omega_c)]\,, \tag{1.9}$$

where $\lambda = \exp(-\pi/\omega_c\tau_q)$ is the Dingle factor and τ_q is the quantum lifetime.

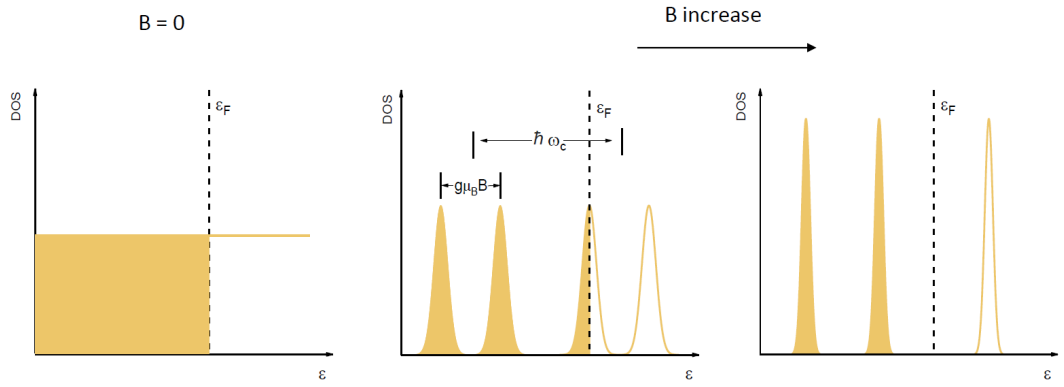

Figure 1.3: An illustration of Landau quantization in 2D systems. In the absence of magnetic fields, the DOS in 2DEG is a constant. With increasing magnetic fields, the energy spectrum splits into equally-spaced Landau levels with energy spacing $\hbar\omega_c$ with further splitting due to Zeeman energy splitting. The figure is taken from Ref. [16].

Another way to describe DOS is modeling it by a Gaussian train

$$\nu_\varepsilon = \frac{\nu_0}{\sqrt{2\pi}\gamma} \sum_{N=0}^{\infty} \exp[-\frac{(\varepsilon/\hbar\omega_c - N - 1/2)^2}{2\gamma^2}] \,. \tag{1.10}$$

Here, $\gamma = \sqrt{1/2\pi\tau_q\omega_c}$ is the width of the Laudau level scaled by Landau spacing, which determines whether LLs are separated or overlapped.

The oscillations of the longitudinal resistivity $\delta\rho$ with the magnetic field are known as Shubnikov-de Haas oscillations (SdHO). They are a prime example of magneto-resistance oscillations originated from Landau quantization in a low magnetic field. SdHO are periodic in $1/B$ and can be expressed as

$$\delta\rho = -4\rho_0\lambda(X_T/\sinh X_T)\cos(2\pi E_F/\hbar\omega_c) \,. \tag{1.11}$$

Here $X_T = 2\pi^2 k_B T/\hbar\omega_c$, known as the T-damping factor, reflects smearing of the Fermi distribution. k_B is the Boltzmann constant and T is the temperature. ρ_0 is the resistivity at zero magnetic field. The oscillations are reflective of the detuning between the Fermi energy E_F and the cyclotron energy $\hbar\omega_c = \hbar eB/m^\star$. The minima of oscillations occur at $E_F/\hbar\omega_c = N$, where N is an integer. SdHO can be used to extract the 2D electron density, effective mass and quantum lifetime of a sample.

1.3.2 The integer quantum Hall effect

The discovery of the integer quantum Hall effect was first observed by Klaus von Klitzing in 1980. With silicon-based metal-oxide-semiconductor field-effect transistor (MOSFET) samples, the Hall resistance was measured to be exactly quantized. Figure. 1.4 shows the original data of the first observation of integer quantum Hall effect. As n_e varies around integer filling factors $\nu = N$, the longitudinal resistance R_{xx} vanishes, and the Hall resistance R_H is quantized to h/ie^2, where i is a positive integer. This is contradicted from the Drude theory where R_{xx} is constant and $R_H = B/n_e e$. The von Klitzing constant $R_{\mathrm{K}} = h/e^2 = 25812.807\ \Omega$ was defined for use in resistance calibrations worldwide in 1990. In 2018, the General Conference on Weights and Measures decided to fix exact values of h and e, where R_{K} is fixed to be 25812.80745... Ω.

The discovery of the integer quantum Hall effect has triggered a large variety of theoretical approaches to understand the underlying physics and to understand the microscopic details. We first view it from the perspective of Landau quantization, which is the basis of 2D quantum transport. Naively, if we compare the Hall resistance observed in the integer quantum Hall effect $R_H = h/ie^2$ with the Hall value in the Drude theory $R_H = B/n_e e$, we obtain $n_e = B\nu e/h$, which is the density of electrons required to fill the ν-th Landau levels, see Eq. (1.8). The vanishing longitudinal resistance can also be thought of in this picture, naively. As shown in Figure. 1.3, the energy gap between separated LLs is $\hbar\omega_{\mathrm{c}}$. If the sample is clean enough that LLs are not broadened too much, and the temperature is low enough that $k_B T \ll \hbar\omega_{\mathrm{c}}$, the states are empty inside the gap. Electrons have nowhere to move and the system behaves like an insulator. Thus the transport lifetime $\tau \to \infty$ and $R_{xx} = 0$.

However, the above explanation is a naive mix of a quantum picture and a classical picture. There are a couple of questions which were not captured. One is the importance of modes at the edge of the system; the other is the role of disorder. First, we discuss the edge modes. From a classical view, as shown in Figure. 1.5, electrons move in circles in a magnetic field. Near the edges of the sample, the electrons collide with the boundary and bounce back. Consequently electrons move in one direction on one side of the sample, and in the other direction on the other side of the sample. Thus the electrons have opposite velocities on the two sides, which results in the vanishing net current in the absence of an electric field.

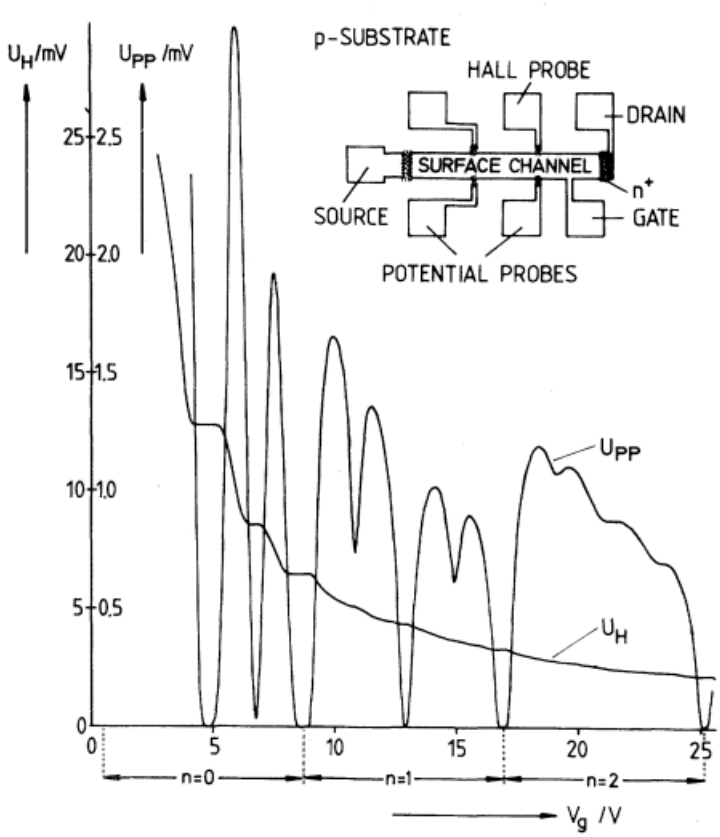

Figure 1.4: The first observation of the integer quantum Hall effect. At the integer filling factors, the longitudinal resistance reaches zero and the Hall resistance is quantized at plateaus. The figure is taken from Ref. [1].

From the quantum-mechanical view, to describe the states at the sample edge in high magnetic fields a confinement potential in the x-direction $V(X)$ is introduced in Eq. (1.5). The new Hamiltonian is described as

$$H = \frac{(p_y + eBx)^2 + {p_x}^2}{2m^\star} + V(x). \tag{1.12}$$

If $V(x)$ is smooth over the magnetic length, one can do a Taylor expansion on the potential around its location X. Neglecting the constant term and dropping the quadratic and higher terms, a drift velocity in the y-direction is given by,

$$v_y = -\frac{1}{eB}\frac{\partial V}{\partial x}. \tag{1.13}$$

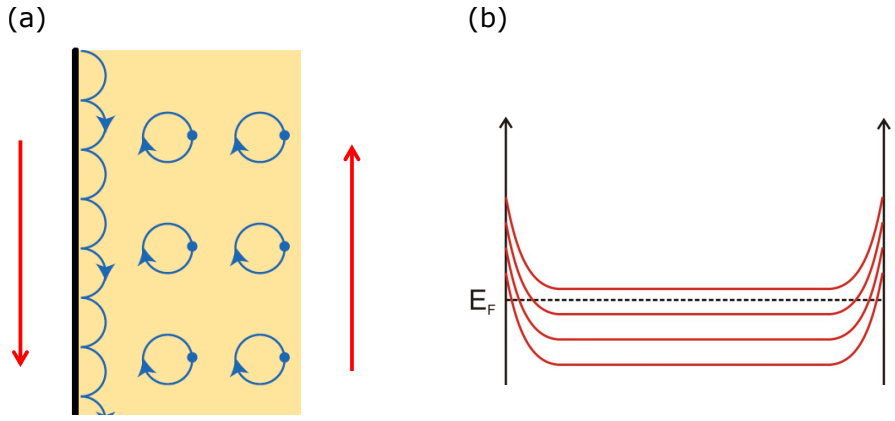

Figure 1.5: (a) Illustration on electrons moving in the circles in the magnetic fields. Chiral modes form on the edges. (b) A view of LL dispersion along x direction. Edge states accounted for the conductance are at the intersections of Fermi energy.

Indeed, this agrees with the classical result of skipping orbits, that the modes at each edge are both chiral, travelling in the opposite directions, $v_y > 0$ on the left and $v_y < 0$ on the right.

By introducing a potential difference $\Delta\mu$ on the two sides of the sample, i.e., more states on the right edge than the left edge, the current can be computed by summing over all filled states,

$$I_y = -e \int \frac{dk}{2\pi} v_y(k) = \frac{e}{2\pi\hbar}\Delta\mu. \tag{1.14}$$

The Hall voltage $V_H = \Delta\mu/e$, yields the Hall conductivity $\sigma_{xy} = e^2/h$, consistent with the expected Hall conductivity for a single LL. In a similar way, one can generalize the theory to multiple LLs, as long as E_F lies between LLs.

Finally, we briefly discuss the role of disorder. Disorder broadens the LLs and turns parts of the quantum states from extended to localized. Here, an extended state is spread throughout the whole system, and a localized state is restricted to lie in some region of space. In the localized states, electrons are trapped close to the extrema in the disorder landscape and therefore they cannot move throughout the sample. Only extended states contribute to the conduction, which is known as the bulk model.

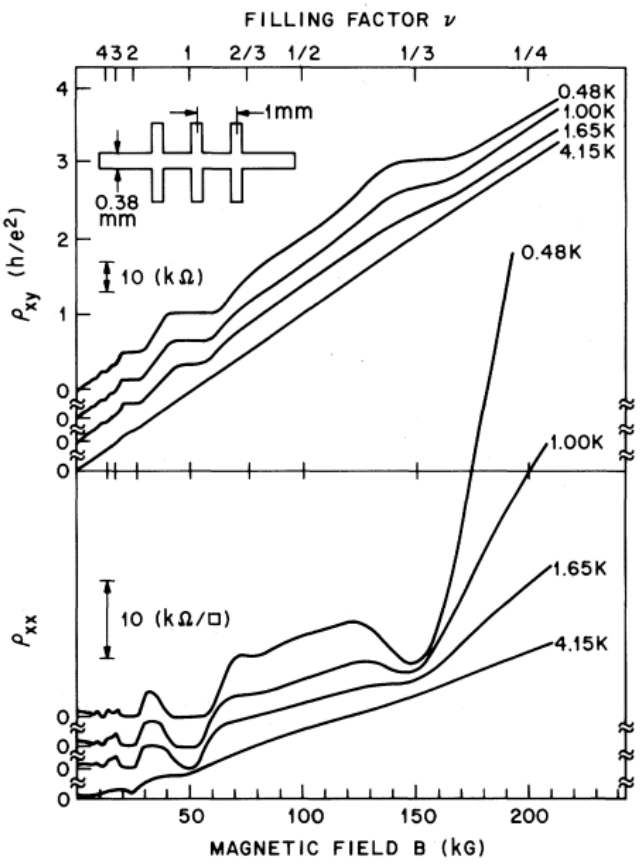

Figure 1.6: The first observation of the fractional quantum Hall effect. The Hall resistance was observed to be quantized at $\nu = 1/3$. The figure is taken from Ref. [2].

1.3.3 The fractional quantum Hall effect

Another milestone of quantum Hall physics is the discovery of the fractional quantum Hall effects, observed in a GaAs/AlGaAs heterostructure, by D. Tsui, H. Stormer and A. Gossard [2]. The same as the integer quantum Hall effect, the fractional quantum Hall effects was first discovered in experiments rather than predicted in theories. In the first measurement of the fractional quantum Hall effects, as shown in Figure. 1.6, the Hall resistance was observed to be quantized at $\nu = 1/3$. To date, the fractional quantum Hall effects has been observed at many filling factors ν, e.g., $\nu = 1/5, 2/5, 3/7, 4/9, ...$ and in many systems, including GaAs [2], Si [17, 18], AlAs [19], GaN [20], graphene [21, 22], CdTe [23], ZnO [24], Ge [25], and InAs [26].

The key difference between the integer and fractional quantum Hall effects is that the interactions between electrons play a significant role in the fractional quantum Hall effect. This is because in a high magnetic field, other LLs do not play roles, and kinetic energy is a constant for all the electrons and thus irrelevant. Laughlin described the physics at filling fractions $\nu = 1/m$ where m is an odd integer, giving the first approach to the fractional quantum Hall effects [27]. He proposed that the ground state wavefunction is

$$\varphi = \prod_{i<j}(z_i - z_j)^m e^{-\sum_{i=1}^{n}|z_i|^2/4l_B^2}, \tag{1.15}$$

where z is the position of electron in the complex notation, m is an odd integer to preserve the anti-symmetry, and l_B is the magnetic length. On one hand, when two electrons are close to each other, the prefactor vanishes with a zero of order m. On the other hand, the exponential factor, which corresponds to the ground state wave function of non-interacting electrons in a magnetic field, decreases quickly when the electrons get too far away from the origin. Thus the wavefunction takes a delicate balance of those two two effects. If the free electron travels on a closed path around one of the fixed electrons, the phase is changed by $2\pi/\nu$. One important insight from Laughlin theory is that the quasi-particle excitation at $\nu = 1/m$ carries the fractional charge $q = -|e|/m$, which gives rise to the fractional quantized Hall resistance.

Another view of fractional quantum Hall effects, composite fermions, was motivated by understanding the deep connection between the integer and fractional quantum Hall effects [28]. It was developed by J. K. Jain. Here we briefly introduce its intuition. We consider the following process. First, we begin with an integer quantum Hall state at $\nu = n$; and then, we convert electrons into composite fermions by attaching $2p$ magnetic flux quanta to each electron, where $2p$ is the number of vortices; finally, we obtain the electrons back by spreading the attached flux. If the gap does not close during the flux smearing process, a fractional quantum Hall state is produced at the filling factor,

$$\nu = n/(2pn \pm 1). \tag{1.16}$$

A large majority of the observed fractional quantum Hall states correspond to the integer quantum Hall states of composite fermions. Recently, a rich pattern of the fractional quantum Hall states in graphene double layers can be explained in terms of two-component composite fermions carrying both intra- and inter-layer vortices [29, 30].

The fractional quantum Hall effect can also be viewed from the perspective of edge channels developed by C. W. J. Beenakker and A. H. MacDonald in 1990 [31, 32]. At the edges of the sample, the electron density is reduced due to the increase in electrostatic potential energy. In the regions where electron gas has fractional filling factors, the potential gradient is small. The energy gap forms, associated with the formation of incompressible bands of fractional filling factor, which are alternating with the edge channels. The fractional quantized Hall resistance arises from applying this picture to the edge model described in the integer quantum Hall effect section.

1.4 Broken symmetry states at $N \geq 2$ Landau levels

1.4.1 Quantum Hall stripes

An anisotropic liquid crystal phase was first theoretically predicted in a clean 2DEG at half-filled LLs ($N \geq 2$) by A. A. Koulakov, M. M. Fogler, and B. I. Shklovskii in 1996 [3, 4]. By performing the Hartree-Fock analyses, they found ground states consisting of complex charge density wave (CDW) states at partially filled LLs due to a peculiar boxlike screened Coulomb potential. At half-filled LLs, the system forms equal-width stripes of alternating filling factors. For example, at $\nu = 9/2$, the system can be viewed of an alternation of $\nu = 4$ and $\nu = 5$. The periodic spacing of alternating stripes was calculated to be of the order of cyclotron radius. For example, at $\nu = 9/2$, the stripe periodic spacing $\lambda \sim 100$ nm. The Hartree-Fock theory is known to be exact for large values of the orbital LL index $N \gg 1$ and it is thought to hold for $N \geq 2$. Quantum fluctuations in the ground and first excited LLs destroy CDW order, which is confirmed by the experiments.

Three years later, in 1999, quantum Hall stripes (QHS) were confirmed by experiments by two groups, M. P. Lilly et al., and R. R. Du et al. [5, 6]. As shown in Figure. 1.7, magnetotransport along two orthogonal directions shows a great anisotropy identified by a peak in R_{xx} and a dip in R_{yy} at half-filled filling factors $\nu = 9/2, 11/2, 13/2, ...$ We note that the Hall resistance is not quantized in the broken symmetry states. The anisotropy was observed under $T = 100$ mK. Given that the large-resistance direction lies along the $\langle 1\bar{1}0 \rangle$ direction, the stripes were identified to lie along the $\langle 110 \rangle$ direction. The transport along the stripes is easy, giving low resistances, and the transport across

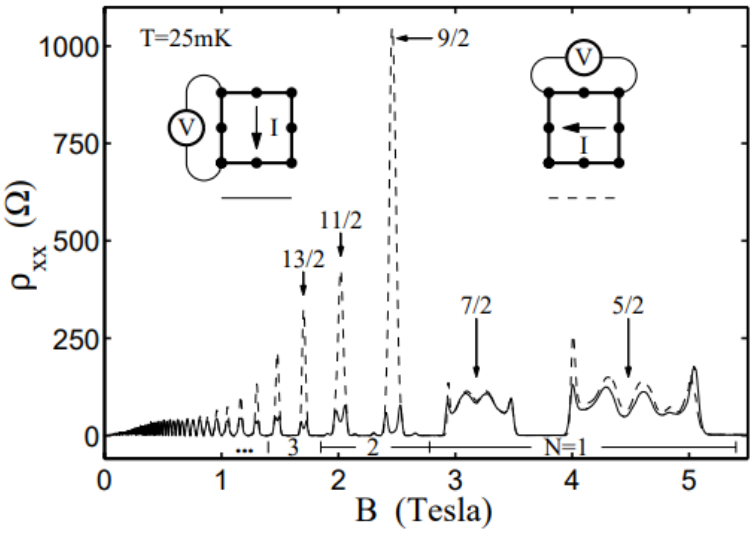

Figure 1.7: One of the first observations on quantum Hall stripes. Magnetotransport along two orthogonal directions show a great anisotropy identified by a peak in R_{xx} and a dip in R_{yy} at half-filled filling factors $\nu = 9/2, 11/2, 13/2, ...$ The figure is taken from Ref. [5].

the stripes is hard, giving high resistances. In addition to the transport measurement, anisotropy was also detected in microwave pinning resonance [33] and surface acoustic wave propagation [34, 35] experiments.

With few examples, the hard direction is almost always along the $\langle 1\bar{1}0\rangle$ direction. The only counterexamples where the hard direction switches to the $\langle 110\rangle$ direction, to date, occur in the samples with high electron density [36, 37]. However, a recent experiment shows that the hard direction is still along the $\langle 1\bar{1}0\rangle$ direction in the samples with $n_e \geq 4.0\times10^{11}$ cm^{-2} [38]. The hard direction aligning with the $\langle 1\bar{1}0\rangle$ direction indicates that a native symmetry-breaking field exists within the semiconductor heterostructure. However, after nearly two decades of research investigating the native-symmetry breaker [39, 40, 37], the origin is still mysterious.

Shortly after the discovery of quantum Hall stripes, it was realized that an in-plane magnetic field $B_{\|}$ can easily reorient stripes [41, 42] perpendicular to it. This finding was well explained by theories considering the finite thickness of the 2DEG [43, 44]. Subsequent experiments, however, revealed evidence for another mechanism

which favors parallel stripe alignment with respect to $B_{\parallel}$ [36, 45, 46, 47]. Other factors which can re-orient stripe directions include heterostructure engineering [37], minute density modulation [48], spin and charge distribution [49], mechanical strain [39], and electric current [50].

While the early Hartree-Fock theories of CDW formation in high Landau levels estimated that the CDWs would form at temperatures of a few Kelvin [3, 4], the onset temperature where transport anisotropy starts to develop in experiments is about 150 mK, which is an order smaller than the theory. Later on, it was proposed that the local stripe order may appear at high temperatures within small domains, but quantum fluctuations and disorder prevent long-range orientational order of those domains. Several possible electronic liquid crystalline states were proposed, including isotropic fluid phase, nematic phase, smectic phase, and stripe-crystal phase [51]. Further theory work strengthened the case for these phases [52]. Experiments typically detect broken rotational symmetry with a lack of broken translational symmetry. Thus nematic phases were commonly considered as the phase of the quantum Hall stripes. However, the debate on the phases is still ongoing. Experimentally, a possible nematic to smectic phase transition in a 2DEG at half-filling [53] was detected. However, recently, the agreement between the hard-to-easy resistivity ratio based on Hartree-Fock theory and the experimental data supports the conventional smectic stripe Hartree-Fock phases [54].

While it is clear that the transport anisotropy reflects the quantum Hall stripes at half-filled LLs ($N \geq 2$), is it possible that the transport can be isotropic with the formation of stripes? The answer is surprisingly yes. We will talk about the hidden quantum Hall stripes in Chapter 3.

In Chapter 4, we report on emergent minima (maxima) in R_{xx} (R_{yy}) and plateau-like features in R_H in half-filled $N \geq 3$ Landau levels which develop at temperatures considerably lower than the onset temperature of quantum Hall stripes, suggesting a new ground state.

1.4.2 Quantum Hall bubbles

As siblings of quantum Hall stripe phases, quantum Hall bubble phases occur away from half-integer fillings at $N \geq 2$ [3, 4]. The electrons form into clusters and the systems can be viewed as electron bubbles. In the limit of zero disorder, electron bubbles crystallize

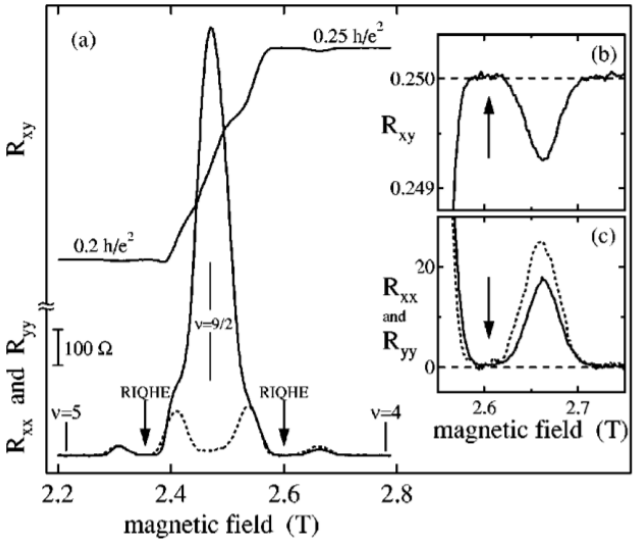

Figure 1.8: One of the first observations on quantum Hall bubbles. Near $\nu \approx 4.25$ and 4.75, both R_{xx} and R_{yy} are small, and R_H exhibits the integer QHE at $T \approx 50$ mK. The figure is taken from Ref. [57].

into a triangular lattice with a lattice constant about three times the cyclotron radius. Additional theoretical studies including exact diagonalization [55] and density matrix renormalization group (DMRG) studies [56] supported bubble formation.

Soon after the formulation of the Hartree-Fock theory, the evidence for bubbles were found in experiments [5, 6, 57]. Being pinned by disorder, such bubble crystals are insulating and the measured resistances are akin to those at the nearest integer filling factors, which are so-called Reentrant integer quantum Hall states (RIQHS). Figure. 1.8 shows one of the earliest experiments on bubbles. Near $\nu \approx 4.25$ and 4.75, both R_{xx} and R_{yy} are small, and R_H exhibits the integer QHE. The bubble phases were also supported by nonlinear transport [57, 58], pinning resonance [59, 60], onset temperature [61], surface acoustic wave [34, 35], and screening efficiency measurements [62].

Theoretically, the number of RIQHS increases with LL index, as more electrons can be accommodated in each cluster. However, the evidence for this was lacking. Indeed, the same number of RIQHS was seen both in the $N = 2$ and $N = 3$ LLs. Although it is possible that multiple bubbles phases occur in the same RIQHS, such an idea is hard

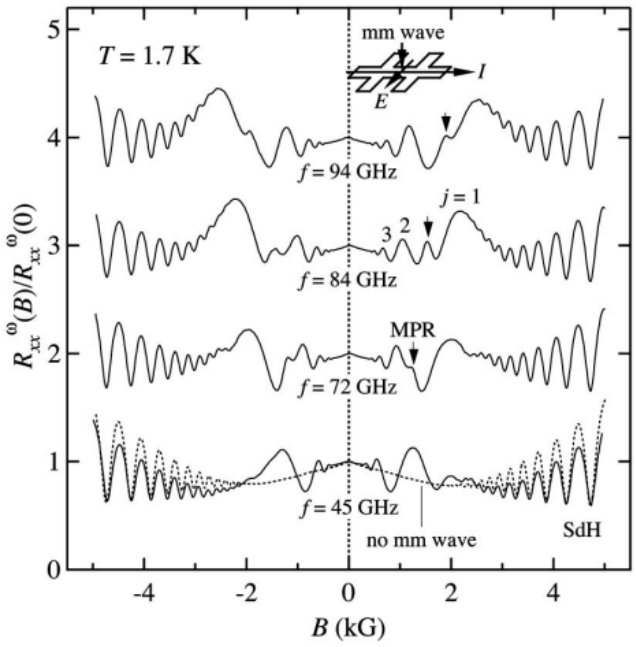

Figure 1.9: First observation on microwave-induced resistance oscillations (MIRO) in a Hall bar sample with $n_e \approx 2.0 \times 10^{11}$ cm^{-2} and the mobility $\mu \approx 3.0 \times 10^6$ cm^{2}V^{-1}s^{-1}. Magnetoresistivity with (solid lines) and without (dashed line) microwave irradiation for different frequencies $f = 45, 72, 84$ and 94 GHz, normalized to R_0 at zero magnetic field. Integers show the order of MIRO peaks. The arrows mark the magnetoplasmon resonance. The figure is taken from Ref. [7].

to test. In Chapter 2, we distinguish two- and three-electron bubbles in the $N = 3$ LL with the help of a tiny amount of short ranged alloy disorder in the quantum well.

1.5 Microwave-induced resistance oscillations in low magnetic fields

When a high mobility 2DEG is exposed to microwave radiation in the presence of a weak perpendicular magnetic field, magnetoplasmon resonance (MPR) is expected. MPR corresponds to a cyclotron resonance driven by magnetic fields. Experimentally, photoresistance oscillations termed microwave-induced resistance oscillations (MIRO) were unexpectedly observed [63, 7, 8]. Figure. 1.9 shows the first observation of MIRO

in a Hall bar sample with $n_e \approx 2.0 \times 10^{11}$ cm^{-2} and the mobility $\mu \approx 3.0 \times 10^6$ cm^{2}V^{-1}s^{-1} at several different microwave frequencies f. The microwave radiation was delivered waveguide. Integers show the orders of MIRO peaks. MPR is marked by the arrows.

MIRO were found to be periodic in $1/B$ but are controlled by the ratio of the microwave radiation frequency $\omega = 2\pi f$ to the cyclotron frequency,

$$\epsilon \equiv \omega/\omega_c. \tag{1.17}$$

The N-th order MIRO maximum $(+)$ and minimum $(-)$ can be described by [64]

$$\epsilon = \epsilon_N^{\pm} \equiv N + \delta_N^{\pm}\,, \quad \delta_N^{\pm} \approx \mp 0.25\,, \tag{1.18}$$

and the N-th zero-response node, defined by $\delta R = 0$, by

$$\epsilon = N\,. \tag{1.19}$$

MIRO are mostly observed below 1 K, are strongly suppressed with increasing T, and become almost undetectable $T = 4 - 7$ K. To date, MIRO have been observed in several 2D platforms including GaAs/AlGaAs [7, 8], Ge/SiGe [65, 66], and MgZnO/ZnO [67]. Recently, terahertz-induced magneto-oscillations was observed in graphene [68].

The most frequently used theoretical models to account for MIRO are referred to as the displacement [69, 70, 71] and inelastic [72, 73] mechanisms. We briefly introduce the physical pictures in these theoretical approaches without detailed calculations. The displacement mechanism originates from a direct modifications of electron-impurity scattering rates by microwave radiation. As shown in Figure. 1.10(a), in the presence of a small applied measurement voltage a spatial gradient is created in the energy spectrum. If an electron is initially in the n-th LL, and absorbs a microwave photon with energy $\hbar\omega$ slightly larger than $2\hbar\omega_c$, a spatial displacement of distance Δ to the right is needed to make a transition to the $(n+2)$th LL. The displacement here is the spatial shift of the electron guiding center, assisted by the momentum transfer between the electron and impurity through an elastic scattering process. This behavior results in a photocurrent flowing against dark currents, leading to a decrease in sample conductivity and a MIRO minima. In a similar manner, if a microwave photon energy $\hbar\omega$ is slightly smaller than $2\hbar\omega_c$, the displacement direction is along dark currents, leading to an increase in sample conductivity and a MIRO maxima. At $\omega/\omega_c = n$, the displacement

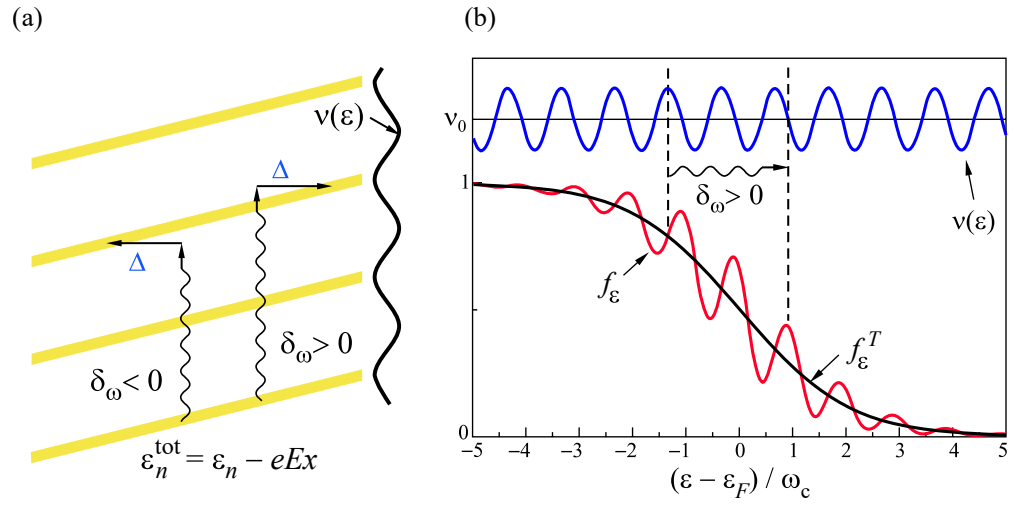

Figure 1.10: Illustration on (a) radiation-induced disorder-assisted current accounted for displacement mechanism and (b) the oscillatory density of states and radiation induced oscillations in the distribution function accounted for inelastic mechanism. The figure is adapted from Ref. [64].

will not be made and the sample conductivity does not change. When $\omega/\omega_c = n + 1/2$, electrons have the same chance to be scattered along or against the electric field, reaching nth or $(n+2)$th LL. Thus overall there is no change in the sample conductivity. Upon swept magnetic fields, the absorbed photons will pass through LLs, giving rise to the oscillatory pattern. The MIRO period and phase detected in the experiments are consistent with this displacement mechanism.

Another contribution is known as the inelastic mechanism [74, 73, 75, 64]. As shown in Figure. 1.10(b), the main effect comes from the radiation-induced corrections to the Fermi distribution function stabilized by inelastic scatterings. By solving the stationary kinetic equation for the zeroth angular harmonic of the distribution function, the modulation in the DOS in the presence of microwave radiation induces a small modulation in the electron energy distribution, which results in a considerable change in conductivity.

Taking those two mechanisms into account, MIRO can be theoretically modeled as

$$\frac{\delta\rho_\omega}{\rho_0} = -2\pi\frac{\omega}{\omega_c}\mathcal{P}\lambda^2\eta\sin\frac{2\pi\omega}{\omega_c}. \tag{1.20}$$

Here, ρ_0 is the resistivity at zero magnetic field. The dimensionless scattering rate η is

given by [75]

$$\eta = \frac{\tau}{2\tau_\star} + \frac{2\tau_{\rm in}}{\tau}\,, \tag{1.21}$$

where $\tau_{\rm in}$ is the inelastic time estimated as $\tau_{\rm in} \approx 0.82\tau_{\rm ee} \propto T^{-2}$ in the condition of $\pi k_B T \gg \hbar\omega$ [73]. $\tau_{\rm ee}$ is the electron-electron scattering time which is introduced later in this section. $\tau_\star$ is the displacement time estimated as $\tau_\star^{-1} \equiv 2\left\langle \tau_\theta^{-1}(1-\cos\theta)^2\right\rangle_\theta$ where $\langle\cdots\rangle_\theta$ denotes averaging over θ. The rate of scattering on angle θ can be expressed in terms of angular harmonics, $\tau_n = \tau_{-n}$, as $\tau_\theta^{-1} = \sum\limits_{-\infty}^{+\infty} \tau_n^{-1} e^{in\theta}$. $\mathcal{P}$ is the dimensional parameter proportional to the microwave power. For linearly polarized microwaves,

$$\mathcal{P}(\epsilon) = \frac{\mathcal{P}^0}{2}\sum_{\pm}\frac{1}{(1\pm\epsilon^{-1})^2+\beta_\omega^2},\ \mathcal{P}^0 = \frac{e^2\mathcal{E}_{\rm ac}^2 v_F^2}{\epsilon_{\rm eff}\hbar^2\omega^4}, \tag{1.22}$$

where $\beta_\omega \equiv (\omega\tau_{\rm em})^{-1} + (\omega\tau)^{-1}$, $\tau_{\rm em}^{-1} = n_e e^2/2\sqrt{\epsilon_{\rm eff}}\epsilon_0 m^\star c$ is the radiation decay rate, $2\sqrt{\epsilon_{\rm eff}} = \sqrt{\varepsilon}+1$, ε is the dielectric constant. If the sample thickness is much thinner than the wavelength inside the sample $2\pi c/\omega\sqrt{\varepsilon}$, one can neglect the polarization of the medium around the 2DEG and put $\varepsilon = 1$. v_F is the Fermi velocity, and $\mathcal{E}_{\rm ac}$ is the microwave electric field. The above expression was obtained assuming $2\pi k_B T \gg \hbar\omega$ and is accurate away from the cyclotron resonance ($2\pi\epsilon \gg 1$), when the microwave power is not too high ($\mathcal{P} \ll 1$), and when LLs are overlapping ($\lambda \ll 1$).

While it was established that MIRO at a high microwave power significantly deviate from Eq. (1.20), they can still be well described within the same theoretical framework after being generalized to an arbitrary radiation intensity [76, 77, 78]. However, experiments also revealed situations where the existing theory is inadequate, e.g., in describing the measured dependencies on radiation polarization [79, 80] and on temperature [81]. Limitations of the theory were also identified in the regime of separated LLs [82] and in the radiation-induced modification of SdHO [83]. In Chapter 5.2, we report the unexpected experimental findings on the MIRO dependent on the carrier density which challenges the existing theories.

Additional, MIRO is a tool to access physical parameters in the samples. For example, with a single B-sweep, carrier effective mass can be extracted from the MIRO period. In Section 5.1, by employing MIRO, we study the effective mass dependent on the carrier density in a back-gated GaAs quantum well. Another important parameter

often extracted from MIRO is the quantum lifetime $\tau_{\rm q}$, as a measure of sample cleanliness as introduced in Section 1.2. Also, by performing the Dingle analysis, we obtain the quantum lifetime $\tau_{\rm q}$ from the decay of MIRO amplitudes. We study the effect of illumination on $\tau_{\rm q}$ in a GaAs quantum well with MIRO in Chapter 6. We note that, unlike SdHO, the quantum lifetime $\tau_{\rm q}$ obtained from MIRO is reduced by electron-electron scattering due to the T-dependent renormalization of the DOS by electron-electron interactions. The relationship is shown as [84, 85, 86, 87, 88, 75],

$$\frac{1}{\tau_{\rm q}} = \frac{1}{\tau_{\rm q,0}} + \frac{1}{\tau_{\rm ee}}. \tag{1.23}$$

The electron-electron scattering rate $1/\tau_{\rm ee}$ is given by [84, 85]

$$\frac{\hbar}{\tau_{\rm ee}} = \frac{\pi k_B^2 T^2}{4E_F} \ln \frac{2\hbar v_F/a_B}{\max\{\pi k_B T, \hbar\omega_{\rm c}(\omega_{\rm c}\tau)^{1/2}\}}. \tag{1.24}$$

where a_B is the Bohr radius.

Chapter 2

Two- and three-electron bubbles in $Al_xGa_{1-x}As/Al_{0.24}Ga_{0.76}As$ quantum wells

This chapter is adapted from X. Fu, Q. Shi, M. A. Zudov, G. C. Gardner, J. D. Watson, and M. J. Manfra, Two- and three-electron bubbles in $Al_xGa_{1-x}As/Al_{0.24}Ga_{0.76}As$ quantum wells, *Phys. Rev. B* **99**, 161402(R) (2019), by permission of the American Physical Society under the American Physical Society reuse and permission license.

2.1 Introduction: quantum Hall bubbles

While the effect of disorder on transport characteristics of a two-dimensional electron gas (2DEG) is usually deemed detrimental, there exist many situations in which the disorder is beneficial. The most celebrated examples are integer [1] and fractional [2] quantum Hall effects (QHEs) which rely on single-(quasi)particle localization by the disorder potential. Many nonequilibrium transport phenomena in very high Landau levels, such as microwave-[7] and Hall field-induced resistance oscillations [89], along with several other related phenomena [76, 78], also benefit from a modest amount of impurities which can provide large-angle scattering.

Furthermore, disorder provides a pinning potential for Wigner crystals [90, 91, 92,

93, 94, 95, 96, 97] and "bubble" phases [3, 4, 98, 5, 6, 57, 99, 100] allowing for their transport manifestation. These bubble phases can be viewed as generalizations of a Wigner crystal formed from clusters of $M \geq 1$ particles per unit cell. Such clustering of electrons (or holes) into "bubbles" is made possible in partially-filled high Landau levels because ring-like electron wavefunctions interact with a box-like potential which is a result of an interplay between long-range direct and short-range exchange components of Coulomb interaction [3]. At low temperatures these M-particle bubbles crystallize into a triangular lattice with a lattice constant $\Lambda_b \approx 3.3R_c$ [4], where $R_c = l_B\sqrt{2N+1}$ is the cyclotron radius, N is the Landau level index, $l_B = (\hbar/eB)^{1/2}$ is the magnetic length, and B is the perpendicular magnetic field. Being pinned by disorder, such bubble crystals are insulating and the measured resistances are akin to those at the nearest integer filling factors $[\nu]$, i.e., both R_{xx} and R_{xy} are small, while R_{xy} exhibits integer QHE. This picture is also supported by the observation of pinning mode resonances in microwave spectroscopy studies [59, 60].

To date, experiments on the bubble phases have focused primarily on $N = 1$ [99, 101, 102, 103, 104, 105, 106, 107] and $N = 2$ [5, 6, 57, 50, 61, 58, 108, 107, 100] Landau levels. At $N = 1$, experiments revealed signatures of eight bubble phases occurring at $\nu^\star \approx 0.29$ and $\nu^\star \approx 0.43$ (see, e.g., Ref. [103]) in each spin sublevel (as well as their electron-hole symmetric values, $\nu^\star \approx 1 - 0.29$ and $\nu^\star \approx 1 - 0.43$), where $\nu^\star = \nu - \lfloor\nu\rfloor$ is the partial filling of the Landau level and $\lfloor\nu\rfloor = \max\{m \in \mathbb{Z} \,|\, m \leq \nu\}$ is the integral part of ν. These states can be ascribed to one- and two-particle bubbles, respectively [109, 110]. At $N = 2$, transport studies (see, e.g., Ref. [61]) found four insulating states accompanied by integer QHE near $\nu^\star \approx 0.28$ and $\nu^\star \approx 1 - 0.28$, which likely reflect formation of bubble crystals with $M = 2$. Moreover, recent experiments in graphene revealed four bubble phases at $N = 2$ and $\nu^\star \approx 0.33$ [100]. While at $N = 2$ theory (see, e.g., Refs. [56], [110]) also predicts bubble phases with $M = 1$, to our knowledge, their existence has not been confirmed in transport measurements. On the other hand, microwave spectroscopy measurements [60] have detected pinning mode resonances which were ascribed to bubble phases with $M = 1$ and $M = 2$. Similar to $N = 2$, theory [110, 111] predicts at least two kinds of bubbles at $N = 3$, with $M = 2$ and $M = 3$, but experiments have so far detected only four isotropic insulating states centered around $\nu^\star \approx 0.27$ (see, e.g., Ref. [47]).

In this chapter we report on transport signatures of *eight* distinct bubble phases in the $N = 3$ Landau level of a $Al_xGa_{1-x}As/Al_{0.24}Ga_{0.76}As$ quantum well with $x = 0.0015$. These signatures are observed in both lower and upper spin branches near partial filling factors $\nu^\star \approx 0.2$ and $\nu^\star \approx 0.3$ (and their particle-hole conjugates $\nu^\star \approx 0.8$ and $\nu^\star \approx 0.7$), which correspond to $M = 2$ and $M = 3$ electrons (or holes) per bubble, respectively. The temperature dependence suggests that three-particle bubbles start to develop at somewhat higher temperature than two-particle bubbles. The data in the control sample (with $x = 0$) on the other hand, show only four insulating states which, however, extend over wider ranges of $\nu^\star$, i.e. $0.20 \lesssim \nu^\star \lesssim 0.33$. We believe that a small amount of alloy disorder helps to distinguish between two- and three-particle bubbles in our $Al_xGa_{1-x}As/Al_{0.24}Ga_{0.76}As$ quantum well.

2.2 Experimental evidence of two- and three-electron bubbles

While we have observed signatures of two- and three-particle bubbles in several 30 nm-wide $Al_xGa_{1-x}As/Al_{0.24}Ga_{0.76}As$ quantum wells (with identical heterostructure design but with different Al content x from 0.0 to 0.0036 [112]), here we present the data obtained from a sample with $x = 0.0015$. After a brief low-temperature illumination, our sample had the density $n_e \approx 2.9 \times 10^{11}$ cm^{-2} and the mobility $\mu \approx 3.6 \times 10^6$ cm^{2}V^{-1}s^{-1}. The sample was a 4×4 mm square with eight indium contacts positioned at the corners and the midsides. Resistances, R_{xx}, R_{yy}, and R_{xy} were measured using a four-terminal, low-frequency lock-in technique.

In Figure. 2.1 we present the longitudinal resistances R_{xx} (solid line, left axis), R_{yy} (dotted line, left axis), and the Hall resistance R_{xy} (right axis) as a function of the filling factor ν measured at $T \approx 25$ mK. The shaded areas mark the regions $0.38 \leq \nu^\star \leq 0.62$ where $R_{xx} > R_{yy}$ reflecting the formation of anisotropic stripe phases [3, 5, 6] with the easy direction along the $\langle 110 \rangle$ crystal axis. In the $N = 2$ Landau level the data clearly show four isotropic insulating states occurring near partial fillings $\nu^\star \approx 0.28$ and $\nu^\star \approx 0.72$ (marked by vertical dashed lines) of both the lower and the upper spin branch. These states are attributed to the formation of bubble crystals formed by clusters of $M = 2$ electrons or holes. As expected, $R_{xx} \approx R_{yy} \approx 0$, while R_{xy} exhibits re-entrant

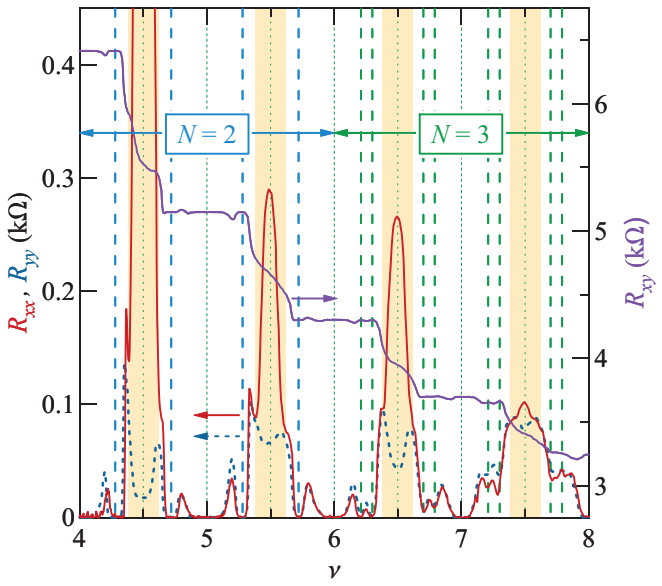

Figure 2.1: (Color online) Longitudinal resistance R_{xx} (solid line, left axis), R_{yy} (dotted line, left axis), and Hall resistance R_{xy} (right axis) as a function of the filling factor ν at $T \approx 25$ mK. Bubble phases in the $N = 2$ and $N = 3$ Landau levels are marked by vertical dashed lines drawn at $\nu^\star = 0.28, 0.72$ and at $\nu^\star = 0.21, 0.30, 0.70, 0.79$, respectively. Shaded regions correspond to $0.38 \leq \nu^\star \leq 0.62$, where stripe phases form (see, e.g., Ref. [56]).

QHE at $R_{xy} = R_{\rm K}/[\nu]$, where $R_{\rm K} = h/e^2 \approx 25.812$ kΩ is the von Klitzing constant.

Remarkably, R_{xx} and R_{yy} in the $N = 3$ Landau level reveal *eight* well-defined minima, two on each side of both half-filled spin sublevels. The positions of these minima are marked by vertical dashed lines drawn at $\nu^\star = 0.21, 0.30, 0.70, 0.79$. Since two of these partial fillings are fairly close to $\nu^\star = 1/5$ and $\nu^\star = 4/5$ where calculations [113, 110] show that QHE at $\nu^\star = 1/5$ can occur only at $N \leq 2$, might support QHE, it is important to examine the R_{xy} data more closely. In Figure. 2.2 we present a zoom-in view of the data for $6.0 < \nu < 6.5$. One observes that as both R_{xx} and R_{yy} approach zero at $\nu^\star \approx 0.21$ and $\nu^\star \approx 0.30$, the Hall resistance R_{xy} exhibits re-entrant integer QHE with $R_{xy} = R_{\rm K}/6$ and not fractional QHE. These observations strongly suggest the formation of bubble phases at these filling factors, which we label *R6a* and *R6b*.

Although the remaining six minima do not reach zero in our experiment, they (i)

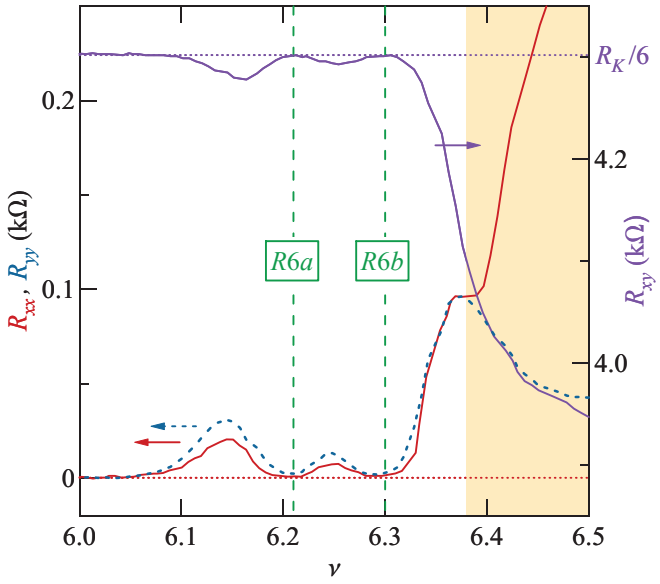

Figure 2.2: (Color online) Zoom-in view of Figure. 2.1 for ν between 6.0 and 6.5. Re-entrant integer quantum Hall states are marked by $R6a$ and $R6b$.

occur either near the same partial fillings $\nu^\star$ or their electron-hole symmetric counterparts $\nu^\star = 0.79$ and $\nu^\star = 0.70$, and (ii) are accompanied by re-entrant QHE features in the R_{xy}. We thus believe that these features also signal formation of the bubble phases and we will refer to them as $R6c, R6d, R7a, R7b, R7c$, and $R7d$. As illustrated in Figure. 2.1, partial fillings of bubble phases show little difference between the lower and the upper spin branches (i.e., $\nu^\star_{R6\alpha} \approx \nu^\star_{R7\alpha}$ for $\alpha = a, b, c, d$), and, as already mentioned, are electron-hole symmetric (i.e., $\nu^\star_{Rid} \approx 1 - \nu^\star_{Ria}$ and $\nu^\star_{Ric} \approx 1 - \nu^\star_{Rib}$ for $i = 6, 7$).

We can estimate the number M of electrons per bubble from $\nu^\star < 1/2$, Landau level index N, and the lattice constant of the bubble phase Λ_b using

$$M = \frac{\sqrt{3}}{2\pi}\left(\frac{\Lambda_b}{R_c}\right)^2 (N + 1/2)\nu^\star \,. \tag{2.1}$$

This result coincides with Eq. (55) of Ref. [4] (apart from "+1/2") and can be easily obtained from geometrical considerations. With $S_0 = \sqrt{3}\Lambda_b^2/2$ being the area of the triangular lattice unit cell and $n_e^\star = \nu^\star(2\pi l_B)^{-2}$ being the electron density in the N-th Landau level, one finds $M = S_0 n_e^\star$, which, with $R_c = l_B\sqrt{2N+1}$, gives Eq. (2.1). With $\Lambda_b \approx 3.3R_c$ [4, 113], $N = 3$, and $\nu^\star = 0.21, 0.30$, we find $M \approx 2$ for Ria and $M \approx 3$ for

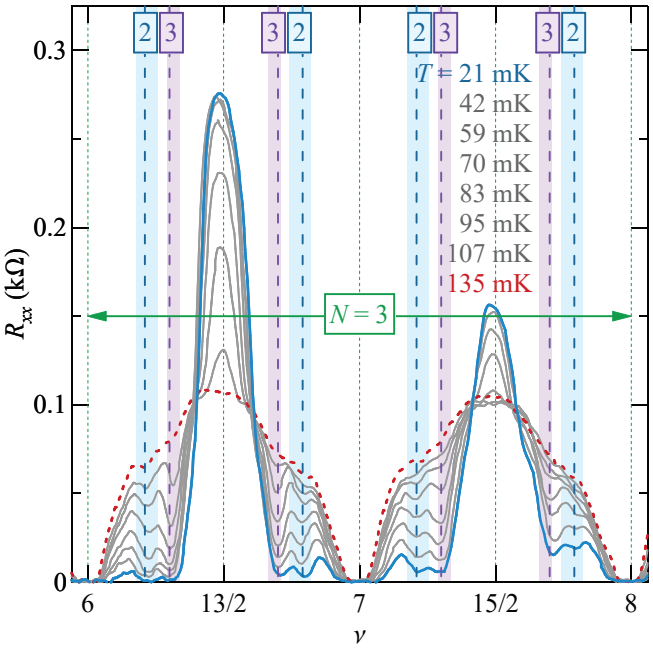

Figure 2.3: (Color online) Longitudinal resistance R_{xx} vs filling factor ν in the $N = 3$ Landau level at different temperatures from 21 mK (thick solid line) to 135 mK (dotted line), as marked. Shaded areas correspond to the ranges of $\nu^\star$ where calculations [111] predict bubble phases with $M = 2$ and $M = 3$, as marked.

Rib. With $\nu^\star = 0.28$ and $N = 2$, Eq. (2.1) yields $M \approx 2.1$, consistent with 2-electron bubble phase. These values are in excellent agreement with the theory [113, 111, 110] predicting formation of bubble phases with $M = 2$ and $M = 3$ electrons per bubble in the $N = 3$ Landau level. We thus conclude that *Ria*, *Rid* and *Rib*, *Ric* are two- and three-particle bubble phases, respectively.

2.3 Temperature dependence

To further test the idea that our data manifest the formation of the bubble phases, we have examined the temperature dependence. In Figure. 2.3(a) we present longitudinal resistance R_{xx} as a function of the filling factor ν measured at different temperatures T from 21 mK (thick solid line) to 135 mK (dotted line), as marked. At the highest $T \approx 135$ mK, the R_{xx} is rather featureless, apart from QHEs near integer ν. In the vicinity of $\nu^\star = 1/2$, the R_{xx} rapidly rises with decreasing T reflecting formation of

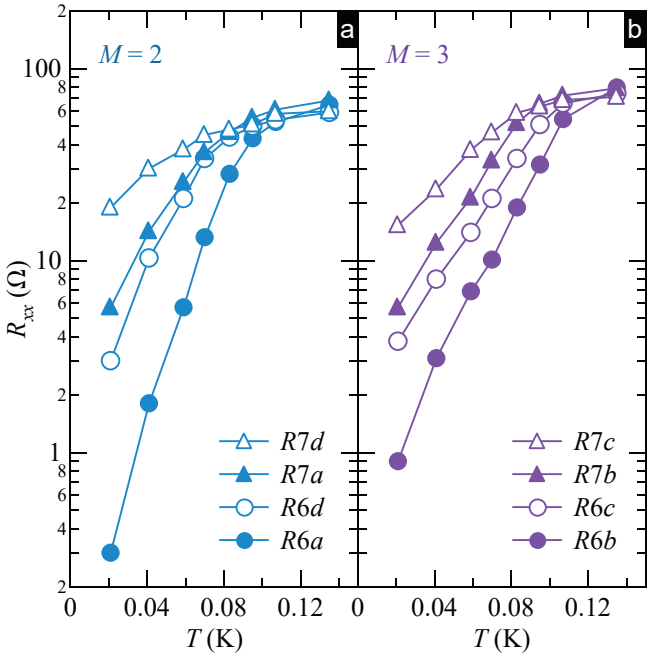

Figure 2.4: (Color online) Resistance R_{xx} at $\nu^\star$ corresponding to bubble phases in the $N = 3$ Landau level with (a) $M = 2$ and (b) $M = 3$ particles per bubble, see legend, as a function of temperature T. Log-linear scale is used for clarity.

stripe phases. Away from half-filling, however, the R_{xx} drops as the temperature is lowered and double minima develop on each side of the half-filling. These minima remain roughly at the same filling factors (marked by vertical dashed lines) over the entire temperature range. Moreover, these filling factors fall within the ranges of $\nu^\star$ (shaded areas) where density matrix renormalization group calculations [111] predict bubble phases with $M = 2$ and $M = 3$.

Further examination of the data in Figure. 2.3 shows that the minima near $\nu^\star \approx 0.3(0.7)$ develop faster with decreasing T than the ones near $\nu^\star \approx 0.2(0.8)$, a behavior most evident at intermediate temperatures, although eventually both approach roughly the same resistance values at the lowest T. Understanding this subtle difference in the temperature dependencies of the two phases will require further investigations.

In Figure. 2.4 we plot longitudinal resistance R_{xx} at filling factors ν corresponding to bubble phases with (a) $M = 2$ and (b) $M = 3$ (as noted in the legend) versus

temperature T using the log-linear scale (for clarity). Both data sets manifest very similar behavior, apart from the above-mentioned better development of the three-particle bubbles at intermediate T. Each of the data sets shows that the low-temperature resistance at the bubble minima grows with the total filling factor ν, suggesting weakening of these phases with increasing ν. This observation is qualitatively consistent with the monotonic decrease of the onset temperature of the bubble phases in the $N = 2$ Landau level [61]. As demonstrated in Ref. [103], the dependence of the onset temperature on the filling factor in the $N = 1$ Landau level is strongly non-monotonic. Non-monotonic dependence of the onset temperature of bubbles has also been found in the $N = 2$ Landau level of graphene [100].

2.4 Role of alloy disorder

It is interesting to note that the resistance minima which we associate with two- and three-particle bubble phases are separated by a resistance maximum, suggesting particle delocalization at these $\nu^\star$. This finding seems to agree with calculations [111] which did not find bubble phases for $0.25 < \nu^\star < 0.30$ at $N = 3$. However, our measurements in the control sample (with $x = 0$) show only four insulating states (see, also Ref. [47]) which extend over much wider ranges of $\nu^\star$, i.e., $0.20 \lesssim \nu^\star \lesssim 0.33$, at low temperatures. As the temperature is raised, this range of $\nu^\star$ shrinks asymmetrically towards $\nu^\star \approx 0.3$, a point where we observe $M = 3$ bubble phase in samples with non-zero x. Our observation of finite conductivity near $\nu^\star \approx 0.25$ suggests that alloy disorder narrows the ranges of filling factors where bubble phases with $M = 2$ and $M = 3$ are insulating, allowing one to resolve them separately. If at $\nu^\star \approx 0.25$ the bubble phases with $M = 2$ and $M = 3$ are energetically degenerate, one can expect coexistence of both types of bubbles. As one crosses this filling factor, electrons (or holes) must hop between different types of bubbles as the new bubble lattice is being formed. Being short-range, alloy disorder can facilitate such hopping via large-angle scattering events (accompanied by large momentum transfer) leading to finite conductivity near the transition.

Chapter 3

Hidden quantum Hall stripes in $Al_xGa_{1-x}As/Al_{0.24}Ga_{0.76}As$ quantum wells

This chapter is adapted from X. Fu, Y. Huang, Q. Shi, B. I. Shklovskii, M. A. Zudov, G. C. Gardner, and M. J. Manfra, Hidden quantum Hall stripes in $Al_xGa_{1-x}As/Al_{0.24}Ga_{0.76}As$ quantum wells, *Phys. Rev. Lett.* **125**, 236803 (2020), by permission of the American Physical Society under the American Physical Society reuse and permission license.

3.1 Introduction: symmetry breaking fields in quantum Hall stripes

Forming due to a peculiar boxlike screened Coulomb potential, QHSs can be viewed as charge density waves consisting of stripes with alternating integer filling factors ν, e.g., $\nu = 4$ and $\nu = 5$. Considering thermal and quantum fluctuations, several electron liquid crystal-like phases have also been proposed [51]. In experiments, QHSs are manifested by giant resistivity anisotropies ($\rho_{xx} \gg \rho_{yy}$) in $N \geq 2$ half-filled Landau levels. Appearance of these anisotropies in macroscopic samples is attributed to a mysterious symmetry-breaking field [114, 39, 40, 37], which nearly always aligns QHSs along the

$\hat{y} \equiv \langle 110 \rangle$ crystal axis of GaAs. In few cases, QHSs were found to align along the $\langle 1\bar{1}0 \rangle$ direction in a tunable density heterostructure insulated gate field effect transistor at densities n_e between 3×10^{11} cm^{-2} and 4.6×10^{11} cm^{-2} [36] and in single heterointerface devices with $n_e \simeq 2 \times 10^{11}$ cm^{-2} and cap thickness exceeding 1 μm [37]. While a sufficiently low disorder is necessary for the QHS formation, the absence of QHSs in systems beyond GaAs might simply be due to the lack of symmetry-breaking fields. Indeed, anisotropies emerging under the in-plane magnetic field, which is known to provide symmetry breaking [42, 41, 43, 44, 45, 115, 46], have been observed in ZnO [116] and AlAs [117]. Electron bubble phases [3, 4, 98, 57, 99, 59, 103, 105, 35, 107, 108, 118, 119], on the other hand, without any native symmetry breaking fields, which are close relatives of QHSs, have already been identified in graphene [100].

In this chapter, we report observation of transport signatures of the recently predicted [120] hidden QHS (hQHS) phases in a series of $Al_xGa_{1-x}As/Al_{0.24}Ga_{0.76}As$ quantum wells with $x < 10^{-3}$. In contrast to the ordinary QHS phases, the hQHS phases are characterized by isotropic resistivity ($\rho_{xx} = \rho_{yy} = \rho$) that is independent of ν, unlike the isotropic liquid phases in which $\rho \propto \nu^{-1}$. These unique properties make these phases detectable without symmetry-breaking fields, thereby opening an avenue to study stripe physics in systems beyond GaAs. The wide variation of mobilities in our samples allows us to construct an experimental phase diagram in the conductivity-filling factor plane. Its comparison to theoretical predictions [120] yields the electron quantum lifetimes and the stripe density of states. The latter turns out to be lower than predicted by original the Hartree-Fock theory [3, 4], calling for further theoretical input. We confirm this finding by a complementary experiment on an ultrahigh mobility GaAs quantum well, where we also show that, in this sample, the hQHS phase yields to the QHS phase in agreement with the theory.

3.2 Theoretical mechanisms behind hidden quantum Hall stripe phases

Before presenting our experimental data, we briefly summarize the physics behind the hQHS phases [120]. The resistance anisotropies in the ordinary QHS phase emerge due to different diffusion mechanisms along and perpendicular to the stripes [52, 121, 54].

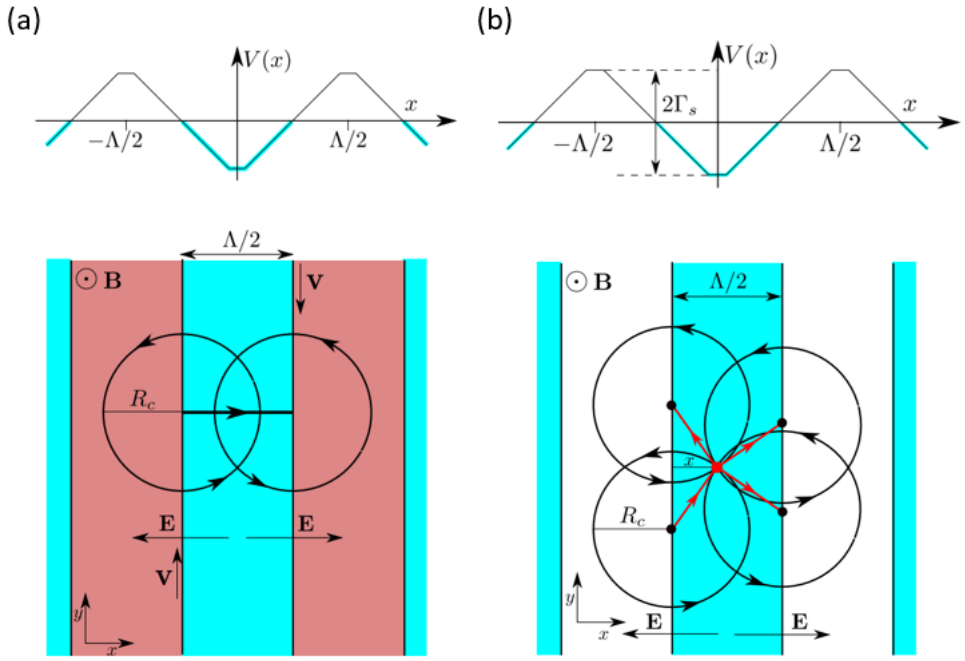

Figure 3.1: Schematic of transport in the quantum Hall stripe and hidden quantum Hall stripe phase. (a) Electrons on the stripe edges (shown in blue) drift in electric fields E with velocity v in the y direction. They are scattered to an adjacent stripe edge by background charged impurities, as illustrated by the thick horizontal arrow. (b) Impurity scattering dominated hopping transport. An electron with the guiding center (black dot) at the lower left edge of the central electron stripe is scattered off an impurity (red dot) at the distance x from its edge. Three possible hops of the guiding center are shown by red arrows. The figure is adopted from Refs. [54] and [120].

In this picture, an electron drifts a distance L_y along the y-oriented stripe edge in an x-directed internal electric field until it is scattered by impurities to one of the adjacent stripe edges located at a distance $L_x = \Lambda/2 \approx \sqrt{2}R_c$ [3, 4], where Λ is the stripe period and R_c is the cyclotron radius, as illustrated in Figure. 3.1(a). When $L_y \gg L_x$, the diffusion coefficient in the $\hat{y}$ direction is much larger that in the $\hat{x}$ direction, which leads to anisotropic conductivity, $\sigma_{yy} \gg \sigma_{xx}$, and resistivity, $\rho_{xx} \gg \rho_{yy}$. Since $L_y \propto \nu^{-1}$ and $L_x \propto \nu$ [54], the anisotropy decreases with ν and eventually vanishes at some $\nu = \nu_1$. At larger ν, the drift contribution to the diffusion along stripes can be neglected, and L_y,

like L_x, is determined entirely by the impurity scattering, as illustrated in Figure. 3.1(b). For isotropic scattering, it is easy to show that $L_y = \sqrt{2}R_{\rm c}$ which coincides with L_x, as the mean free path along stripes limited by isotropic impurity scattering can be calculated using $L_y^2 = (1/2\pi)\int_0^{2\pi} d\theta (2R_c\cos\theta)^2 = 2R_c^2$. As a result, the QHS phase yields to the hQHS phase in which the resistivity is isotropic and ν independent (since the stripe density of states does not vary with ν). The hQHS phase persists until the stripe structure is destroyed by disorder at $\nu = \nu_2$ and the ground state becomes an isotropic liquid with $\rho_{xx} = \rho_{yy} \propto \nu^{-1}$, as predicted by Ando and Uemura [122] and experimentally confirmed by Coleridge, Zawadski, and Sachrajda (CZS) [123].

For the hQHS phase to exist and be detected, it should span a sizable range of the filling factors $\Delta\nu = \nu_2 - \max\{\nu_1, 9/2\} \gg 1$. The range $\Delta\nu$ depends sensitively on both transport τ^{-1} and quantum $\tau_{\rm q}^{-1}$ scattering rates, which control ν_1 and ν_2, respectively [120]. As we will see, ultrahigh mobility GaAs quantum wells do not support the hQHS phase as $\nu_1 \approx \nu_2$ in these samples. On the other hand, adding the correct small amount of Al to the GaAs well greatly expands $\Delta\nu$, as it affects ν_1 to a much greater extent than it does ν_2. Our estimates show that $\Delta\nu$ reaches a maximum of 6 at $x \approx 0.1\,\%$. This happens because Al acts as a short-range disorder, which contributes *equally* to transport τ^{-1} and quantum $\tau_{\rm q}^{-1}$ scattering rates, and because $\tau_{\rm q}/\tau \ll 1$ at $x = 0$.

3.3 Transport signatures of hidden quantum Hall stripe phases

Apart from different x, all our $Al_xGa_{1-x}As$ quantum wells share an identical heterostructure design [112]. Electrons are supplied by Si doping in narrow GaAs wells surrounded by narrow AlAs layers and placed at a setback distance of 75 nm from each side of

Table 3.1: Sample ID, Al mole fraction x, electron density n_e, mobility μ, and Drude conductivity, in units of e^2/h, $\tilde{\sigma}_0 = hn_e\mu/e$ at zero magnetic field ($B = 0$).

Sample ID	x	n_e (10^{11} cm^{-2})	μ (10^6 cm^2/Vs)	$\tilde{\sigma}_0$ (10^3)
A	0.00057	3.0	6.5	8.0
B	0.00082	2.9	4.1	4.9
C	0.0078	2.7	1.2	1.3

the 30-nm-wide $Al_xGa_{1-x}As$ well hosting the 2D electrons. Parameters of samples A, B, and C such as Al mole fraction x, electron density n_e, mobility μ, and Drude conductivity $\tilde{\sigma}_0 = hn_e\mu/e$ in units of e^2/h at zero magnetic field ($B = 0$) are listed in Table 3.1. The samples are approximately 4 mm squares with eight indium contacts positioned at the corners and at the midsides. Longitudinal resistances R_{xx} and R_{yy} were measured in sweeping magnetic fields using a four-terminal, low-frequency (a few Hz) lock-in technique at a temperature $T \approx 25$ mK at which the resistances are nearly temperature independent. The current was sent along either the $\hat{x} \equiv \langle 1\bar{1}0\rangle$ or $\hat{y} \equiv \langle 110\rangle$ direction using the midside contacts, and the voltage was measured between contacts along the edge. To account for anisotropies due to non-ideal geometry, R_{xx} or R_{yy} was multiplied by a factor (typically $\lesssim 1.1$) that was chosen to make $R_{xx} = R_{yy}$ in the low field regime.

In Figure. 3.2, we present longitudinal resistances R_{xx} and R_{yy} as a function of filling factor ν measured in sample B. At low half-integer filling factors ($\nu = 9/2$, $11/2$, and $13/2$) the data reveal conventional QHS phases, as evidenced by $R_{xx} > R_{yy}$. At high half-integer filling factors ($\nu > 25/2$) we identify the CZS phase in which $R_{xx} \approx R_{yy} \propto \nu^{-1}$ (cf. dash-dotted line). At intermediate half-integer filling factors, $\nu = 15/2, ..., 23/2$, one readily confirms *both* characteristic features of the hQHS phase; indeed, the data show that two longitudinal resistances are practically the same ($R_{xx} \approx R_{yy}$) and are *independent* of ν (cf. dashed line). From Figure. 3.2, we can easily identify the characteristic filling factors $\nu_1 \approx 7$ and $\nu_2 \approx 12.5$ which mark the crossovers from the QHS to the hQHS phase and from the hQHS to the CZS phase, respectively.

In a similar manner, we have obtained ν_1 and ν_2 for sample A and ν_2 for sample C (which does not support the QHS phase due to higher Al mole fraction x), which we then use to construct the experimental phase diagram shown in Figure. 3.3. We start by adding points representing the dimensionless Drude conductivity $\tilde{\sigma}_0$ for samples A, B, C (see Table 3.1) and the corresponding filling factors ν_1 (solid circles) and ν_2 (solid squares). To connect these data points we use the theoretical boundaries of the hQHS phase [120]. The lower boundary $\nu = \nu_1$, separating the QHS and the hQHS phases, is given by [120]

$$\nu_1 \simeq \frac{\sqrt{\tilde{\sigma}_0}}{\alpha}\,, \tag{3.1}$$

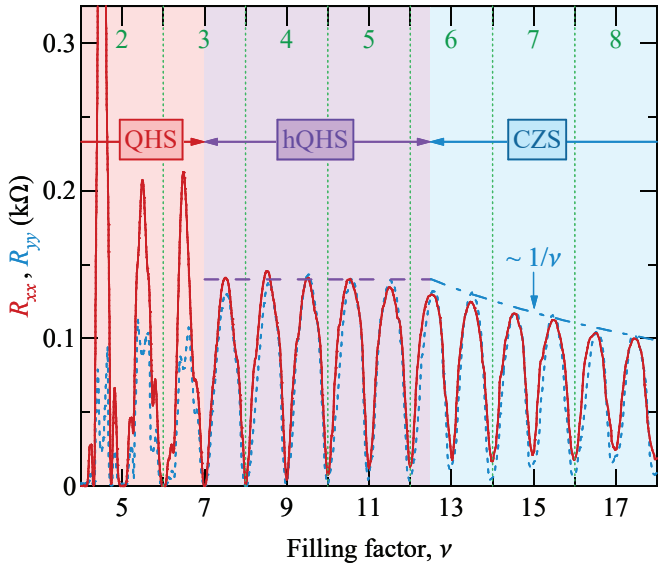

Figure 3.2: Longitudinal resistances R_{xx} (solid line) and R_{yy} (dotted line) as a function of the filling factor ν measured in sample B. Gap centers between spin-resolved Landau levels are labeled by $N = 2, 3, ...$, at the top axis ($\nu = 2N + 1$). The conventional QHS phase ($R_{xx} > R_{yy}$) and the CZS phase ($R_{xx} \approx R_{yy} \propto \nu^{-1}$) occur at half-integer $\nu = 9/2, 11/2, 13/2$ and at $\nu = 27/2, 29/2, ...$, respectively. The hQHS phase is identified at intermediate half-integer filling factors, $\nu = 15/2, ..., 25/2$, where the resistance is isotropic *and* ν independent. The characteristic ν^0 (ν^{-1}) dependence of the isotropic resistance in the hQHS (CZS) phase is marked by dashed (dash-dotted) line.

where α [1] is the QHS density of states in units of the density of states per spin at $B = 0$, $g_0 = m^\star/2\pi\hbar^2$. This boundary can be obtained by either matching the parameter-free geometric average of the resistivities in the QHS phase $\sqrt{\rho_{xx}\rho_{yy}} = (h/e^2)/(2\nu^2 + 1/2) \approx (h/e^2)/2\nu^2$ [52, 54] and the resistivity in the hQHS phase [120],

$$\tilde{\rho}_{\rm hQHS} \equiv \frac{h}{e^2}\frac{\alpha^2}{2\tilde{\sigma}_0}\,, \tag{3.2}$$

or, equivalently, by setting the resistivity anisotropy ratio to unity, $\rho_{xx}/\rho_{yy} \approx (\tilde{\sigma}_0/\alpha^2\nu^2)^2 = 1$ [54, 120].

[1] In general, α should be modified by a factor $\sqrt{2\gamma}$, where γ is a parameter depending on the nature of scattering [54]. In samples without alloy disorder, γ decreases with N_1/N_2 where N_1 (N_2) is the concentration of Coulomb impurities in the barrier (quantum well), starting from $\gamma \approx 0.43$ at $N_1 = N_2$ [54], whereas in samples where scattering is dominated by alloy disorder $\gamma \approx 0.53$ [120]. While we estimate $\gamma \approx 0.4$ in our samples A and B, we will assume $\gamma = 0.5$ for simplicity.

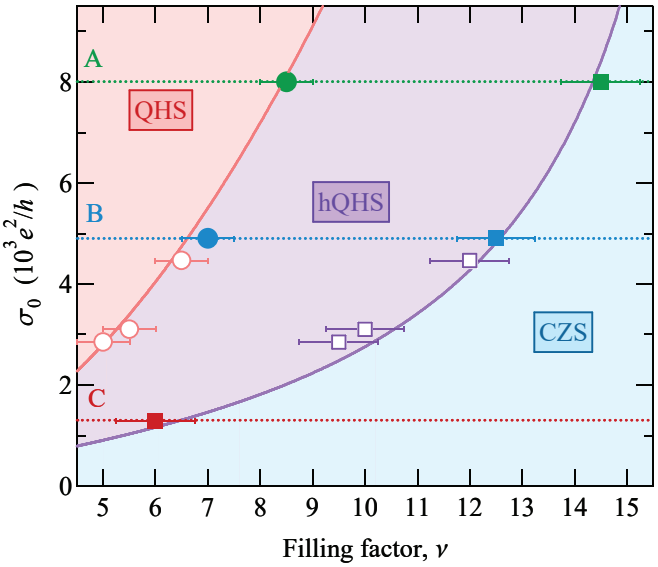

Figure 3.3: A diagram in the (ν, σ_0) plane showing QHS, hQHS, and CZS phases. Solid lines represent crossovers between phases, Eq. (3.1) [left(upper) line] and Eq. (3.3) [right(lower) line]. Solid circles (solid squares) represent experimental ν_1 (ν_2) and horizontal dotted lines mark $\tilde{\sigma}_0$ for samples A-C [112]. Open circles (squares) are additional data from a study conducted in a different context that conform to our present findings [124].

The higher boundary $\nu = \nu_2$ marks the crossover from the hQHS to the CZS phase and is represented by

$$\nu_2 \simeq \frac{\tilde{\sigma}_0}{\alpha^2}\frac{\tau_q}{\tau}\,. \tag{3.3}$$

This boundary can be obtained by equating α and the density of states at the center of the Landau level in CZS phase, in units of the density of states at $B = 0$, $\sqrt{\omega_c \tau_q}$ [125, 126] or by matching $\rho_{\rm hQHS}$ and the resistivity in the CZS phase [123],

$$\rho_{\rm CZS} \equiv \frac{h}{e^2}\frac{1}{\nu}\frac{\tau_q/2\tau}{(\tau_q/2\tau)^2+1} \approx \frac{h}{e^2}\frac{1}{\nu}\frac{\tau_q}{2\tau}\,. \tag{3.4}$$

We thus see that for a given carrier density, as mentioned above, ν_2 and ν_1 are controlled by τ and τ_q, respectively. Strictly speaking, Eqs. (3.1), (3.3) are not sharp boundaries but rather gradual crossovers between corresponding phases.

With the help of Eq. (3.1) and experimental values of ν_1 in samples A and B, we estimate $\alpha \approx 11$, which is smaller than the theoretical estimate of $\alpha \simeq 18$ [54]. We then

parameterize scattering rates τ^{-1} and $\tau_{\rm q}^{-1}$ as

$$\tau^{-1} = \tau_0^{-1} + \kappa x\,, \quad \tau_{\rm q}^{-1} = \tau_{\rm q0}^{-1} + \kappa x\,, \tag{3.5}$$

where x is the Al mole fraction, $\kappa \approx 24$ ns^{-1} per % Al [112], and $\tau_0^{-1} \approx 3$ ns^{-1} [112] is the transport scattering rate in the limit of $x \to 0$. To find the remaining parameter $\tau_{\rm q0}^{-1}$, which is the quantum scattering rate in the limit of $x \to 0$, we use experimental ν_2 values and notice that Eqs. (3.1), (3.3) yield $\tau_{\rm q}/\tau \simeq \nu_2/\nu_1^2$. Using Eq. (3.5) we then obtain an estimate for $\tau_{\rm q0} \simeq 0.05$ ns which is in good agreement with $\tau_{\rm q}$ values found from low B experiments [81, 78, 127] on microwave-induced [7, 8, 64] and Hall-field-induced [89, 128, 129] resistance oscillations in GaAs quantum wells.

We next use $n_e = 3 \times 10^{11}$ cm^{-2} and $m^\star = 0.06\, m_0$ [130, 131, 132, 133, 134] to compute the phase boundaries, Eqs. (3.1), (3.3), which are shown in Figure. 3.3 by solid lines. Both lines pass in close proximity to the experimentally obtained ν_1 (solid circles) and ν_2 (solid squares) from all samples, showing excellent agreement between theory [120] and experiment. Finally, we add data points (open circles and squares) from three other $Al_xGa_{1-x}As/Al_{0.24}Ga_{0.76}As$ quantum wells that were investigated in a different context [124]. These points are also in agreement with the theory and the present experiment.

3.4 Examination of hidden quantum Hall stripes in a ultraclean GaAs quantum well

Having confirmed the existence of the hQHS phases in $Al_xGa_{1-x}As/Al_{0.24}Ga_{0.76}As$ quantum wells, we next examine the possibility for these phases to exist in ultrahigh mobility GaAs quantum wells (without alloy disorder). In such samples, the lower boundary ν_1, Eq. (3.1), might approach and even merge with the higher boundary ν_2, Eq. (3.3), eliminating the hQHS phase as a result. To test this scenario, we revisit the data obtained from sample A of Ref. [54] with $\tilde{\sigma}_0 \approx 3.4 \times 10^4$, much higher than in samples used in the present study. As illustrated in Figure. 3.4, showing ρ_{xx} (solid triangles) and ρ_{yy} (open triangles) as a function of the filling factor ν, the QHS anisotropy in this sample collapses at $\nu_1 \approx 20$. Using Eq. (3.1), we can then estimate $\alpha = \sqrt{\tilde{\sigma}_0}/\nu_1 \approx 9$. We note that, the analysis of the anisotropy ratio in this sample [54] with theoretical value

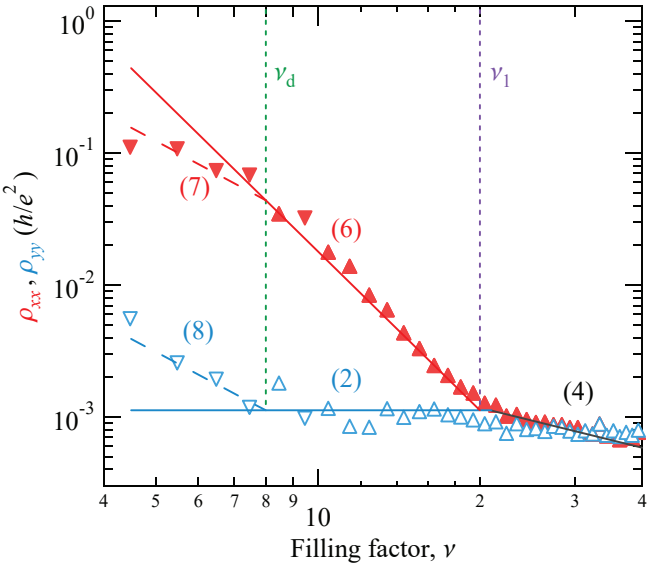

Figure 3.4: ρ_{xx} (solid triangles) and ρ_{yy} (open triangles) as a function of filling factor ν for sample A of Ref. [54]. Lines are computed using theoretical expressions, marked by equation numbers. The equations (i) marked in the figure refers to equation (3.i) in this chapter.

of $\alpha = 18$ leads to $\gamma \approx 0.15$ and a ratio of concentrations of Coulomb impurities in the spacer N_1 to that in the quantum well N_2, $N_1/N_2 \simeq 60$, much larger than $N_1/N_2 \simeq 10$ estimated in Ref. [135]. Our present experiments, however, suggest lower value of α, leading to larger γ and restoring the agreement with Ref. [135]. Larger γ can also result from interface roughness scattering, which was not theoretically considered in Ref. [135]. With $\tau_q \simeq 0.05$ ns, Eq. (3.3) gives $\nu_2 \approx 21$, which is very close to $\nu_1 \approx 20$. Indeed, the data in Figure. 3.4 show that the QHS phase crosses over directly to the CZS phase, bypassing the intermediate hQHS phase.

In the QHS phase, the easy resistivity is ν independent and is described by $\rho_{yy} = \rho_{\rm hQHS}$, Eq. (3.2), while the hard resistivity exhibits clear ν^{-4} dependence and follows [120]

$$\rho_{xx} \simeq \frac{h}{e^2} \frac{\tilde{\sigma}_0}{2\alpha^2\nu^4} \,. \tag{3.6}$$

However, the agreement between theory and experiment breaks down at $\nu < \nu_d \approx 8$, where one observes significant deviations leading to the reduction of the anisotropy. While the nature of such reduction is unclear, it becomes more pronounced upon further

cooling and might reflect a crossover to another competing ground state [53, 136]. We can account for the observed anisotropy reduction at lower filling factors assuming that the QHS phase has a finite concentration of dislocations separated by an average distance $L_{\rm d} = \beta\Lambda/2$ along stripes, where β is a numerical factor. Scattering of drifting electrons by these dislocations limits their drift length by $L_{\rm d} \ll L_y$ and the resistivities calculated in Refs. [54], [120] need to be modified to

$$\rho_{xx} = \frac{h}{e^2}\frac{\beta}{2\nu^2}\,, \tag{3.7}$$

$$\rho_{yy} = \frac{h}{e^2}\frac{1}{2\beta\nu^2}\,. \tag{3.8}$$

We note that, with $i, j = x, y$ $(i \neq j)$, the resistivity in units of h/e^2 is $\tilde{\rho}_{ii} \simeq \tilde{\sigma}_{jj}\nu^{-2}$, where $\tilde{\sigma}_{jj} = L_j/2L_i$ and L_i (L_j) is the mean free path along the i (j) direction. Without dislocations, $L_y \propto \nu^{-1}$, $L_x \propto \nu$, and $\tilde{\rho}_{xx} \propto \nu^{-4}$, while $\tilde{\rho}_{yy} \propto \nu^0$. With dislocations, $L_y \propto L_x \propto \nu$, i.e., $\tilde{\sigma}_{jj} \propto \nu^0$, and $\tilde{\rho}_{xx} \propto \tilde{\rho}_{yy} \propto \nu^{-2}$. Equations (3.7), (3.8) plotted as dashed lines in Figure. 3.4, can be obtained via replacement of hopping time of electrons between neighboring stripes $2\tau_B$ by $L_{\rm d}/v$, where v is the drift velocity of electron along the stripe. Equating Eq. (3.7) to Eq. (3.6) [or Eq. (3.8) to Eq. (3.2)], we find that the crossover to the dislocation limited transport happens at

$$\nu_{\rm d} \equiv \frac{\nu_1}{\sqrt{\beta}}\,. \tag{3.9}$$

With $\nu_{\rm d} \simeq 8$ and $\nu_1 \simeq 20$ we find $\beta = (\nu_1/\nu_{\rm d})^2 \simeq 6.3$. This value does not seem unreasonable and correctly accounts for the saturation of the anisotropy, $\rho_{xx}/\rho_{yy} = \beta^2 \approx 40$ [54].

3.5 Roadmap for future detection

Our experimental findings in $Al_xGa_{1-x}As$ quantum wells (Figure. 3.3) and in a clean GaAs quantum well (Figure. 3.4) can be unified in a phase diagram shown in Figure. 3.5 which treats σ_0/α^2 and $\tau_{\rm q}/\tau$ as independent parameters. Here, the QHS phase is observed above the horizontal line corresponding to $\nu_1 = 9/2$. To detect the hQHS phase, one should satisfy both $\nu_2 - \nu_1 > 1$ and $\nu_2 > 11/2$, since at least two half-integer filling factors are needed to establish the ν independence of the resistance. [2] As a

[2] The approximate condition for the hQHS phase detection is $\tilde{\sigma}_0 > \alpha^2(\tau/\tau_{\rm q})\max\{\tau/\tau_{\rm q}, 11/2\}$.

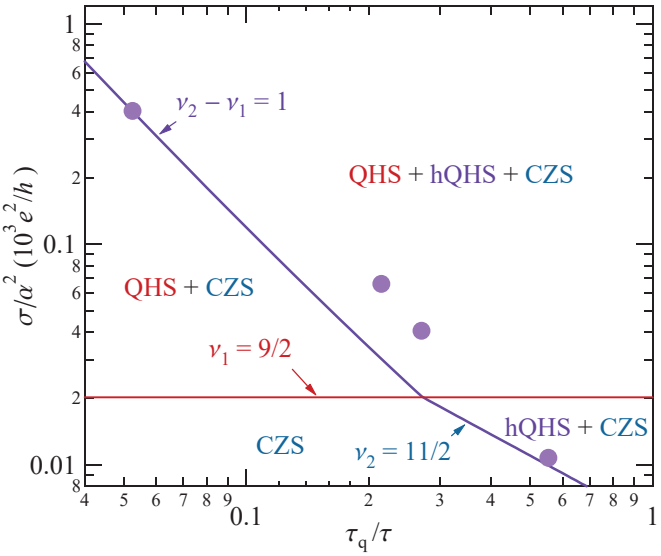

Figure 3.5: A diagram in the $(\tau_q/\tau, \sigma_0/\alpha^2)$ plane showing four regions marked by detectable phases. Circles are experimental data points from all four samples studied.

result, the most favorable conditions for the hQHS phase are realized at the top-right corner of the diagram. However, as demonstrated by our experiments on $Al_xGa_{1-x}As$ quantum wells, the hQHS can be detected at modest mobilities provided that the ratio τ_q/τ is sufficiently high. On the other hand, this ratio is much smaller in clean GaAs quantum wells, which makes the hQHS detection difficult in such systems despite their high mobility. The phase diagram shown in Figure. 3.5 provides a a road map for future experiments aiming to detect the hQHS phases.

In summary, we have observed hidden quantum Hall stripe (hQHS) phases [120] forming near half-integer filling factors of $Al_xGa_{1-x}As/Al_{0.24}Ga_{0.76}As$ quantum wells with varying x. These phases reside between the conventional stripe phases and the isotropic liquid phases and are characterized by isotropic resistivity that is not sensitive to the filling factor. Analysis of the experimental phase diagram reveals that the QHS density of states is smaller than predicted by the Hartree-Fock theory [3, 4], calling for improved theory. The unique transport characteristics of the hQHS phases should allow exploration of the stripe physics in 2D systems that, unlike GaAs, lack symmetry-breaking fields. On the other hand, ultrahigh mobility GaAs quantum wells favor conventional QHSs over hQHSs due to a shrinking filling factor range where the hQHS phases can form.

Chapter 4

Anomalous nematic states in high half-filled Landau levels

This chapter is adapted from X. Fu, Q. Shi, M. A. Zudov, G. C. Gardner, J. D. Watson, M. J. Manfra, K. W. Baldwin, L. N. Pfeiffer, and K. W. West, Anomalous nematic states in high half-filled Landau levels, *Phys. Rev. Lett.* **124**, 067601 (2020), and from X. Fu, Q. Shi, M. A. Zudov, G. C. Gardner, J. D. Watson, M. J. Manfra, K. W. Baldwin, L. N. Pfeiffer, and K. W. West, Anomalous nematic state to stripe phase transition driven by in-plane magnetic fields, *Phys. Rev. B* **104**, L081301 (2021), by permission of the American Physical Society under the American Physical Society reuse and permission license.

4.1 Introduction

The ground state of a two-dimensional electron gas (2DEG) at half-integer filling factors $\nu = i/2, i = 1, 3, 5, ...$, can depend sensitively on the Landau level (LL) index N. At $N = 0$ ($\nu = 1/2, 3/2$) it is a compressible composite fermion metal [28], whereas at $N = 1$ ($\nu = 5/2, 7/2$) it is an incompressible fractional quantum Hall insulator formed by paired composite fermions [137, 15]. It is a compressible composite fermion metal [28] at $N = 0$ ($\nu = 1/2, 3/2$) and an incompressible fractional quantum Hall insulator formed by paired composite fermions [137, 15] at $N = 1$ ($\nu = 5/2, 7/2$). At $N = 2$ and several higher LLs ($\nu = i/2, i = 9, 11, ...$), the competition between long-range repulsive

and short-range attractive components of Coulomb interaction leads to compressible charge-ordered phases [3, 98, 4]. These phases can be viewed as unidirectional charge-density waves consisting of stripes with alternating integer ν (e.g., $\nu = 4$ and $\nu = 5$) and are commonly known as quantum Hall stripes (QHSs). With further consideration of thermal and quantum fluctuations, several electron liquid crystal-like phases have also been proposed [51]. With few exceptions [36, 37], QHSs in a 2DEG confined to GaAs quantum wells align along $\langle 110 \rangle$ crystal axis of GaAs. This symmetry breaking field remains enigmatic, despite many efforts to identify its origin [114, 39, 40, 37].

The generic QHS features are a maxima (minima) in a longitudinal resistance R_{xx} (R_{yy}), which develop at temperatures $T \lesssim 0.1$ K, and a non-quantized Hall resistance R_H [5, 6]. More precisely, QHSs form when partial filling factor $\nu^\star = \nu - \lfloor \nu \rfloor$, where $\lfloor \nu \rfloor$ is an integral part of ν, falls in the range of $0.4 \lesssim \nu^\star \lesssim 0.6$. The resistance anisotropy ratio $\alpha_R \equiv R_{xx}/R_{yy}$ normally achieves a single maximal value $\alpha_R \gg 1$ at $\delta\nu \equiv \nu^\star - 0.5 \approx 0$ and quickly drops to $\alpha_R \approx 1$ at $\delta\nu \approx \pm 0.1$. This drop occurs due to a *monotonic* decrease (increase) of the R_{xx} (R_{yy}) with $|\delta\nu|$.

In this chapter, we report on anomalous nematic states (ANSs) which are distinguished from QHSs by minima (maxima) in R_{xx} (R_{yy}) and plateau-like features in R_H in half-filled $N \geq 3$ Landau levels. The global maxima (minima) in the R_{xx} (R_{yy}) occur away from half-filling, at $\delta\nu \approx \pm 0.08$, where the resistance anisotropy ratio attains its maximal value. Remarkably, all these features emerge at temperatures considerably lower than the onset temperature of QHSs, which indicates possible transition to a new phase.

Moreover, we report on the response of the ANSs to in-plane components of the magnetic-fields $B_\parallel = B_x$ and $B_\parallel = B_y$. We find that the immediate effects of $B_\parallel$ are to transform the minimum (maximum) in the R_{xx} (R_{yy}) at half-filling into a maximum (minimum), to eliminate the plateau in R_H, and to restore the ratio R_{xx}/R_{yy} to values consistent with the QHS phases. Remarkably, the ANSs respond to $B_\parallel$ in essentially the same manner when $B_\parallel$ is applied along either the $\hat{x} \equiv \langle 1\bar{1}0 \rangle$ or the $\hat{y} \equiv \langle 110 \rangle$ direction; in both cases the revived QHS phase is aligned along its native $\langle 110 \rangle$ crystal axis. This is in contrast with the effect of $B_\parallel$ on the QHS phases which respond very differently to B_x and B_y whereas persisting to much higher $B_\parallel$ [42, 41, 115]. These observations signal that a modest $B_\parallel \approx 0.5$ T is enough to tip a delicate balance between the ANSs

and the QHS phases in favor of the latter, a finding which should be taken into account by theories aimed to explain the origin of the ANSs.

4.2 Anomalous reduced anisotropy and plateau-like features in the Hall at $\nu \approx 13/2$

The 2DEG in sample A (B) resides in a GaAs quantum well of width 29 nm (30 nm) surrounded by $Al_{0.24}Ga_{0.76}As$ barriers. After a brief low-temperature illumination, samples nominally had the electron density $n_e \approx 3.0 \times 10^{11}$ cm^{-2} and the mobility $\mu \gtrsim 2 \times 10^7$ cm^{2}V^{-1}s^{-1}. Samples were 4×4 mm squares with indium contacts fabricated at the corners and the midsides. We note that signatures of anomalous nematic states have also been observed in Hall bar geometry. R_{xx} (R_{yy}) was measured using a four-terminal, low-frequency lock-in technique, with the current sent between mid-side contacts along $\hat{x} \equiv \langle 1\bar{1}0 \rangle$ ($\hat{y} \equiv \langle 110 \rangle$) direction. R_H was measured concurrently with R_{xx}.

In Figure. 4.1(a) we present R_{xx} and R_{yy} versus magnetic field B measured in sample A at $T \approx 25$ mK. Near $\nu = 11/2, 15/2$, and $\nu = 17/2$, R_{xx} (R_{yy}) exhibits maxima (minima), with $R_{xx} \gg R_{yy}$, as expected of the usual QHS phases. Remarkably, the behavior in the vicinity of $\nu = 13/2$ is qualitatively different; even though $R_{xx} \gg R_{yy}$ (like at other $\nu = i/2$), R_{xx} exhibits a pronounced *minimum* whereas R_{yy} shows a *maximum* near half-filling. The global maxima (minima) in R_{xx} (R_{yy}) occur away from half-filling, namely near $\nu = 13/2 \pm 0.08$, as illustrated by vertical dashed lines. As a result, α_R becomes a *non-monotonic* function of $|\delta\nu| = |\nu^\star - 0.5|$; it is relatively small at $\delta\nu = 0$ and exhibits maxima at $\delta\nu \approx \pm 0.08$. The variation of α_R with $\nu^\star$ is quite significant, it drops from $\alpha_R > 600$ at $\nu = \nu_+ \approx 6.58$ to $\alpha_R < 10$ near half-filling.

In Figure. 4.1(b) we show the Hall resistance R_H as a function of B. Concurrent with the unexpected extrema in R_{xx} and R_{yy} at $\nu = 13/2$, the Hall resistance shows a plateau-like feature, marked by solid horizontal lines drawn at $2R_K/13$, where $R_K \equiv h/e^2$ is the von Klitzing constant. While the plateau-like feature in R_H near $\nu = 13/2$ is very close to $2R_K/13$, as one would expect for a developing even-denominator quantum Hall state, its appearance might be coincidental. Indeed, steps in R_H are also present near $\nu = 11/2$ and $\nu = 15/2$, albeit in these cases R_H is noticeably lower than half-integer-quantized values (cf. dashed horizontal line segments drawn at $2R_K/11$ and $2R_K/15$. In

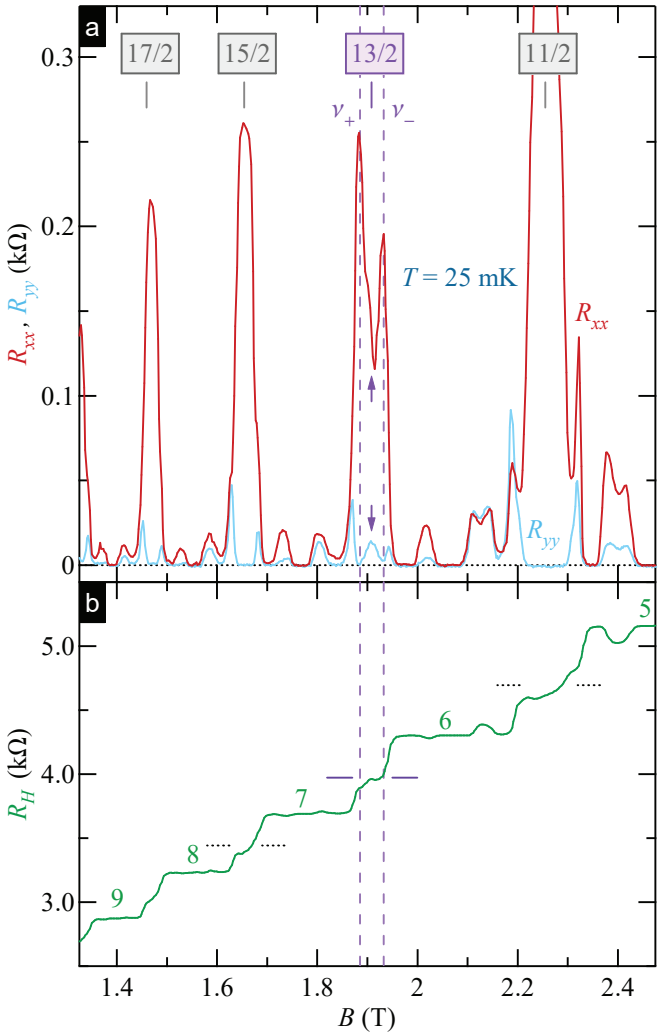

Figure 4.1: (Color online) (a) R_{xx} and R_{yy} versus B measured in sample A at $T \approx 25$ mK. Half-integer ν are marked by $15/2, 13/2$, and $11/2$. The R_{xx} minimum and the R_{yy} maximum at $\nu \approx 13/2$ are marked by $\uparrow$ and $\downarrow$, respectively. Dashed vertical lines are drawn at $\nu_\pm = 6.5 \pm 0.08$. (b) Hall resistance R_H versus B. Solid horizontal lines, drawn at $2R_K/13$, mark a plateau-like feature near $\nu = 13/2$, while dashed horizontal lines are drawn at $2R_K/11$ ($\nu = 11/2$) and $2R_K/15$ ($\nu = 15/2$), where $R_K \equiv h/e^2 = 25812.80745$ Ω is the von Klitzing constant.

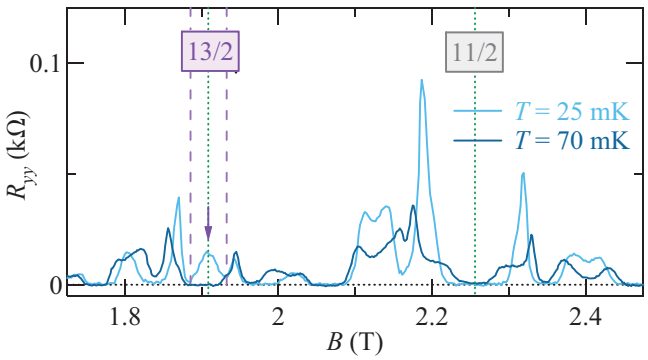

Figure 4.2: (Color online) R_{yy} versus B measured in the sample A at $T \approx 25$ mK (light line) and at $T \approx 70$ mK (dark line). Half-integer ν are marked by 13/2, and 11/2.

addition, even at $\nu = 13/2$, R_H often differs from $2R_K/13$ when measured concurrently with R_{yy}. We notice, however, that signatures of even-denominator quantum Hall states were recently observed in the $N = 3$ LL of graphene [138]. It was also established that in AlAs quantum wells, Hall quantization at $\nu = 3/2$ can occur in anisotropic setting and be accompanied by a maximum in easy resistance [139]. Finally, fractional quantum Hall nematic states have been reported at $\nu = 7/3$ [140] and $\nu = 5/2$ [141] in tilted magnetic fields.

4.3 Probing the ground states at low temperature

The anomalous nematic state near $\nu = 13/2$ depicted in Figure. 4.1 is best observed at low temperatures. As a glimpse at the temperature dependence, we present in Figure. 4.2 the easy resistance R_{yy} as a function of B measured in sample A at two different temperatures. Remarkably, as the temperature is raised from $T \approx 25$ mK to $T \approx 70$ mK, the two R_{yy} minima near $\nu = 13/2 \pm 0.08$ and the maximum near $\nu = 13/2$ are replaced by *single* minimum, centered at $\nu = 13/2$ with $R_{yy} \approx 0$. Such a broad minimum is a characteristic feature of the well-developed QHS phase. In contrast, the broad minimum near $\nu = 11/2$ observed at $T \approx 25$ mK becomes narrower at $T \approx 70$ mK, consistent with previous studies of QHSs. These data demonstrate that unexpected extrema near $\nu = 13/2$ emerge at temperatures lower than the onset temperature of QHSs.

4.4 Anomalous nematic state at more half-fillings

Some of our samples revealed the unexpected R_{xx} minima not only near $\nu = 13/2$, as in Figure. 4.1, but also near other half-integer ν. We note that, Anomalous nematic states are very fragile and the R_{yy} maxima near $\nu = i/2$ are more elusive than the R_{xx} minima. As for other fragile states in quantum Hall systems forming below 0.1 K, the uniformity of the carrier density is obviously an important factor. Another requirement is a good sample "state" which, we believe, is determined by the disorder landscape. The latter, in turn, sensitively depends on the details of both cooldown and illumination procedures, which are known to produce charge redistribution between the quantum well, the doping layers, and the sample surface [142, 143, 144], thereby leading to different degrees of screening of the disorder potential [135]. Nevertheless, after multiple cooldowns of different samples we are confident that the phenomenon is generic. In Figure. 4.3 we show the data obtained from sample B which exhibit pronounced R_{xx} minima at $\nu = 13/2, 15/2$, and $17/2$. All of these minima are accompanied by plateau-like features in R_H, see right axis, which assumes the values close to $2R_{\rm K}/i$, with $i = 13, 15, 17$, as indicated by horizontal line segments in Figure. 4.3. Moreover, R_{xx} maxima occur nearly precisely at the same $\nu^\star$ as in Figure. 4.1, i.e., at $\nu^\star = 1/2 \pm 0.08$, as illustrated by vertical dashed lines. Whether or not the value of $|\delta\nu| = 0.08$ is universal remains an open question.

We now turn to the temperature dependence in sample B which is illustrated in Figure. 4.4(a) showing R_{xx} (dark line) and R_{yy} (light line) as a function of B measured at different T, as marked. The Hall resistances R_H measured at $T \approx 135$ mK (light line) and $T \approx 30$ mK (dark line) are shown in Figure. 4.4(b). At $T \approx 135$ mK, R_{xx} and R_{yy} near $\nu = 11/2$ and $\nu = 15/2$ are featureless and R_H is classical. At $\nu \approx 13/2$, however, the anisotropy is already developed ($\alpha_R \approx 6$) and R_H shows a clear signature of a re-entrant integer quantum Hall state near $\nu \approx 6.72$ (as marked by $\uparrow$ in the figure), indicative of a bubble phase. As anticipated, R_{xx} (R_{yy}) exhibits a single maximum (minimum) at $\nu \approx 13/2$, i.e., the strongest anisotropy occurs close to half-filling, consistent with nearly all previous experiments. [1] The fact that transport anisotropies in the lower-spin branches of a LL develop at higher temperatures (e.g.,

[1] We are aware of only two experiments which observed maximum resistance anisotropy at $\nu^\star > 0.5$ [145, 53].

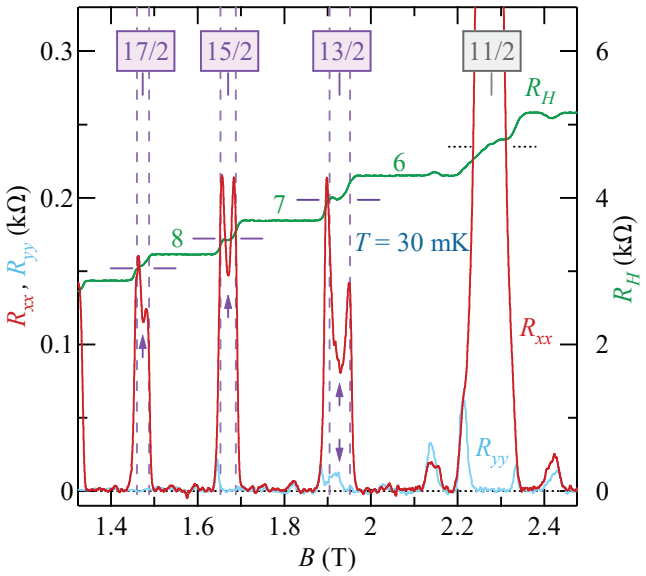

Figure 4.3: (Color online) R_{xx}, R_{yy} (left axis), and R_H (right axis) versus B measured in sample B at $T \approx 30$ mK. Half-integer ν are marked by $17/2, 15/2, 13/2$, and $11/2$. The R_{xx} minima at $\nu = 13/2, 15/2, 17/2$ and the R_{yy} maximum near $\nu = 13/2$ are marked by $\uparrow$ and $\downarrow$, respectively. Dashed vertical lines are drawn at $\nu_{\pm} = i/2 \pm 0.08$, $i = 13, 15, 17$. Near $\nu = i/2$ ($i = 13, 15, 17$), R_H shows plateau-like features with $R_H \approx 2R_{\rm K}/i$, marked by solid horizontal lines.

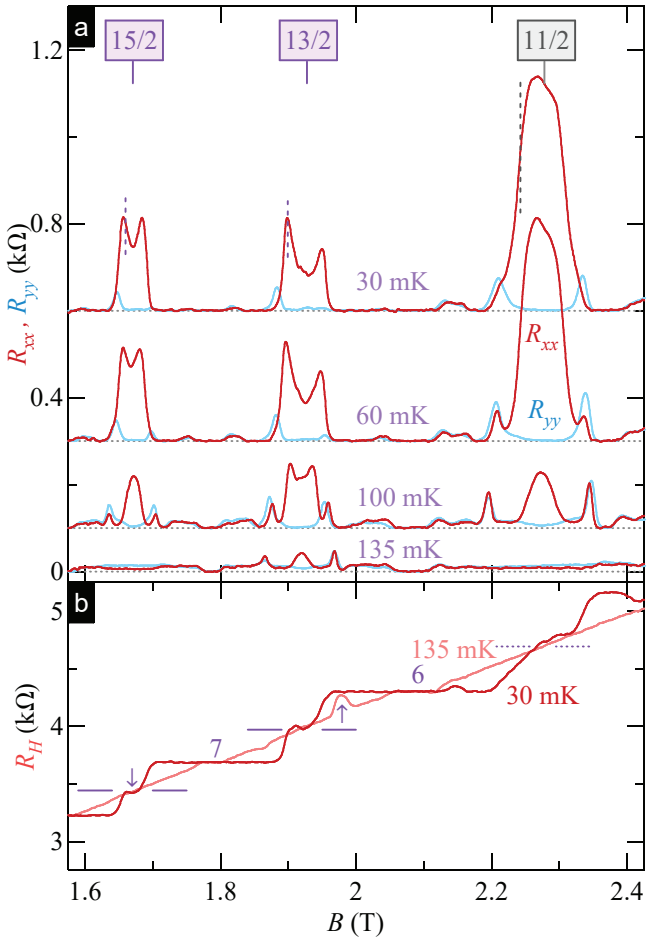

Figure 4.4: (Color online) (a) R_{xx} (dark line), R_{yy} (light line) versus B measured in sample B at $T \approx 135$ mK (bottom), $T \approx 100$ mK (offset by 0.1 kΩ), $T \approx 60$ mK (offset by 0.3 kΩ), and $T \approx 30$ mK (offset by 0.6 kΩ). Vertical dashed lines mark $\nu^\star = 0.58$. (b) R_H versus B at $T \approx 30$ mK (dark line) and at $T \approx 135$ mK (light line). Solid horizontal lines next to the R_H mark concurrent plateau-like features at $2R_K/13$ and $2R_K/15$, while dashed horizontal lines are drawn at $2R_K/11$.

$\nu \approx 9/2, 13/2$) than in the upper-spin branches ($\nu \approx 11/2, 15/2$) is well documented (see, e.g., Ref. [5]).

Upon cooling to $T \approx 100$ mK, transport anisotropy with a maximum in R_{xx} and a minimum in R_{yy} also emerges at both $\nu \approx 11/2$ ($\alpha_R \approx 20$) and at $\nu \approx 15/2$ ($\alpha_R \approx 30$). Near $\nu \approx 13/2$, however, even though the anisotropy becomes an order of magnitude stronger ($\alpha_R \approx 60$), R_{xx} now exhibits a pronounced *minimum* near half-filling indicating an onset of the anomalous nematic state. When the sample is cooled to $T \approx 60$ mK, the resistance anisotropy at $\nu \approx 11/2$ increases dramatically ($\alpha_R > 300$), in agreement with previous studies. Concurrently, we observe that the R_{xx} minimum at $\nu \approx 13/2$ deepens and that the resistance anisotropy is *reduced* by about a factor of three compared to its value at $T \approx 100$ mK. Remarkably, the R_{xx} near $\nu \approx 15/2$ also develops a minimum at this temperature. At $T \approx 30$ mK, the magnetotransport near $\nu = 11/2$ remains qualitatively unchanged, although the anisotropy ratio becomes even higher ($\alpha_R \approx 400$). Near $\nu = 13/2$, however, further development of the R_{xx} minimum and the appearance of the R_{yy} maximum reduce the anisotropy to $\alpha_R \approx 10$. While we do not observe a maximum in the R_{yy} near $\nu = 15/2$, the R_{xx} minimum becomes more pronounced and the anisotropy reduces to $\alpha_R < 20$. As previously noted, the R_{xx} minima near $\nu = 13/2$ and $\nu = 15/2$ are accompanied by plateau-like features in R_H, see Figure. 4.4(b).

It is evident that the temperature dependencies near $\nu = 13/2$ and $\nu = 15/2$ are qualitatively similar. At temperatures immediately below the onset temperature at which the QHS anisotropies sets in, the data at both filling factors exhibit normal behavior, i.e., a broad single maximum (minimum) in the R_{xx} (R_{yy}). Upon cooling down further, both filling factors demonstrate the gradual development of the "splitting" in the R_{xx}, around half-filling, marked by a reduction of the anisotropy ratio and by the emergence of plateau-like features in the R_H. We can thus conclude that, while definitely more robust in the lower spin branch, the anomalous nematic state is also supported by the upper spin branch.

The contrasting behavior between temperature dependencies of the R_{xx} (circles) and of the R_{yy} (squares) near $\nu = 13/2, 15/2$ and those near $\nu = 11/2$ are summarized in Figure. 4.5. While R_{xx} (R_{yy}) at $\nu \approx 11/2$ monotonically increases (decreases) as the temperature is lowered, R_{xx} (R_{yy}) at both $\nu = 13/2$ and $\nu = 15/2$ shows a clear maximum (minimum) at some intermediate "turnover" temperatures, $T^{\star}_{13/2} \approx 100$ mK and

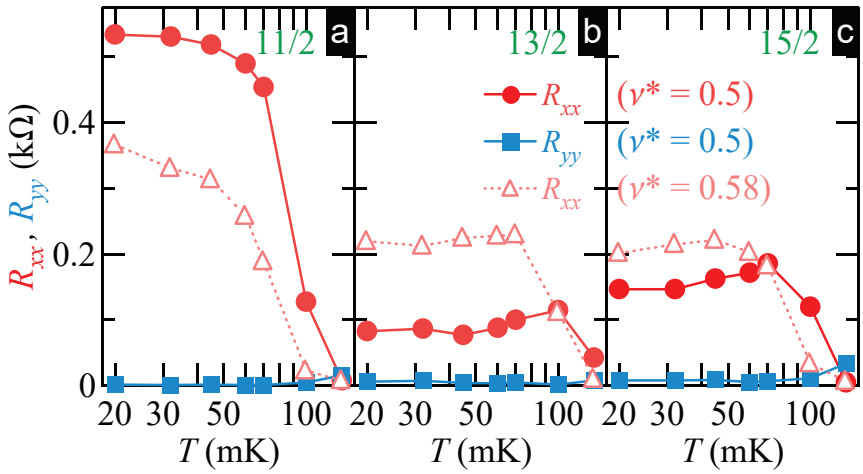

Figure 4.5: (Color online) R_{xx} (circles), R_{yy} (squares) versus T at (a) $\nu = 11/2$, (b) $\nu = 13/2$, and (c) $\nu = 15/2$. For comparison, R_{xx} at $\nu^\star = 0.58$, cf. dashed vertical lines in Figure. 4.4(a), versus T is shown by triangles.

$T^\star_{15/2} \approx 70$ mK, respectively. We note that, A turnover in the temperature dependence has been observed previously [146, 53], but no local resistance extrema near $\nu^\star = 0.5$ have been reported to date. For comparison, we also include in Figure. 4.5 the R_{xx} data at $\nu = i/2 + 0.08$ ($i = 11, 13, 15$), represented by triangles. As can be seen in Figure. 4.5(a), R_{xx} at $\nu = 5.58$ is always smaller than that at $\nu = 11/2$ at all temperatures studied. In contrast, R_{xx} at $\nu = i/2 + 0.08$ ($i = 13, 15$) is smaller than that at $\nu = i/2$ *only* when $T > T^\star_{i/2}$ but not when $T < T^\star_{i/2}$. This observation further confirms that filling factors $\nu = i/2$ ($i = 13, 15$) are governed by the same physics which sets in at $T \approx T^\star_{i/2}$ and is considerably more effective at reducing the transport anisotropy at $\nu = i/2$ than away from half-filling. Indeed, the temperature dependencies of the R_{xx} at $\nu = 6.58, 7.58$ are rather similar to that at $\nu = 5.58$.

According to the transport theory of QHS phase, which treats it as a pinned smectic [52], the decrease (increase) of R_{xx} (R_{yy}) upon cooling can be attributed to the enhanced electron scattering between stripe edges. This model, however, predicts *weaker* anisotropy away from half-filling than at $\nu = i/2$, in contrast to our observations. In addition, Ref. [52] predicts considerably stronger T-dependence of R_{xx} and R_{yy} at $\nu = i/2$ than away from half filling. At $\nu^\star = 1/2$, Ref. [52] predicts $\rho_{xx} \propto T^{-\alpha}$ and $\rho_{yy} \propto T^{\alpha}$ with $\alpha \approx 0.5$. Our data do not reflect that. Therefore, the observed dependencies on

ν and T are inconsistent with QHS or a nematic-to-smectic transition [53]. Instead, the observed low-temperature emergence of unexpected extrema in R_{xx} and R_{yy} along with the plateau-like features in R_H likely reflects the formation of another competing ground state.

In addition to the temperature dependence, it is interesting to investigate the effects of the carrier density and of the in-plane magnetic field. Our measurements on a tunable-density Van der Pauw device with in-situ back gate have *not* revealed these anomalous states at *any* density from 2.2 to 3.6×10^{11} cm^{-2} [46], as neither have those using high density [$n_e = (4.1 - 4.3) \times 10^{11}$ cm^{-2}] heterostructures [38]. However, the carrier mobilities of samples used in the above experiments were below 1.2×10^7 cm ^{2} V^{-1}s^{-1} and, since the anomalous nematic states form at considerably lower temperatures than QHSs, it is reasonable to expect that they are more easily destroyed by disorder. The absence of anomalous nematic states in these more-disordered samples yields further support to the importance of electron-electron correlations. Measurements in tilted magnetic fields are currently under way and will be a subject of future publication. We note, however, that the effect of in-plane magnetic field remains poorly understood even for conventional QHSs [47, 115, 46] which might complicate the interpretation of the data.

4.5 Anomalous nematic state to stripe phase transition driven by in-plane magnetic fields

We report the anomalous nematic state to stripe phase transition driven by in-plane magnetic fields with two samples below. Our samples are 30 nm-wide GaAs quantum well surrounded by $Al_{0.24}Ga_{0.76}As$ barriers. The electrons are supplied by Si doping in narrow GaAs doping wells, sandwiched between thin AlAs layers, which are positioned at a setback distance of 80 nm on both sides of the main GaAs well. After a brief illumination at $T \approx 5$ K, the electrons had a density $n_e \approx 3.0 \times 10^{11}$ cm^{-2} and a mobility $\mu \gtrsim 2 \times 10^7$ cm^{2}V^{-1}s^{-1}. Samples were 4×4 -mm squares with eight indium contacts at the corners and the midsides. The longitudinal resistances, R_{xx} and R_{yy}, were measured using a four-terminal, low-frequency (a few hertz) lock-in technique. The excitation current was sent through the center of the sample, i.e., between mid-side

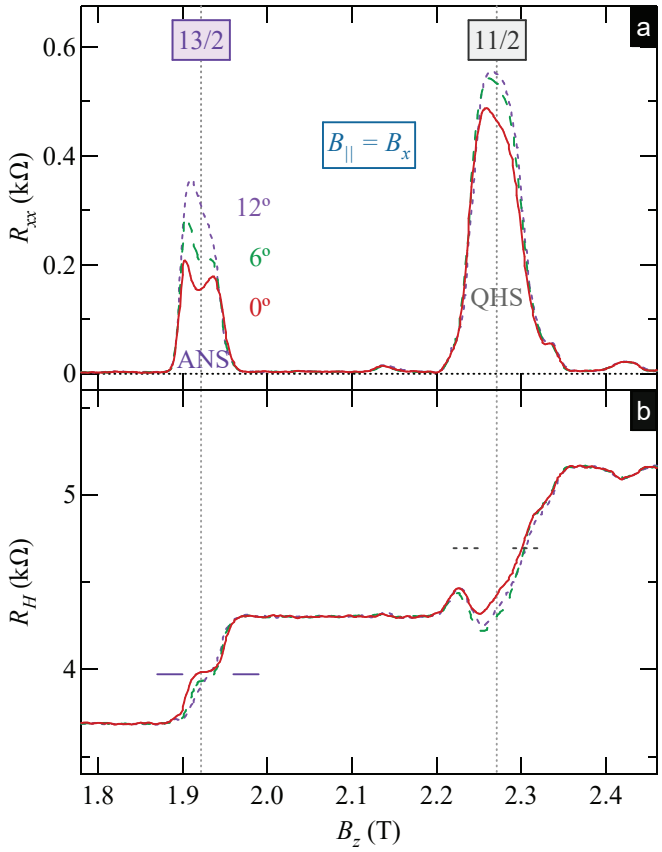

Figure 4.6: (a) R_{xx} and (b) R_H as a function of B_z measured under $B_{||} = B_y$ at $\theta = 0°$ (solid line), 6° (dashed line), and 12° (dotted line) at $T \approx 20$ mK. Horizontal solid (dashed) lines in (b) are drawn at $R_H = 2R_K/13$ ($R_H = 2R_K/11$), where $R_K = h/e^2$ is the von Klitzing constant.

contacts along $\hat{x}$ or $\hat{y}$ direction. The in-plane magnetic field B_x or B_y was introduced by tilting the sample about either $\hat{y}$ or $\hat{x}$ axis, in separate cooldowns.

4.5.1 Effect of $B_{||} = B_x$

We start with the discussion of the experiments under $B_{||} = B_x$ (i.e., applied along the $\langle 1\bar{1}0 \rangle$ crystal axis) and compare its effects on the QHS phase and on the ANS. In Figs. 4.6 (a) [4.6(b)] we show the longitudinal [Hall] resistance R_{xx} [R_H] as a function of the perpendicular component of the magnetic field B_z at different tilt angles $\theta = 0°$ (solid lines), 6° (dashed lines), and 12° (dotted lines). Consistent with findings of Ref. [136],

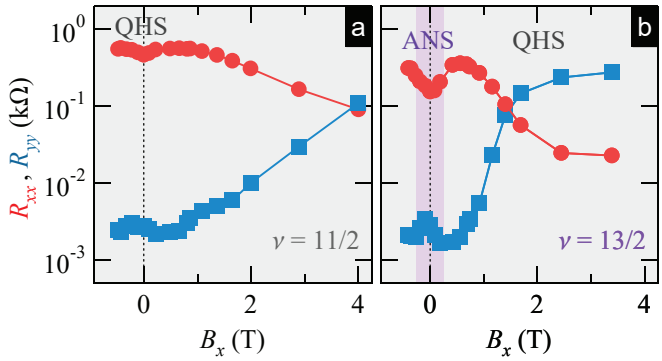

Figure 4.7: (a) R_{xx} (circles), R_{yy} (squares) vs. B_x at $\nu \approx 11/2$. (b) Same as (a) but at $\nu \approx 13/2$.

the data at $B_{\|} = 0$ reveal the QHS phase at $\nu = 11/2$ and the ANS at $\nu = 13/2$. The ANS at $\nu = 13/2$ is evidenced by (i) a minimum in the R_{xx}, with the resistance value much smaller than typical of a QHS phase, and by (ii) an incipient plateau in the R_H with the value close to $R_H = 2R_K/13$, as marked by horizontal solid lines. None of these features are present at $\nu = 11/2$ where the data reflect a conventional QHS phase.

Upon tilting the sample to introduce $B_{\|} = B_x$, the R_{xx} minimum at $\nu = 13/2$ becomes less pronounced at $\theta = 7^\circ$ and disappears completely at $\theta = 12^\circ$. We note that, While the maximum is shifted away from half-filling towards larger ν, it not uncommon for QHS phases to exhibit such shift both in tilted [145] and perpendicular [53] fields. The plateau in the R_H is also destroyed by B_x at this filling factor. As a result, both the R_{xx} and the R_H at $\nu = 13/2$ become akin to those at $\nu = 11/2$, hinting at a $B_{\|}$-driven transition from the ANS to the QHS phase. In contrast, the data at $\nu = 11/2$, representing the QHS phase, exhibit no qualitative changes with increasing B_x in this range of tilt angles, despite higher B_x.

To further analyze the effects of $B_{\|} = B_x$ on the QHS phase at $\nu = 11/2$ and on the ANS at $\nu = 13/2$ we construct Figs. 4.7 (a) and Figs. 4.7 (b), respectively, which show the R_{xx} (circles) and the R_{yy} (squares) as a function of B_x covering a wider range of tilt angles. The R_{xx} (R_{yy}) at $\nu = 11/2$ remains nearly unchanged up to $B_x \approx 1$ T and then gradually decays (grows) until the anisotropy disappears at $B_x \approx 4$ T, in agreement with earlier experiments [115]. In contrast, the R_{xx} at $\nu = 13/2$ shows a pronounced maximum at $B_x \approx 0.5$ T, whereas the R_{yy} shows a deep minimum at the same B_x. As

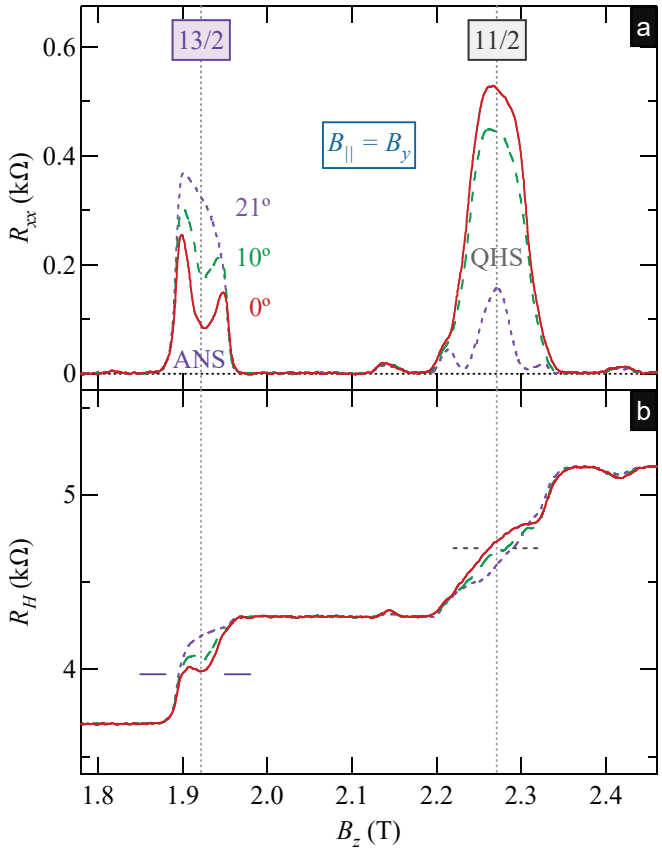

Figure 4.8: (a) R_{xx} and (b) R_H as a function of B_z under $B_{||} = B_y$ at $\theta = 0°$ (solid line), 10° (dashed line), and 21° (dotted line) at $T \approx 20$ mK. Horizontal solid (dashed) lines in (b) are drawn at $R_H = 2R_K/13$ ($R_H = 2R_K/11$).

a result, the anisotropy ratio R_{xx}/R_{yy} increases considerably and becomes consistent with the value exhibited by the QHS phase at $\nu = 11/2$. Upon further increase of B_x, both the R_{xx} and the R_{yy} at $\nu = 13/2$ evolve as expected for the QHS phase; here, the anisotropy vanishes at $B_x \approx 1.5$ T, which is lower than the corresponding B_x at $\nu = 11/2$ and the QHS phase realigns along the $\langle 1\bar{1}0 \rangle$ axis at still higher B_x, as anticipated [115].

4.5.2 Effect of $B_{||} = B_y$

To acquire further support to the $B_{||}$-driven ANS-to-QHS phase transition at $\nu = 13/2$ we next present the data under orthogonal orientation of $B_{||}$ with respect to the

anisotropy axis, $B_{\|} = B_y$. In Figure. 4.8 (a) we show the R_{xx} as a function of B_z at $T \approx 20$ mK under $B_{\|} = B_y$ (i.e., applied along $\langle 110 \rangle$ crystal axis) at three tilt angles, $\theta = 0^\circ$ (solid line), 10° (dashed line) and 21° (dotted line). The Hall resistance data are presented in Figure. 4.8 (b). At $\theta = 0^\circ$, the data are similar to those obtained in another cooldown, cf. Figure. 4.6; both the R_{xx} and the R_H exhibit all characteristic features of the QHS phase at $\nu = 11/2$ and of the ANS at $\nu = 13/2$. It is also evident that in this cooldown the ANS is better developed, as evidenced by a deeper minimum in the R_{xx}. As discussed in Ref. [136], the strength of the ANS sensitively depends on the details of the cool down and illumination protocols.

The evolution of the R_{xx} in the QHS phase at $\nu = 11/2$ with B_y is consistent with previous studies [47, 115]. Upon tilting to $\theta = 10^\circ$, the R_{xx} decreases, as the QHS phase starts to reorient perpendicular to B_y [42, 41, 47, 115], and at $\theta = 21^\circ$ the R_{xx} is reduced much more. In contrast to the R_{xx} at $\nu = 11/2$, the R_{xx} at $\nu = 13/2$ *grows* with the tilt angle and the characteristic ANS minimum quickly disappears. Indeed, at $\theta = 21^\circ$ the R_{xx} near $\nu = 13/2$ exhibits a single maximum, as expected of a QHS phase. As shown in Figure. 4.8 (b) the Hall plateau with $R_H \approx 2R_{\rm K}/13$ is also destroyed by B_y. We thus conclude that the effect of B_y on the ANS is essentially the same as that of B_x; in either case, the ANS yields to the QHS phase once a modest $B_{\|}$ is introduced.

In Figure. 4.9 we summarize the evolution of both the R_{xx} (circles) and the R_{yy} (squares) near (a) $\nu = 11/2$ and (b) near $\nu = 13/2$ over the whole range of B_y studied. The data at $\nu = 11/2$ reveal two reorientations of the QHS phase; B_y first realigns the QHS phase along the $\langle 1\bar{1}0 \rangle$ crystal axis (perpendicular to $B_{\|}$) at $B_y \approx 1$ T and then back to along the $\langle 110 \rangle$ axis (parallel to $B_{\|}$) at $B_y \approx 3$ T, as previously reported [115, 46]. At $\nu = 13/2$, however, the data in Figure. 4.9 (b) show that the immediate effect of B_y is to dramatically *increase* (*decrease*) the R_{xx} (R_{yy}) to a value consistent with the QHS phase. Interestingly, unlike the QHS phase at $\nu = 11/2$, the revived QHS phase at $\nu = 13/2$ preserves its native orientation at all values of B_y. The second reorientation at $\nu = 11/2$ was attributed to another $B_{\|}$-induced symmetry breaking mechanism which favors the QHS alignment parallel to $B_{\|}$ [115]. This second mechanism is stronger at $\nu = 13/2$ than at $\nu = 11/2$, i.e., it turns on at lower $B_{\|}$ [115]. Therefore, it seems plausible that at $\nu = 13/2$, the second symmetry breaking mechanism dominates over the first starting from very small B_y. While such scenario has not been explicitly

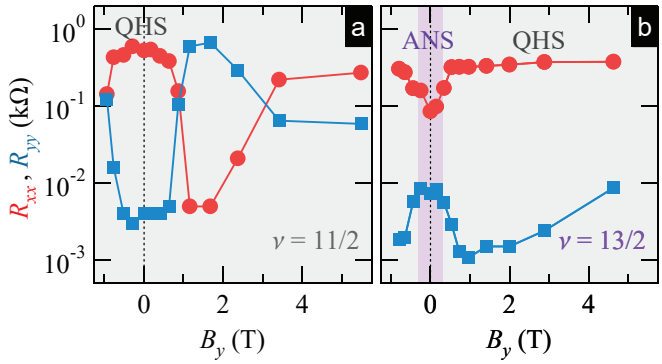

Figure 4.9: (a) R_{xx} (circles), R_{yy} (squares) vs B_y at $\nu \approx 11/2$. (b) Same as (a) but at $\nu \approx 13/2$.

discussed in the literature, it is known that the QHS orientation can remain immune to B_y [46]. As a result of these changes, the resistance anisotropy ratio grows from $R_{xx}/R_{yy} \approx 10$ at $B_y = 0$ to $R_{xx}/R_{yy} \approx 300$ at $B_y \approx 1$ T. This fact further supports the B_y-driven ANS-to-QHS transition, consistent with our findings under small $B_{\|} = B_x$.

4.5.3 Discussions

Having concluded that both B_x and B_y transform the ANS to the QHS phase with native orientation, we next comment on possible mechanisms behind this transition. Let us first assume that the energetics of the ANS phase is not altered by $B_{\|}$. According to the calculations of the QHS phases under $B_{\|}$ [43, 44], $B_{\|}$ serves as an external symmetry-breaking field which either competes with ($B_{\|} = B_y$) or assists ($B_{\|} = B_x$) the native field, responsible for the QHS phase alignment along the $\langle 110 \rangle$ direction at $B_{\|} = 0$. As a result, B_x (B_y) lowers (raises) the energy of the QHS phase with native orientation with respect to its value at $B_{\|} = 0$. Consistent with this picture,our QHS phase data at $\nu = 11/2$ indeed show that B_x (B_y) initially raises (lowers) the anisotropy ratio R_{xx}/R_{yy}. The situation at $\nu = 13/2$, however, is markedly different. Here, the QHS phase should win over (lose to) the competing ANS as it must become more (less) energetically favorable under modest B_x (B_y). Although this prediction is consistent with our data under B_x, it clearly contradicts our observation of the ANS-to-QHS phase transition under B_y. Furthermore, even though the theory [43, 44] dictates that B_x lowers the energy of the QHS phase with its native orientation, all previous

transport studies [41, 115] have shown that the anisotropy ratio R_{xx}/R_{yy} at $\nu = 13/2$ is, in fact, *reduced* by B_x. Our data at $\nu = 13/2$, on the other hand, clearly show significant increase in the R_{xx}/R_{yy} once B_x is turned on. Based on the above arguments, we can conclude that $B_\parallel$, regardless of its orientation, raises the energy of the ANS above its value at $B_\parallel = 0$, making it less favorable than the QHS phase at modest $B_\parallel$.

Distinct effects of B_y on the ANS and on the QHS phase are further highlighted by opposite dependencies on the detuning $|\delta\nu|$ from half-filling. Indeed, near $\nu = 13/2$, the response of the ANS to B_y is obviously the strongest at $\delta\nu = 0$ resulting in the disappearance of the R_{xx} minimum and the restoration of a single maximum. This is in contrast to the QHS phase near $\nu = 11/2$, at which two deep R_{xx} minima emerge *away* from half-filling at $\theta = 21^\circ$. These minima appear because lower B_y is required to reorient the QHS phase perpendicular to $B_\parallel$ away from half-filling than at $\delta\nu = 0$ [47].

It is interesting to note that the local minimum in the hard resistance and the maximum in the easy resistance, as found in the ANS at $\delta\nu = 0$ without an in-plane magnetic field, can also be realized under $B_\parallel = B_y$ when the QHS phase is about to complete its reorientation perpendicular to $B_\parallel$, see, e.g., Fig. 1(e) in Ref. [47]. Such dependencies on $\delta\nu$ can be attributed to a possible decrease in the native symmetry breaking field as one moves away from half-filling [47]. However, if one were to treat the ANS as the QHS phase, the opposite conclusion emerges. Indeed, both the reduced anisotropy at $B_\parallel = 0$ and the stronger effects of $B_\parallel$ at $\delta\nu = 0$ would suggest that the native field is the weakest at half-filling. It seems unlikely that the $\delta\nu$ dependencies of the native field be so drastically different at $\nu = 13/2$ and at $\nu = 11/2$. We note, however, that there is not always a *direct* correlation between the strength of the symmetry breaking field, either native or external, and the observed resistance anisotropy. Indeed, one recent study has shown that the QHS phases can be aligned orthogonal to the direction dictated by the symmetry breaking potential [145]. Furthermore, under certain disorder parameters the resistance anisotropy can vanish altogether, even when the underlying stripe structure is preserved [120, 147].

To summarize, we have observed a transition from the anomalous nematic state to the quantum Hall stripe phase upon application of the a modest in-plane magnetic field, highlighting tight competition between these two ground states. The transition occurs both when $B_\parallel$ is aligned along the $\langle 110 \rangle$ and along the $\langle 1\bar{1}0 \rangle$ crystal axis of GaAs and

the resultant quantum Hall stripe phase is aligned along native the $\langle 110 \rangle$ direction. Our analysis suggests that $B_{\|}$ likely raises the energy of the ANS compared to its value at $B_{\|} = 0$. These findings further distinguish anomalous nematic states from other ground states in half-filled Landau levels.

Chapter 5

Microwave-induced resistance oscillations in a back-gated GaAs quantum well

This chapter is adapted from X. Fu, Q. A. Ebner, Q. Shi, M. A. Zudov, Q. Qian, J. D. Watson, and M. J. Manfra, Microwave-induced resistance oscillations in a back-gated GaAs quantum well, *Phys. Rev. B* **95**, 235415 (2017), and from X. Fu, M. D. Borisov, M. A. Zudov, Q. Qian, J. D. Watson, and M. J. Manfra, Effect of density on microwave-induced resistance oscillations in back-gated GaAs quantum wells, *Phys. Rev. B* **98**, 121303(R) (2018), by permission of the American Physical Society under the American Physical Society reuse and permission license.

In this chapter, we investigate how microwave-induced resistance oscillations evolve with the carrier density n_e in a GaAs/AlGaAs quantum well equipped with an *in situ* grown back gate, an aspect which has not been previously explored. First, we show that the MIRO frequency monotonically decreases with n_e. This finding can be linked to the renormalization of the effective mass by electron-electron interactions, which are sensitive both to n_e and to quantum confinement of our 2DEG. Second, we find that the MIRO amplitude substantially increases with n_e. While higher n_e leads to a larger radiation absorption (larger P) and a longer τ_q, both of which favor such an increase, these effects should be completely overwhelmed by the anticipated concomitant decrease

in η. Remarkably, however, our analysis of the MIRO amplitude is incompatible with such a decrease, showing just the opposite trend, i.e., that η steadily increases with n_e. Finally, we observe that the fundamental oscillation maximum moves towards the cyclotron resonance with increasing n_e. Taken together, these unexpected findings indicate that our understanding of microwave photoresistance remains incomplete, calling for futher theoretical and experimental studies.

5.1 Probing the effective mass dependent on the density

5.1.1 Ways to probe effective mass

It is well established that the effective electron mass $m^\star$ in GaAs/AlGaAs-based two-dimensional electron gas (2DEG) can deviate from the band mass of bulk GaAs, $m_b = 0.067\, m_0$ (m_0 is the free electron mass). One cause for this deviation is the non-parabolicity of the GaAs conduction band which leads to an enhancement of $m^\star$ with respect to m_b. This enhancement becomes more pronounced at higher carrier densities and/or in narrower quantum wells. Another important aspect is electron-electron interactions which, depending on the carrier density n_e, can either increase or decrease $m^\star$ [148, 149, 130, 131, 150, 151, 152, 153, 132]. Since cyclotron resonance is immune to interactions [154], one usually resorts to $m^\star$ measurements using Shubnikov-de Haas oscillations (SdHO) to pick up these effects [130, 131].

SdHO is a prime example of magneto-resistance oscillations which originate from Landau quantization when a 2DEG is subjected to a varying magnetic field B and low temperature T. These oscillations owe to the commensurability between the Fermi energy and the cyclotron energy $\hbar\omega_\mathrm{c} = \hbar eB/m^\star$. Since these energies are both inversely proportional to $m^\star$, $m^\star$ cancels out and the SdHO frequency $B_\mathrm{SdHO} = \pi\hbar n_e/e$ can only be used to obtain the carrier density n_e. The information about $m^\star$ is contained in the SdHO amplitude which is proportional to $(X_T/\sinh X_T)\exp(-\pi/\omega_\mathrm{c}\tau_\mathrm{q})$, where $X_T = 2\pi^2 k_B T/\hbar\omega_\mathrm{c} \propto m^\star$, k_B is the Boltzmann constant, and τ_q is the quantum lifetime. Therefore, the only way to extract $m^\star$ from the SdHO measurements is through the examination of the decay of the SdHO amplitude with increasing temperature. Such approach, however, is very time consuming as it requires magnetoresistance measurements at several different temperatures followed by a careful analysis. Furthermore,

the SdHO method suffers from a relatively low accuracy even if the data reduction procedure seems to work properly [155, 156, 130, 157]. Therefore, it is very desirable to employ other experimental probes, which are free from the above drawbacks, to obtain $m^\star$.

One such probe is based on a phenomenon known as microwave-induced resistance oscillations (MIRO) which emerge in irradiated 2DEGs [7, 8]. While MIRO also originate from Landau quantization, the role of the Fermi energy is now assumed by the energy of the incident photon $\hbar\omega$, where $\omega = 2\pi f$ is the microwave frequency. As a result, the effective mass $m^\star$ can be obtained directly from the MIRO frequency,

$$B_\omega = \frac{m^\star \omega}{e}\,, \tag{5.1}$$

which does not contain any other unknown parameters and can be measured precisely in a single B-sweep. In addition, it was recently shown [132] that $m^\star$ obtained using Eq. (5.1) differs from the value obtained from magneto-plasmon resonance [132], indicating sensitivity of the MIRO mass to interaction effects. Both of the above properties make MIRO an accurate, fast, and convenient option to investigate effective mass renormalization due to electron-electron interactions.

5.1.2 Probe effective mass employing MIRO

In this session we investigate the effect of the carrier density n_e on the effective mass obtained from the MIRO frequency in a high-mobility GaAs/AlGaAs quantum well equipped with *in situ* back gate. At higher electron density ($n_e \approx 3.16 \times 10^{11}$ cm^{-2}), the analysis of the MIRO frequency revealed $m^\star < m_b$, in accord with Ref. [132], which investigated MIRO in samples of similar density. When the carrier density was lowered down to $n_e \approx 1.26 \times 10^{11}$ cm^{-2}, our MIRO data clearly showed an increase of $m^\star$. While the increase of $m^\star$ is expected to occur with decreasing n_e, the detection of this increase previously required going to much lower densities [131], presumably, due to a considerably lower accuracy of the traditional SdHO approach.

Our 2DEG resides in a 30-nm GaAs/AlGaAs quantum well located about 200 nm below the sample surface. The structure is doped in a 2 nm GaAs quantum well at a setback of 63 nm on a top side. The *in situ* gate consists of an n^+ GaAs layer situated 850 nm below the bottom of the quantum well [158]. The density of the 2DEG at

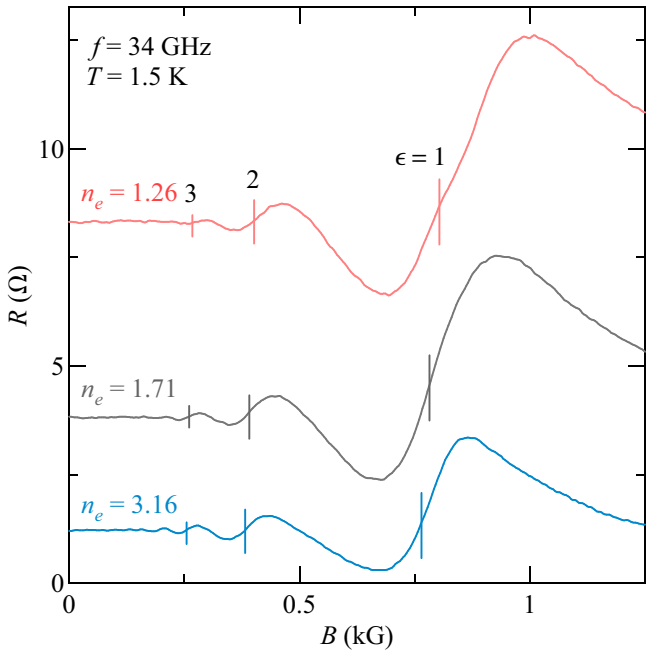

Figure 5.1: (Color online) Magnetoresistance $R(B)$ measured at density $n_e \approx 1.26$ (top trace), 1.71 (middle trace), and 3.16×10^{11} cm^{-2} (bottom trace) at $T = 1.5$ K under irradiation by microwaves of $f = 34$ GHz. Vertical line segments are drawn at $B = B_\omega/N$ for $N = 1, 2, 3$, as marked.

zero gate bias is $n_e \approx 1.64 \times 10^{11}$ cm^{-2} [158]. Ohmic contacts were fabricated at the corners and midsides of the lithographically-defined 1×1 mm^2 Van der Pauw mesa. The low-temperature electron mobility varied from $\mu \approx 0.4 \times 10^7$ to $\mu \approx 1.2 \times 10^7$ cm^2/Vs over the density range studied. Microwave radiation of $f = 34$ GHz, generated by a synthesized sweeper, was delivered to the sample immersed in liquid ^{3}He via a rectangular (WR-28) stainless steel waveguide. The resistance R was measured using a standard low-frequency (a few Hz) lock-in technique.

Before presenting our experimental results, we recall that the radiation-induced correction to resistance which gives rise to MIRO can be described by [64]

$$\delta R \propto -\lambda^2 \epsilon \sin 2\pi\epsilon \,, \tag{5.2}$$

where $\epsilon \equiv \omega/\omega_c \equiv B_\omega/B$ and $\lambda = \exp(-\epsilon/2f\tau_q)$ is the Dingle factor. We note that, for brevity, we limit theoretical expressions to the case of positive B, N, and ϵ. For negative values, one should change sign of $\delta_N^{\pm}$. The N-th order MIRO maximum (+), minimum

$(-)$, and the N-th zero-response node, defined by $\delta R = 0$, are given in Eq. 1.18 and Eq. 1.19.

While Eq. (1.18) is very simple, it should be used with caution. We address again that Eq. (1.20) is valid only in the regime of overlapping Landau levels, i.e., when the amplitude of oscillations in the density of states (given by $\lambda \ll 1$) due to Landau quantization is small. Also, it works best at low radiation intensities as high microwave power is known to reduce $|\delta_N^{\pm}|$ or even introduce additional oscillations [77, 78]. Finally, at sufficiently low values of $f\tau_{\rm q}$, the exponential dependence of the Dingle factor can be strong enough to cause a significant shift of the oscillation extrema towards lower ϵ [65, 66, 67, 159]. These considerations suggest that it is important to confirm that $|\delta_N^{\pm}| \approx 0.25$. While none of the above limitations apply to Eq. (1.19), direct determination of the node positions from the experimental data is not possible.

In Figure. 5.1 we present magnetoresistance $R(B)$ for three different densities, $n_e \approx 1.26$ (top trace), 1.71 (middle trace), and 3.16×10^{11} cm^{-2} (bottom trace), measured at $T = 1.5$ K under irradiation by microwaves of $f = 34$ GHz. It is evident that as the density is lowered, MIRO continuously shift to higher magnetic fields reflecting an increase of the effective mass. The shift can also be discerned by comparing vertical line segments drawn at $B_N = B_\omega/N$ for $N = 1, 2, 3$, computed using Eq. (5.1) and $m^\star$ values obtained as discussed below.

Since $\epsilon = B_\omega/B \propto m^\star/B$, $m^\star$ can be readily obtained from the slope of $\epsilon_N^{\pm}$ vs $1/B$ evaluated at the MIRO extrema. This approach is illustrated in Figure. 5.2 showing ϵ_N^+ ($\bullet$) and ϵ_N^- ($\circ$) as a function of $1/B$ at the MIRO maxima (cf. $2+, 3+, 4+$) and minima, respectively, obtained from R (solid line) measured at $n_e = 1.26 \times 10^{11}$ cm^{-2}, $T = 0.5$ K, and $f = 34$ GHz. One readily observes that the data points for both maxima and minima fall on the same straight line passing through the origin. This observation is important as it confirms that the positions of the MIRO maxima are accurately described by Eq. (1.18). The linear fit (solid line) generates the MIRO frequency $B_\omega = 0.804$ kG, from which one obtains $m^\star = 0.0662\, m_0$ using Eq. (5.1).

While $|\delta_N^{\pm}| \approx 0.25$ is a good approximation for $N = 2, 3, 4$, the extrema near the cyclotron resonance are pushed towards the nodes at $\epsilon = \pm 1$ and are characterized by a considerably smaller $|\delta_1^{\pm}|$. As a result, these extrema cannot be directly included in the analysis to obtain the mass. However, since $|\delta_1^+| \approx |\delta_1^-|$, one can use the average

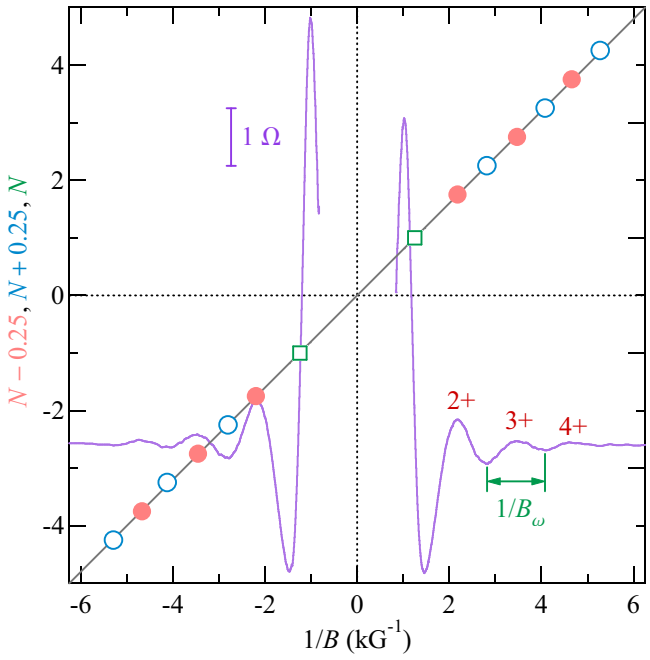

Figure 5.2: (Color online) $N - 0.25$ (●) and $N + 0.25$ (○) as a function of $1/B$ at the MIRO maxima (cf. $2+, 3+, 4+$) and minima, respectively, obtained from R (solid line) measured at $n_e = 1.26 \times 10^{11}$ cm^{-2}, $T = 0.5$ K, and $f = 34$ GHz. $N = \pm 1$ (□) vs $1/B = (1/B_1^+ + 1/B_1^-)/2$, see text. Linear fit to B_ω/B generates MIRO frequency $B_\omega = 0.804$ kG, from which one obtains $m^\star = 0.0662\, m_0$ using Eq. (5.1).

position of these extrema, i.e., $1/B_1 = (1/B_1^+ + 1/B_1^-)/2$, to obtain data points at the node between them, $\epsilon = N = \pm 1$. As shown in Figure. 5.2, these points (□) are in excellent agreement with the rest of the data supporting the viability of the above approach.

Having obtained B_ω, it is straightforward to compute ϵ which allows further validation of the data reduction procedure to obtain the effective mass. In Figure. 5.3 we present R as a function of $\epsilon = B_\omega/B$ computed using $m^\star = 0.0662, 0.0644$, and $0.0631\, m_0$ for $n_e \approx 1.26$ (top trace), 1.71 (middle trace), and 3.16×10^{11} cm^{-2} (bottom trace), respectively, measured at $T = 1.5$ K and $f = 34$ GHz. Vertical lines are drawn at $\epsilon = \pm(N - 1/4)$ for $N = 1, 2, 3, 4$. These lines pass through all MIRO maxima with $|N| \geq 2$ confirming that $|\delta_N^+| \approx 0.25$. The same conclusion can be drawn for the MIRO minima.

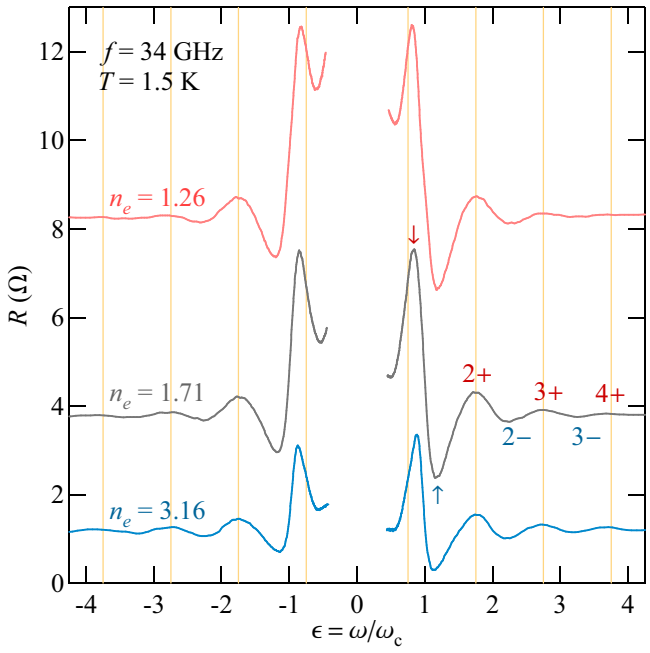

Figure 5.3: (Color online) R for $n_e \approx 1.26$ (top trace), 1.71 (middle trace), and 3.16×10^{11} cm^{-2} (bottom trace) measured at $T = 1.5$ K and $f = 34$ GHz as a function of $\epsilon = \omega/\omega_c$ computed using $\epsilon = B_\omega/B$ with $m^\star = 0.0662$, 0.0644, and $0.0631\,m_0$, respectively. MIRO maxima (minima) are marked by $N+$ ($N-$) for $N = 2, 3, 4$ and by $\downarrow$ ($\uparrow$) for $N = 1$. Vertical lines are drawn at $\epsilon = \pm(N - 1/4)$ for $N = 1, 2, 3, 4$.

After repeating the effective mass extraction for other densities, we summarize our findings in Figure. 5.4 showing $m^\star$, in units of a free electron mass m_0, as a function of n_e. We find that the effective mass increases from $m^\star \approx 0.0631$ to $0.0662\,m_0$, as the density is lowered from $n_e \approx 3.16$ to 1.26×10^{11} cm^{-2}. We note that, in contrast to electron-electron interactions, non-parabolicity increases $m^\star$ as the density is *raised*. In a HIGFET used in Ref. [131], this increase was estimated to be about 3 % within our density range. It is also evident that at lower n_e the effective mass is changing at a faster rate.

It is interesting to compare our findings with an earlier study which investigated the density dependence of $m^\star$ obtained from SdHO in heterojunction-insulated gate field effect transistor (HIGFET) [131]. The findings of Ref. [131] can be briefly summarized as follows. At low densities, between $n_e \approx 1 \times 10^{10}$ cm^{-2} and $n_e \approx 1 \times 10^{11}$ cm^{-2}, $m^\star$ showed a decrease from $m^\star \approx 0.085 - 0.1$ to $m^\star \approx 0.06 - 0.065$. However, further

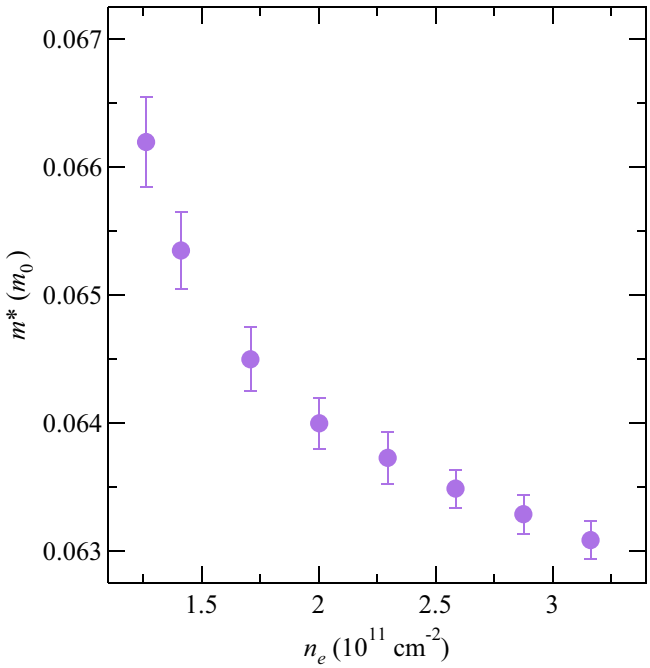

Figure 5.4: (Color online) Effective mass $m^\star$, in units of a free electron mass m_0, as a function of the carrier density n_e.

increase of density up to $n_e = 4\times10^{11}$ cm^{-2} showed either little variation of the effective mass within the experimental uncertainty [131] or a slight increase [130] which could have originated from non-parabolicity. This is in contrast to our data which clearly show a noticeable decrease of $m^\star$ with increasing n_e within this density range.

One possible reason for the above discrepancy is a much higher accuracy of our approach as compared to the SdHO analysis. Indeed, the uncertainty of the mass obtained in Ref. [131] is comparable to the mass change detected in our experiment. However, it is also known that quantum confinement of a 2DEG under study sensitively affects mass renormalization due to electron-electron interactions [150, 151, 152]. More specifically, the finite thickness of the 2DEG softens the Coulomb interaction potential, resulting in a reduced mass value compared to the ideal 2D case [150, 151, 152]. Furthermore, the dependence of the quantum confinement on the gate voltage is not universal but depends on the heterostructure design. In contrast to HIGFET, the electron distribution in our quantum well becomes wider and more symmetric when a positive bias is applied

to the back gate. As a result, one should exercise caution when attempting quantitative comparison of our findings with that of Ref. [131] or with existing calculations [150, 151, 152], both of which investigated a HIGFET realization of a 2DEG. We note that, another recent study [160] has reported $m^\star = 0.0575m_e$ and $m^\star \approx 0.067m_e$ in a HIGFET and a modulation-doped single-interface heterostructure, respectively. Apart from the delta-doping, both heterostructures were identical and both samples were gated to the same density $n_e = 6.1 \times 10^{10}$ cm^{-2}. While the samples were characterized by very different values of transport and quantum lifetimes, which might have affected accuracy of the SdHO method, Ref. [160] did not comment on the origin of this discrepancy.

In summary, we investigated the effect of carrier density n_e on the effective mass obtained from the MIRO frequency in a high-mobility modulation-doped GaAs/AlGaAs quantum well equipped with *in situ* back gate over the density range from $\approx 1.2 \times 10^{11}$ cm^{-2} to $n_e \approx 3.2 \times 10^{11}$ cm^{-2}. At the highest n_e, the analysis of the MIRO frequency revealed $m^\star \approx 0.063\, m_0$, considerably lower than the band mass value $m_b = 0.067\, m_0$, in qualitative agreement with Ref. [132]. We note that, quantitatively, our study revealed the effective mass which is noticeably (about 7 %) higher than obtained in Ref. [132]. While the exact reason for such discrepancy is unknown, it might be due to the differences in heterostructure designs, as suggested in a recent study [160]. With decreasing density, the effective mass was found to increase exceeding $m^\star = 0.066\, m_0$ at the lowest density. While the low-density increase of $m^\star$ has been previously established by SdHO measurements [131], it was detected only at much lower densities. Taken together, our findings lend strong support that MIRO, like SdHO [130, 131], are sensitive to electron-electron interactions but offer a much more convenient and accurate means to obtain $m^\star$. In addition, the MIRO approach can be directly applied to the effective mass renormalization studies in other systems, such as recently emerged high-quality Ge/SiGe and MgZnO/ZnO heterostructures. Finally, our results are in general agreement with recent measurements of the MIRO mass in a series of individual samples covering a wider density range [133].

5.2 Unexpected density dependence on microwave-induced resistance oscillations

5.2.1 Motivation

MIRO dependent on ϵ, $\delta\rho_\omega \propto -\epsilon\lambda^2 \sin 2\pi\epsilon$, has been verified in many experiments. In addition, it was established that while MIROs at high microwave power significantly deviate from Eq. (1.20), they can still be well described within the same theoretical framework after generalization to an arbitrary radiation intensity [76, 77, 78]. At the same time, experiments also revealed situations when existing theory is inadequate, e.g., in describing the measured dependencies on radiation polarization [79, 80] and on temperature [81]. Limitations of the theory were also identified in the regime of separated Landau levels [82] and in the radiation-induced modification of Shubnikov−de Haas oscillations [83].

One important parameter, whose role has remained largely unexplored, is the carrier density n_e. While it has been recently demonstrated that n_e affects ϵ, presumably through interaction-induced renormalization of the effective mass $m^\star$ [133, 134], it should also modify other quantities, e.g., $\mathcal{P}$ and η, entering Eq. (1.20). Since the density dependencies of $\mathcal{P}$ and η are both known theoretically, MIRO measurements as a function of n_e should provide an important test to existing microscopic description of microwave photoresistance.

5.2.2 MIRO amplitude

The density of the 2DEG was varied from $n_e \approx 1.41$ to 2.87×10^{11} cm^{-2}. Over this density range, the low-temperature electron mobility increased from $\mu \approx 0.37$ to $\mu \approx 1.1 \times 10^7$ cm^{2}V^{-1}s^{-1}, roughly following $\mu \propto n_e^\alpha$, with $\alpha \approx 1.5$ [135]. We note that, the obtained value of α is in agreement with recent theoretical calculations [135] considering GaAs quantum wells similar to the one employed in our study.

In Figure. 5.5(a) we present R/R_0 vs $1/\epsilon$ for three different densities, $n_e \approx 1.41$ (bottom trace), 2.15 (middle trace), and 2.87×10^{11} cm^{-2} (top trace), measured at $T = 1.5$ K under irradiation by microwaves of $f = 34$ GHz. The data show that MIROs become significantly stronger with increasing density. We next extract the oscillatory

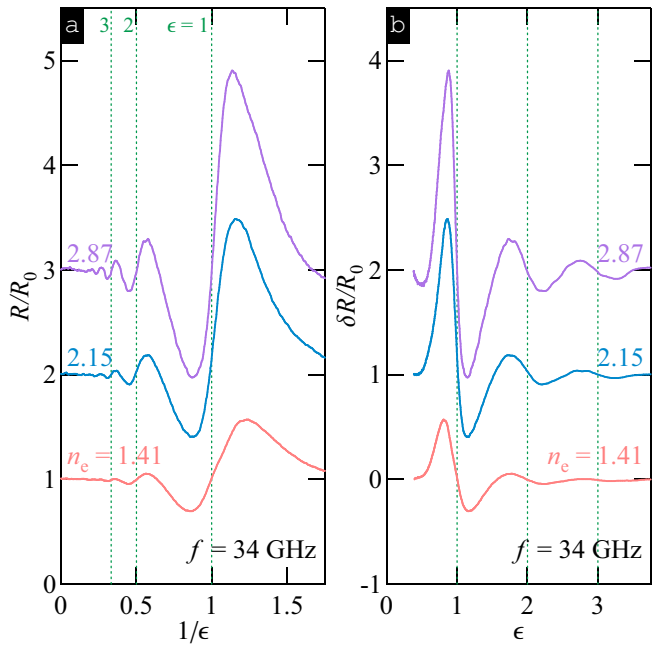

Figure 5.5: (Color online) (a) R/R_0 vs. $1/\epsilon$ at density $n_e \approx 1.41$ (bottom trace), 2.15 (middle trace), and 2.87×10^{11} cm^{-2} (top trace) at $T = 1.5$ K under irradiation by microwaves of $f = 34$ GHz. We note that, ϵ was computed using $m^\star = 0.0652, 0.0638$, and $0.0631 m_0$ for $n_e = 1.41, 2.15$ and 2.87×10^{11} cm^{-2}, respectively [134]. Vertical lines are drawn at $\epsilon = 1, 2, 3$, as marked. (b) $\delta R/R_0$ vs ϵ under the same conditions as in panel (a). The traces are vertically offset for clarity by 1.

correction $\delta R/R_0$ and present the result in Figure. 5.5(b) as a function of ϵ. All three data sets reveal an expected periodicity with ϵ, in agreement with Eq. (1.20).

According to Eq. (1.20), the MIRO amplitude is proportional to the effective microwave power, which is shown in Eq. 1.22. The density dependence of β_ω has been recently verified in time-resolved measurements of the cyclotron resonance [161]. Within the density range studied in our experiment, $\tau \gg \tau_{\rm em}$ and $\beta_\omega \approx (\omega\tau_{\rm em})^{-1} \propto n_e$. However, β_ω remains much smaller than unity and, as a result, $\mathcal{P}$ increases with n_e for all ϵ except in close proximity to $\epsilon = 1$. We will see, however, that the anticipated increase in $\mathcal{P}$ is rather small and contributes little to the growth of MIRO shown in Figure. 5.5.

The growth of MIRO with n_e observed in Figure. 5.5 can, in principle, stem from $\tau_{\rm q}$ (entering λ) or η. Both of these parameters are readily available from the Dingle analysis. Following Eq. (1.20), we introduce a reduced MIRO amplitude $\mathcal{A} =$

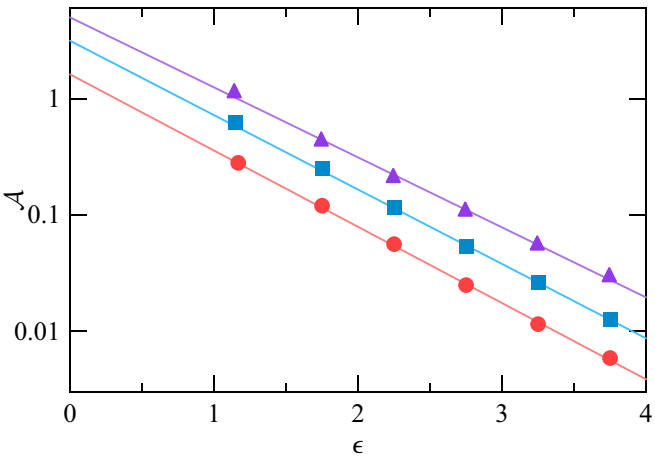

Figure 5.6: (Color online) $\mathcal{A} = |\delta R|_{\max}/2\pi\epsilon\mathcal{P}R_0$ vs ϵ for $n_e \approx 1.41$ (circles), 2.15 (squares), and 2.87×10^{11} cm^{-2} (triangles) measured at $T = 1.5$ and $f = 34$ GHz. We note that, $\mathcal{P}$ was calculated using Eq. (1.22) with $\mathcal{E}_{\rm ac} = 1$ V/cm and $m^\star = 0.067m_0$ entering ϵ and $\tau_{\rm em}$. Fits to the data with $\mathcal{A}_0 \exp(-\epsilon/f\tau_{\rm q})$ (solid lines) yield $\tau_{\rm q} \approx 19.5$, 20.0, and 21.2 ps respectively.

$|\delta R|_{\max}/2\pi\epsilon\mathcal{P}R_0$, where $|\delta R|_{\max}$ is the MIRO amplitude, and present it in Figure. 5.6 as a function of ϵ for $n_e = 1.41$ (circles), 2.15 (squares), and 2.87×10^{11} cm^{-2} (triangles). Fits to the data with $\mathcal{A}_0 \exp(-\epsilon/f\tau_{\rm q})$ (solid lines) yield $\tau_{\rm q} \approx 19.5$, 20.0, and 21.2 ps, respectively, indicating a slight increase of $\tau_{\rm q}$ with n_e. In contrast, the intercept of the Dingle plots, $\mathcal{A}_0$, grows substantially with n_e. As we show below, theory predicts that under our experimental conditions $\mathcal{A}_0$ can only decrease with n_e.

After repeating the Dingle analysis for other n_e, we present the density dependence of $\tau_{\rm q}$ (circles) in Figure. 5.7. A slight increase of $\tau_{\rm q}$ with n_e appears to contradict a recent study [162], which has found a saturation of $\tau_{\rm q}$ at $n_e \approx 2 \times 10^{11}$ cm^{-2} and a monotonic decrease at higher n_e. This discrepancy can be alleviated by recalling that Shubnikov−de Haas oscillations employed in Ref. [162] yield only impurity contributions to the quantum lifetime $\tau_{\rm q,0}$ [163, 164]. The quantum lifetime obtained from MIROs, on the other hand, is reduced by electron-electron scattering, as shown in Eq. 1.23. Under the conditions of our experiment the electron-electron scattering rate is given by [84, 85, 73]

$$\frac{\hbar}{\tau_{\rm ee}} = \frac{\pi k_B^2 T^2}{4E_F} \ln \frac{2\hbar v_F/a_B}{\pi k_B T}\,, \tag{5.3}$$

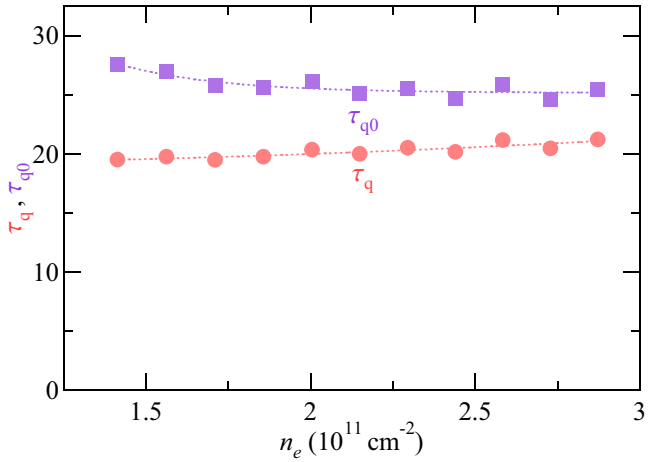

Figure 5.7: (Color online) τ_q (circles), obtained from the fits (cf. Figure. 5.6), and $\tau_{q,0}$ (squares), calculated using Eqs. Eq. (1.23)and Eq. (1.24), vs n_e. The dotted lines are guides to the eye.

where E_F is the Fermi energy and $a_B \approx 11$ nm is the Bohr radius in GaAs. Using Eqs. (1.23) and (5.3) we compute $\tau_{q,0}$ and present the results (squares) in Figure. 5.7. The results show that the impurity-limited quantum lifetime decreases slightly with n_e, in general agreement with Ref. [162]. We note, however, that in our experiment most of this decrease takes place at densities below $\approx 2 \times 10^{11}$ cm^{-2}.

As already mentioned, Figure. 5.6 also reveals a significant increase of the intercept of the Dingle fits, given by $\mathcal{A}_0$, with increasing n_e. Since $\mathcal{A}_0 \propto \eta$, this increase reflects the increase in η, provided that the density dependence of $\mathcal{P}$ is accurately described by Eq. (1.22). We note that, microwave power is not exactly known and $\mathcal{A}_0$ differs from η by a numerical factor. To quantify this increase we introduce a parameter $\kappa = \mathcal{A}_0(n_e)/\mathcal{A}_0(n_l)$, where $n_l = 1.41 \times 10^{11}$ cm^{-2} is the lowest density studied. As shown in Figure. 5.8, κ (circles) increases by a factor of about 3 over the investigated density range. This finding is unexpected since, as we show next, one should anticipate a *decrease* of η with increasing n_e.

The dimensionless scattering rate η is given in Eq. (1.21) that $\eta = \frac{\tau}{2\tau_\star} + \frac{2\tau_{in}}{\tau}$. The first (second) term represents displacement [70, 165, 71] (inelastic [73, 75]) contribution. Here, $\tau_{in} \approx 0.82\tau_{ee}$ [73] and $\tau/2\tau_\star$ can vary between $\tau/2\tau_\star = 6(\tau/\tau_{q,0} + 3)^{-1}$ (smooth disorder limit) and $\tau/2\tau_\star = 3/2$ (sharp disorder limit) according to the mixed-disorder

model [129, 75]. We recall that, the rate of scattering on angle θ can be expressed in terms of angular harmonics, $\tau_n = \tau_{-n}$, as $\tau_\theta^{-1} = \sum_{-\infty}^{+\infty} \tau_n^{-1} e^{in\theta}$. In this notation, $\tau_{\mathrm{q},0}^{-1} \equiv \left\langle \tau_\theta^{-1} \right\rangle_\theta = \tau_0^{-1}, \tau^{-1} \equiv \left\langle \tau_\theta^{-1}(1-\cos\theta) \right\rangle_\theta = \tau_0^{-1} - \tau_1^{-1}$, and $\tau_\star^{-1} \equiv 2\left\langle \tau_\theta^{-1}(1-\cos\theta)^2 \right\rangle_\theta = 3\tau_0^{-1} - 4\tau_1^{-1} + \tau_2^{-1}$ ($\langle\cdots\rangle_\theta$ denotes averaging over θ). In the mixed disorder model [129], $\tau_n^{-1} = \tau_{\mathrm{sh}}^{-1}\delta_{n,0} + \tau_{\mathrm{sm}}^{-1}(1+\chi n^2)^{-1}$, where τ_{sh}^{-1} and τ_{sm}^{-1} represent, respectively, scattering rates for background impurities and remote ionized donors [located at a distance d from the interface, $\chi = (2k_F d)^{-2}$]. As a result, the relative change in η (or $\mathcal{A}_0$) with n_e is expected to fall between κ_{sm} and κ_{sh}, given by $\eta(n_e)/\eta(n_l)$ evaluated in the smooth and the sharp disorder limit, respectively. On a qualitative level, the decrease of $\tau/2\tau_\star$ with n_e can be expected whenever $\tau_{\mathrm{q}}/\tau \ll 1$, i.e., when small angle scattering dominates, which is the case for all modern high-mobility GaAs quantum wells. This decrease should occur because $\tau_\star^{-1}$ is less sensitive to small-angle scattering than τ^{-1} and because the characteristic scattering angle decreases with density.

As shown in Figure. 5.8, both κ_{sh} (squares) and κ_{sm} (triangles) monotonically decrease with n_e. The decrease in κ_{sh} with n_e occurs solely due to the weakening of the inelastic contribution, given by the second term in Eq. (1.21). This weakening, in turn, owes to a superlinear increase in the momentum relaxation time τ, which wins over the slightly sublinear increase in τ_{in} [see Eq. (1.24)]. In the smooth disorder limit, characterized by κ_{sm}, the decrease becomes larger due to the growing ratio of $\tau/\tau_{\mathrm{q},0}$ which enters the denominator of the displacement contribution [first term in Eq. (1.21)]. We thus conclude that regardless of the exact disorder characteristics, theoretical predictions are in contrast with the experimentally obtained κ (circles) which shows a significant *increase* over the density range studied. We note that, An alternative theoretical proposal [166] considering MIROs in terms of classical memory effects for the case of small-angle scattering predicts $\eta \propto \tau n_e^{1/2}$. We note, however, that the inelastic mechanism was not considered in Ref. [166] and that their choice of the disorder potential predicts $\tau_{\mathrm{q}}, \tau \propto n_e^{-1/2}$ leading to density-independent η. Our findings were confirmed by measurements using $f = 39.5$ GHz in another sample which is not shown here.

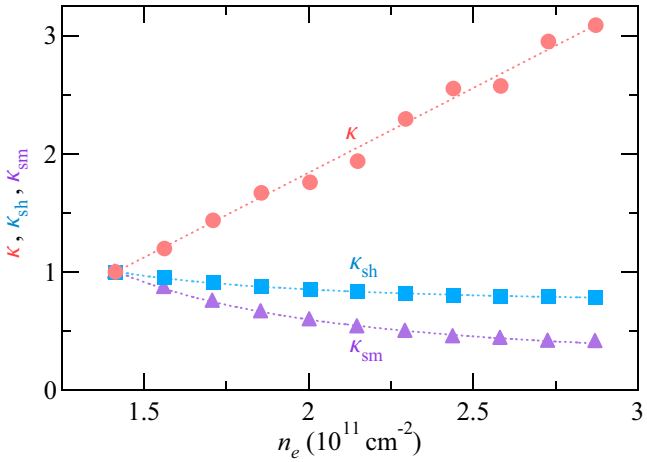

Figure 5.8: (Color online) κ (circles), obtained from the fits (cf. Figure. 5.6), $\kappa_{\rm sh}$ (squares), and $\kappa_{\rm sm}$ (triangles), calculated using Eq. (1.21) in the sharp and smooth disorder limit, respectively, vs n_e. The dotted lines are guides to the eye.

5.2.3 Fundamental oscillation extrema

We next examine the effect of density on the positions of the MIRO extrema near the cyclotron resonance. As noted from the data in Figure. 5.5(b), these extrema move closer towards $\epsilon = 1$ with increasing density. To examine this behavior quantitatively, we introduce a parameter $\varphi = (\epsilon^- - \epsilon^+)/2$, where ϵ^- (ϵ^+) is the position of the fundamental minimum (maximum). We then present obtained φ (circles) in Figure. 5.9(a) as a function of n_e and observe that it monotonically *decreases* with n_e. Similar to $\tau_{\rm q,0}$, the decrease is more pronounced at lower densities. Theory, however, predicts just the opposite behavior; as illustrated in Figure. 5.9(a), the calculated values of $\varphi_{\rm sh}$ (squares) and $\varphi_{\rm sm}$ (triangles), representing sharp and smooth disorder limits, respectively, both increase with n_e. The expected growth of $\varphi_{\rm sh} \approx \varphi_{\rm sm}$ with n_e occurs, for the most part, due to the increase in β_ω, dominated by $\tau_{\rm em}^{-1} \propto n_e$, which controls the sharpness of $\mathcal{P}$ near $\epsilon = 1$. Indeed, as shown in Figure. 5.9(b), $\mathcal{P}(\epsilon)$ is considerably sharper at $n_e = 1.41 \times 10^{11}$ cm^{-2} (solid line) than at $n_e = 2.87 \times 10^{11}$ cm^{-2} (dotted line).

It is known that the phase reduction can occur with increasing $\mathcal{P}$ due to contributions from multiphoton processes [77, 78]. This scenario, however, can be ruled out since $\mathcal{P}$, in fact, decreases with n_e near $\epsilon = 1$ within the investigated density range. As shown in Figure. 5.9(c), $\mathcal{P}$ at the fundamental MIRO extrema (solid and open circles) exhibits

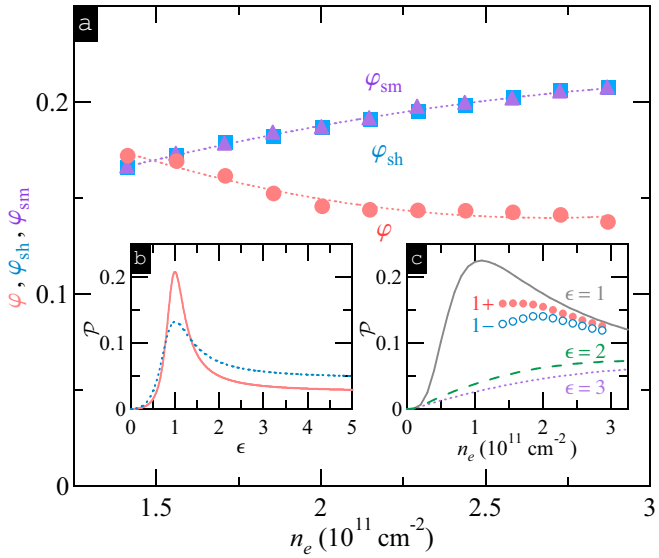

Figure 5.9: (Color online) (a) φ (circles), $\varphi_{\rm sh}$ (squares), and $\varphi_{\rm sm}$ (triangles) vs n_e. The dotted lines are guides to the eye. (b) $\mathcal{P}$ vs ϵ for $n_e = 1.41 \times 10^{11}$ cm^{-2} (solid line) and $n_e = 2.87 \times 10^{11}$ cm^{-2} (dotted line). (c) $\mathcal{P}$ vs n_e for $\epsilon = 1$ (solid line), $\epsilon = 2$ (dashed line), and $\epsilon = 3$ (dotted line). Also shown is $\mathcal{P}$ vs n_e at the first MIRO maximum (1+, solid circles) and minimum (1−, open circles).

a slight overall decrease within the studied density range, similar to $\mathcal{P}$ at $\epsilon = 1$ (solid line). At higher MIRO orders, $\mathcal{P}$ monotonically increases, as illustrated by dashed and dotted lines computed for $\epsilon = 2$ and $\epsilon = 3$, respectively. This increase in $\mathcal{P}$ occurs because $\mathcal{P}_0 \propto n_e$ while β_ω remains relatively small within the studied density range.

5.3 Discussions

One somewhat uncertain parameter is $\epsilon_{\rm eff}$ which affects β_ω entering $\mathcal{P}$ given by Eq. (1.22). Indeed, the expression we have used is generally valid only when the overall sample thickness greatly exceeds the radiation wavelength, a condition which is not satisfied for the microwave frequency used in our experiment. According to Ref. [64], a better approximation would be using $\epsilon_{\rm eff} = 1$ which would increase the value of β_ω by approximately a factor of 2. However, any increase in β_ω would only weaken (or even reverse) the density dependence of $\mathcal{P}$ and further increase the disagreement between theory and experiment, both in η and φ.

Finally, we note that by applying the gate voltage we are not only changing the carrier density but also modifying the confinement potential. Numerical simulations show that the 2DEG is pulled away from the top interface towards the center of the quantum well and becomes wider with increasing density. Whether or not such a change of the confinement plays any significant role in the observed enhancement of the MIRO amplitude is unclear at this point and is left for future studies. To investigate this possibility, it would be interesting to perform measurements in different structures, such as heterojunction-insulated gate field-effect transistors, in which confinement becomes stronger with increasing carrier density.

Chapter 6

Effect of illumination on quantum lifetime in GaAs quantum wells

This chapter is adapted from X. Fu, A. Riedl, M. Borisov, M. A. Zudov, J. D. Watson, G. Gardner, M. J. Manfra, K. W. Baldwin, L. N. Pfeiffer, and K. W. West, Effect of illumination on quantum lifetime in GaAs quantum wells, *Phys. Rev. B* **98**, 195403 (2018), by permission of the American Physical Society under the American Physical Society reuse and permission license.

6.1 Introduction: effect of illumination on sample "quality"

Even though low-temperature illumination of a 2DEG in GaAs quantum wells is known to improve the quality of high-field magnetotransport [167, 142, 143], systematic investigations of this effect remain limited. One study [142] has investigated the effect of illumination on a 2DEG residing in a 30 nm-wide GaAs/$Al_{0.34}Ga_{0.66}As$ quantum well with Si δ-doping layers placed directly in $Al_{0.34}Ga_{0.66}As$ barriers on both sides at setback distances of 100 nm (above the well) and 120 nm (below the well). The initial effect of illumination is a considerable increase of both the density n_e and the mobility μ of the 2DEG [168] which, predictably, resulted in better developed fractional quantum Hall (FQH) states. However, additional, higher-intensity illumination left n_e and

μ essentially unchanged, while the transport features, e.g., the fragile FQH states in the $N = 1$ Landau level, were further improved. This improvement was attributed to the enhanced screening of ionized impurities by an increased number of polarized neutral shallow donors. We note that, light-induced conversion of negatively-charged DX centers to neutral shallow donors has been demonstrated much earlier in Ref. [169] which systematically investigated the effect of illumination on time-dependent density and mobility in modulation-doped GaAs/Al_xGa_{1-x}As single heterojunctions. This work also showed that illumination can increase mobility without affecting the carrier density.

Another study [143] investigated the effect of illumination in a 2DEG hosted by a 30 nm-wide GaAs/$Al_{0.24}Ga_{0.76}$As quantum well utilizing a "modern" doping scheme. This heterostructure was also remotely doped on both sides, but Si atoms were placed inside very narrow GaAs "doping" wells sandwiched between thin AlAs layers [170, 11, 171, 172, 10, 173, 135]. Such doping scheme avoids formation of deep donor states, all Si atoms are ionized, but a significant fraction of donated electrons populate the X-band in surrounding AlAs layers. Interestingly, illumination of such structure can also lead to improvement of high-field transport characteristics even though it does not appreciably change n_e and μ. For example, Ref. [143] has shown that illumination can significantly enhance the measured energy gap of the FQH state at filling factor $\nu = 5/2$ and better development of other fragile quantum Hall states. The enhancement of transport quality was linked to improved homogeneity of the 2DEG achieved after illumination.

In this chapter we (i) examine the effect of illumination on the quality of the *low-field* magnetotransport under microwave irradiation and (ii) quantitatively assess the effect of illumination on total (quantum) lifetime τ_q, which is a measure of electron-remote impurity scattering. To measure τ_q we employ microwave-induced resistance oscillations (MIRO) [7, 8] which, in contrast to SdHO [162], are believed to be largely immune to macroscopic density fluctuations. We find that after illumination MIRO become more pronounced while extending to lower magnetic fields. The Dingle analysis reveals that the observed improvement is a result of significant enhancement of quantum lifetime which increases by a factor of about two. This enhancement presents strong evidence that illumination results in reduced scattering from remote impurities, presumably due to light-induced redistribution of charge improving the screening capability of the doping

layers. Whether or not the increase of τ_q also contributes to the improvement of high-field transport [167, 142, 143] remains an open question [172, 162].

6.2 Probe the role of illumination with MIRO

While we have investigated several samples with similar outcomes, here we present the results from two samples which exhibited almost no change in mobility due to illumination. The 2DEG in sample A (B) resides in a GaAs quantum well of width 30 nm (24.9 nm) surrounded by $Al_xGa_{1-x}As$ barriers with $x = 0.24$ ($x = 0.28$). Sample A (B) utilized Si doping in narrow GaAs doping wells surrounded by thin AlAs layers and positioned at a setback distance of 75 nm (80 nm) on both sides of the GaAs well hosting the 2DEG. Both samples were 4×4 mm squares with eight indium contacts fabricated at the corners and the midsides. When cooled in the dark, sample A (B) had the density $n_e \approx 2.57 \times 10^{11}$ cm^{-2} ($n_e \approx 3.33 \times 10^{11}$ cm^{-2}). Low-temperature mobility was estimated to be $\mu \approx 1.5 \times 10^7$ cm^{2}V^{-1}s^{-1} in sample A and $\mu \approx 1.6 \times 10^7$ cm^{2}V^{-1}s^{-1} in sample B. Measurements were performed in Faraday configuration; microwave radiation was delivered to the sample immersed in liquid ^{3}He inside a superconducting solenoid via a rectangular (WR-28) stainless steel waveguide with the magnetic field was applied perpendicular to the 2DEG. The longitudinal resistance R in sample A (B) was recorded using a standard low-frequency (a few Hz) four-terminal lock-in technique under continuous irradiation by microwaves of $f = 34$ GHz ($f = 64$ GHz) at a constant coolant temperature $T \approx 0.3$ K ($T \approx 1.8$ K).

Both sample A and sample B were illuminated by visible light (either green or white light-emitting diode) via the microwave waveguide at zero magnetic field for 10 minutes. For sample A, we followed a procedure outlined in Ref. [143]; illumination at base temperature ($T \approx 0.3$ K in our case) following up by an annealing step at $T \approx 2.5$ K for 15 minutes. For sample B, we used "conventional" illumination temperature of $T \approx 5$ K after which the sample was cooled down in the dark. After illumination procedure, the density of sample A (B) increased only by $\approx 4 \times 10^9$ cm^{-2} ($\approx 9 \times 10^9$ cm^{-2}) while the mobilities remained essentially unchanged. However, as we show next, both illumination protocols yielded substantial improvement of the quality of low-field magnetotransport, manifested by more pronounced MIRO, which we link to the

enhancement of the quantum lifetime.

Before presenting our experimental results, we recall that the oscillatory microwave photoresistance δR, i.e., the change of resistance caused by microwave radiation, can be written as $\frac{\delta R(\epsilon)}{R_0} \propto -2\pi\epsilon\lambda^2\mathcal{P}\sin 2\pi\epsilon$ as shown in Eq. (1.20). Again, R_0 is the resistance at $B = 0$, $\epsilon = 2\pi f/\omega_c$, $\omega_c = eB/m^\star$ is the cyclotron frequency, $m^\star \approx 0.06m_0$ is the electron effective mass [132, 133, 134], $\lambda = \exp(-\pi/\omega_c\tau_q)$ is the Dingle factor, and $\mathcal{P}(\epsilon)$ is the effective microwave power which, for linearly polarized microwaves, is given in Eq. (1.22).

The effect of low-temperature illumination on MIRO in sample A is illustrated in Figure. 6.1(a) which shows the resistance R normalized to its zero-field value R_0 measured before (dotted line) and after (solid line) illumination under microwave irradiation of frequency $f = 34$ GHz at temperature $T \approx 0.3$ K. Vertical lines are drawn at integer ϵ, as marked. The data clearly reveal that after illumination MIRO become more pronounced and extend to higher orders. Similar measurements in sample B, though employing different illumination procedure, yielded qualitatively identical results, as illustrated in Figure. 6.1(b) showing the data at $f = 68$ GHz and $T \approx 1.8$ K.

The results in Figure. 6.1 reveal that the enhancement of MIRO after illumination is significantly more pronounced at higher ϵ, signaling an increase in quantum lifetime. To quantify this increase, we performed Dingle analysis of MIRO. Following Eq. (1.20), we introduce a reduced MIRO amplitude $\mathcal{A} = |\delta R|_{\max}\mathcal{P}_0/2\pi\epsilon\mathcal{P}R_0$, where $|\delta R|_{\max}$ is the measured MIRO amplitude. The results for sample A and sample B are presented in Figure. 6.2(a) and (b), respectively, which show $\mathcal{A}$ as a function of ϵ extracted from the data acquired before (●) and after (■) illumination. Fitting the data with $\mathcal{A} = \mathcal{A}_0\exp(-\epsilon/f\tau_q)$ (solid lines) reveals that illumination enhances τ_q from 23 ps to 44 ps in sample A and from 16 ps to 32 ps in sample B.

Next, we take the electron-electron scattering into accounts. The relationship between quantum lifetime yielding from MIRO and electron-electron scattering is given in Eq. (1.23). And electron-electron contribution τ_{ee}^{-1} is given in Eq. (1.24). It is clear that subtracting the electron-electron contribution will only increase the change in impurity-limited quantum lifetime caused by illumination. Because measurements on sample A were performed at low temperature ($T \approx 0.3$ K), electron-electron scattering rate is much smaller than $\tau_q^{-1} \approx \tau_{q,0}^{-1}$. In sample B, however, Eq. (1.24) yields $\tau_{ee} \approx 80$ ps and

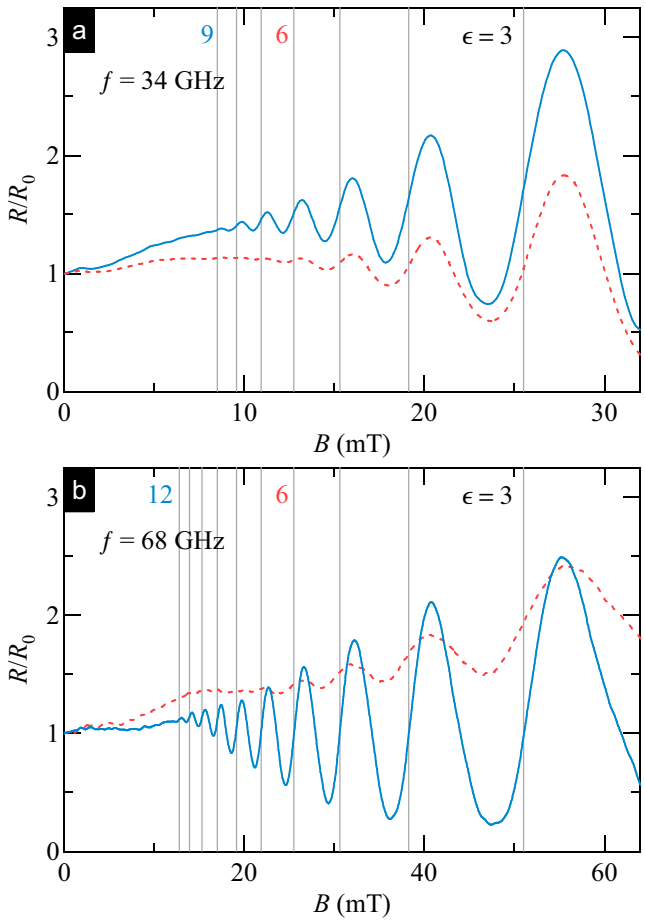

Figure 6.1: (Color online) Resistance in units of the zero-field resistance R/R_0 as a function of B measured before (dotted line) and after (solid line) illumination in (a) sample A at $T \approx 0.3$ K and $f = 34$ GHz and (b) sample B at $T \approx 1.8$ K and $f = 68$ GHz. Vertical lines are drawn at integer ϵ, as marked.

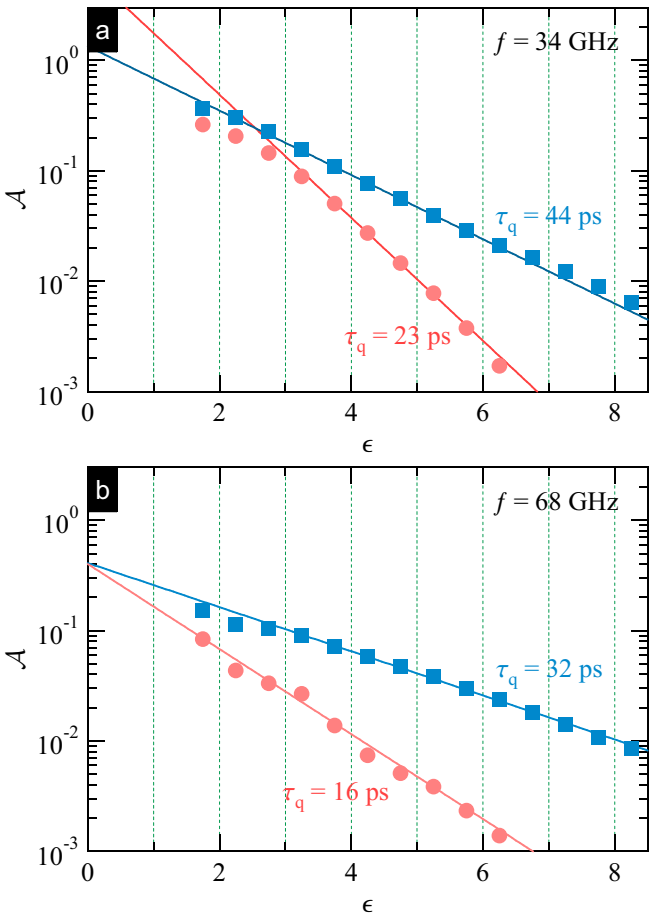

Figure 6.2: (Color online) Reduced MIRO amplitude $\mathcal{A} = |\delta R|_{\max}(\mathcal{P}_0/\mathcal{P})/2\pi\epsilon R_0$ as a function of ϵ for (a) sample A and (b) sample B before (●) and after (■) illumination. Fitting the data with $\mathcal{A} = \mathcal{A}_0 \exp(-\epsilon/f\tau_q)$ (solid lines) reveals that illumination enhances τ_q from 23 ps to 44 ps in sample A and from 16 ps to 32 ps in sample B.

using Eq. (1.23) we can estimate that $\tau_{q,0}$ increases from $\tau_{q,0} \approx 20$ ps to $\tau_{q,0} \approx 53$ ps upon illumination.

While the observed increase of quantum lifetime after illumination in both samples is quite significant, the momentum relaxation time τ remained virtually unchanged. This observation allows us to establish the source of disorder which is affected by illumination. Since the quantum scattering rate, in general, is much more sensitive to remote impurities than the transport scattering rate, we can conclude that illumination primarily affects scattering from remote impurities rather than from those in the vicinity of the GaAs quantum well. Insensitivity of τ to illumination then suggests that contribution of the remote impurities to the momentum relaxation rate is negligible even before the illumination, i.e., that τ is limited by scattering from unintentional background impurities within the GaAs quantum well and in the AlGaAs barriers [135, 174]. The quantum scattering rate, on the other hand, can still contain a sizable or even dominant contribution from the remote impurities, e.g. Si ions in the doping layers, before the sample has been illuminated.

6.3 Discussions

Recent theoretical examination [135, 174] of the doping layers has shown that excess electrons which occupy the X-bands of the AlAs mini-wells form compact dipoles with donors of their choice (to minimize their energy) which reside in GaAs mini-wells. These X-electrons can effectively screen the random potential from the remaining un-paired ionized Si atoms and the screening effectiveness grows rapidly with their number. Because of this fast growth, the doping layer which has fewer X-electrons will contribute much more strongly to scattering than the other one. In typical samples, such as ours, this would be the top doping layer which donate significant number of electrons to compensate surface states. If the illumination can increase the number of X-electrons in the top doping layer, e.g., by returning electrons from the surface, one can expect a significant reduction of the quantum scattering rate. Assuming that after illumination the number of X-electrons in the top doping layer becomes similar to that in the bottom doping layer, theoretical estimates [135, 174] show that the remote impurity-limited quantum lifetime should be several times higher than observed in our experiment. Our

findings thus suggest that the quantum scattering rate after illumination is limited by scattering off background impurities residing in the main GaAs quantum well and in surrounding AlGaAs barriers.

While we clearly established that illumination significantly reduces quantum scattering rate, whether the observed reduction is the sole cause for the concurrent improvement in high-field transport characteristics [167, 142, 143] can be debated [172, 162]. Indeed, as mentioned in Ref. [143], low-temperature illumination can also lead to improved density homogeneity of the 2DEG under study which must lead to improved development of FQH states, e.g., the increase of the excitation gap at $\nu = 5/2$. MIRO, on the other hand, are nearly immune to macroscopic density fluctuations and therefore their enhancement can be linked directly to the increase of the quantum lifetime. Indeed, the enhancement of MIRO accompanied by an increase in τ_{q} has been observed even when samples became less homogeneous after illumination.

References

[1] K. von Klitzing, G. Dorda, and M. Pepper. New method for high-accuracy determination of the fine-structure constant based on quantized Hall resistance. *Phys. Rev. Lett.*, 45:494, 1980.

[2] D. C. Tsui, H. L. Stormer, and A. C. Gossard. Two-dimensional magnetotransport in the extreme quantum limit. *Phys. Rev. Lett.*, 48:1559, 1982.

[3] A. A. Koulakov, M. M. Fogler, and B. I. Shklovskii. Charge density wave in two-dimensional electron liquid in weak magnetic field. *Phys. Rev. Lett.*, 76:499, 1996.

[4] M. M. Fogler, A. A. Koulakov, and B. I. Shklovskii. Ground state of a two-dimensional electron liquid in a weak magnetic field. *Phys. Rev. B*, 54:1853, 1996.

[5] M. P. Lilly, K. B. Cooper, J. P. Eisenstein, L. N. Pfeiffer, and K. W. West. Evidence for an anisotropic state of two-dimensional electrons in high Landau levels. *Phys. Rev. Lett.*, 82:394, 1999.

[6] R. R. Du, D. C. Tsui, H. L. Stormer, L. N. Pfeiffer, K. W. Baldwin, and K. W. West. Strongly anisotropic transport in higher two-dimensional Landau levels. *Solid State Commun.*, 109:389, 1999.

[7] M. A. Zudov, R. R. Du, J. A. Simmons, and J. L. Reno. Shubnikov–de haas-like oscillations in millimeterwave photoconductivity in a high-mobility two-dimensional electron gas. *Phys. Rev. B*, 64:201311(R), 2001.

[8] P. D. Ye, L. W. Engel, D. C. Tsui, J. A. Simmons, J. R. Wendt, G. A. Vawter, and J. L. Reno. Giant microwave photoresistance of two-dimensional electron gas. *Appl. Phys. Lett.*, 79:2193, 2001.

[9] Y. J. Chung, K. A. Villegas Rosales, K. W. Baldwin, P. T. Madathil, K. W. West, M. Shayegan, and L. N. Pfeiffer. Ultra-high-quality two-dimensional electron systems. *Nat. Mat.*, 20(5):632, 2021.

[10] Michael J. Manfra. Molecular beam epitaxy of ultra-high-quality AlGaAs/GaAs heterostructures: Enabling physics in low-dimensional electronic systems. *Annu. Rev. Condens. Matter Phys.*, 5(1):347, 2014.

[11] K.-J. Friedland, R. Hey, H. Kostial, R. Klann, and K. Ploog. New concept for the reduction of impurity scattering in remotely doped GaAs quantum wells. *Phys. Rev. Lett.*, 77:4616, 1996.

[12] D. J. Chadi and K. J. Chang. Energetics of DX-center formation in GaAs and $Al_xGa_{1-x}As$ alloys. *Phys. Rev. B*, 39:10063, 1989.

[13] S. Das Sarma and F. Stern. Single-particle relaxation time versus scattering time in an impure electron gas. *Phys. Rev. B*, 32:8442, 1985.

[14] J. P. Eisenstein, R. L. Willett, H. L. Stormer, L. N. Pfeiffer, and K. W. West. Activation energies for the even-denominator fractional quantum Hall effect. *Surf. Sci.*, 229(1):31, 1990.

[15] W. Pan, J.-S. Xia, V. Shvarts, D. E. Adams, H. L. Stormer, D. C. Tsui, L. N. Pfeiffer, K. W. Baldwin, and K. W. West. Exact quantization of the even-denominator fractional quantum Hall state at $\nu = 5/2$ Landau level filling factor. *Phys. Rev. Lett.*, 83:3530, 1999.

[16] Qi Qian. *Quantum Transport in the AlGaAs/GaAs Two Dimensional Electron System at Half-Fillings*. PhD thesis, Purdue University, 2018.

[17] S. F. Nelson, K. Ismail, J. J. Nocera, F. F. Fang, E. E. Mendez, J. O. Chu, and B. S. Meyerson. Observation of the fractional quantum Hall effect in Si/SiGe heterostructures. *Appl. Phys. Lett.*, 61(1):64, 1992.

[18] T. M. Kott, B. Hu, S. H. Brown, and B. E. Kane. Valley-degenerate two-dimensional electrons in the lowest Landau level. *Phys. Rev. B*, 89:041107, 2014.

[19] E. P. De Poortere, Y. P. Shkolnikov, E. Tutuc, S. J. Papadakis, M. Shayegan, E. Palm, and T. Murphy. Enhanced electron mobility and high order fractional quantum Hall states in AlAs quantum wells. *Appl. Phys. Lett.*, 80(9):1583, 2002.

[20] M. J. Manfra, N. G. Weimann, J. W. P. Hsu, L. N. Pfeiffer, K. W. West, S. Syed, H. L. Stormer, W. Pan, D. V. Lang, S. N. G. Chu, G. Kowach, A. M. Sergent, J. Caissie, K. M. Molvar, L. J. Mahoney, and R. J. Molnar. High mobility AlGaN/GaN heterostructures grown by plasma-assisted molecular beam epitaxy on semi-insulating GaN templates prepared by hydride vapor phase epitaxy. *J. Appl. Phys.*, 92(1):338, 2002.

[21] X. Du, I. Skachko, F. Duerr, A. Luican, and E. Y. Andrei. Fractional quantum Hall effect and insulating phase of Dirac electrons in graphene. *Nature*, 462(7270):192, 2009.

[22] K. I. Bolotin, F. Ghahari, M. D. Shulman, Horst L. Stormer, and P. Kim. Observation of the fractional quantum Hall effect in graphene. *Nature*, 462(7270):196, 2009.

[23] B. A. Piot, J. Kunc, M. Potemski, D. K. Maude, C. Betthausen, A. Vogl, D. Weiss, G. Karczewski, and T. Wojtowicz. Fractional quantum Hall effect in CdTe. *Phys. Rev. B*, 82:081307, 2010.

[24] A. Tsukazaki, S. Akasaka, K. Nakahara, Y. Ohno, H. Ohno, D. Maryenko, A. Ohtomo, and M. Kawasaki. Observation of the fractional quantum Hall effect in an oxide. *Nat. Mat.*, 9(11):889, 2010.

[25] Q. Shi, M. A. Zudov, C. Morrison, and M. Myronov. Spinless composite fermions in an ultrahigh-quality strained Ge quantum well. *Phys. Rev. B*, 91:241303(R), 2015.

[26] M. K. Ma, M. S. Hossain, K. A. Villegas Rosales, H. Deng, T. Tschirky, W. Wegscheider, and M. Shayegan. Observation of fractional quantum Hall effect in an InAs quantum well. *Phys. Rev. B*, 96:241301, 2017.

[27] R. B. Laughlin. Anomalous quantum Hall effect: An incompressible quantum fluid with fractionally charged excitations. *Phys. Rev. Lett.*, 50:1395, 1983.

[28] J. K. Jain. Composite-fermion approach for the fractional quantum Hall effect. *Phys. Rev. Lett.*, 63:199, 1989.

[29] X. Liu, Z. Hao, K. Watanabe, T. Taniguchi, B. I. Halperin, and P. Kim. Interlayer fractional quantum Hall effect in a coupled graphene double layer. *Nat. Phys.*, 15(9):893, 2019.

[30] J. I. A. Li, Q. Shi, Y. Zeng, K. Watanabe, T. Taniguchi, J. Hone, and C. R. Dean. Pairing states of composite fermions in double-layer graphene. *Nat. Phys.*, 15(9):898, 2019.

[31] C. W. J. Beenakker. Edge channels for the fractional quantum Hall effect. *Phys. Rev. Lett.*, 64:216, 1990.

[32] A. H. MacDonald. Edge states in the fractional-quantum-Hall-effect regime. *Phys. Rev. Lett.*, 64:220, 1990.

[33] G. Sambandamurthy, R. M. Lewis, H. Zhu, Y. P. Chen, L. W. Engel, D. C. Tsui, L. N. Pfeiffer, and K. W. West. Observation of pinning mode of stripe phases of 2D systems in high Landau levels. *Phys. Rev. Lett.*, 100:256801, 2008.

[34] M. E. Msall and W. Dietsche. Acoustic measurements of the stripe and the bubble quantum Hall phase. *New J. Phys.*, 17(4):043042, 2015.

[35] B. Friess, Y. Peng, B. Rosenow, F. von Oppen, V. Umansky, K. von Klitzing, and J. H. Smet. Negative permittivity in bubble and stripe phases. *Nat. Phys*, 13:1124, 2017.

[36] J. Zhu, W. Pan, H. L. Stormer, L. N. Pfeiffer, and K. W. West. Density-induced interchange of anisotropy axes at half-filled high Landau levels. *Phys. Rev. Lett.*, 88:116803, 2002.

[37] J. Pollanen, K. B. Cooper, S. Brandsen, J. P. Eisenstein, L. N. Pfeiffer, and K. W. West. Heterostructure symmetry and the orientation of the quantum Hall nematic phases. *Phys. Rev. B*, 92:115410, 2015.

[38] X. Fu, Q. Shi, M. A. Zudov, Y. J. Chung, K. W. Baldwin, L. N. Pfeiffer, and K. W. West. Quantum Hall stripes in high-density GaAs/AlGaAs quantum wells. *Phys. Rev. B*, 98:205418, 2018.

[39] S. P. Koduvayur, Y. Lyanda-Geller, S. Khlebnikov, G. Csáthy, M. J. Manfra, L. N. Pfeiffer, K. W. West, and L. P. Rokhinson. Effect of strain on stripe phases in the quantum Hall regime. *Phys. Rev. Lett.*, 106:016804, 2011.

[40] I. Sodemann and A. H. MacDonald. Theory of native orientational pinning in quantum Hall nematics. *arXiv:1307.5489*, 2013.

[41] M. P. Lilly, K. B. Cooper, J. P. Eisenstein, L. N. Pfeiffer, and K. W. West. Anisotropic states of two-dimensional electron systems in high Landau levels: Effect of an in-plane magnetic field. *Phys. Rev. Lett.*, 83:824, 1999.

[42] W. Pan, R. R. Du, H. L. Stormer, D. C. Tsui, L. N. Pfeiffer, K. W. Baldwin, and K. W. West. Strongly anisotropic electronic transport at Landau level filling factor under a tilted magnetic field. *Phys. Rev. Lett.*, 83:820, 1999.

[43] T. Jungwirth, A. H. MacDonald, L. Smrčka, and S. M. Girvin. Field-tilt anisotropy energy in quantum Hall stripe states. *Phys. Rev. B*, 60:15574, 1999.

[44] T. D. Stanescu, I. Martin, and P. Phillips. Finite-temperature density instability at high Landau level occupancy. *Phys. Rev. Lett.*, 84:1288, 2000.

[45] H. Zhu, G. Sambandamurthy, L. W. Engel, D. C. Tsui, L. N. Pfeiffer, and K. W. West. Pinning mode resonances of 2D electron stripe phases: Effect of an in-plane magnetic field. *Phys. Rev. Lett.*, 102:136804, 2009.

[46] Q. Shi, M. A. Zudov, Q. Qian, J. D. Watson, and M. J. Manfra. Effect of density on quantum Hall stripe orientation in tilted magnetic fields. *Phys. Rev. B*, 95:161303, 2017.

[47] Q. Shi, M. A. Zudov, J. D. Watson, G. C. Gardner, and M. J. Manfra. Reorientation of quantum Hall stripes within a partially filled Landau level. *Phys. Rev. B*, 93:121404, 2016.

[48] M. A. Mueed, M. S. Hossain, L. N. Pfeiffer, K. W. West, K. W. Baldwin, and M. Shayegan. Reorientation of the stripe phase of 2D electrons by a minute density modulation. *Phys. Rev. Lett.*, 117:076803, 2016.

[49] Y. Liu, D. Kamburov, M. Shayegan, L. N. Pfeiffer, K. W. West, and K. W. Baldwin. Spin and charge distribution symmetry dependence of stripe phases in two-dimensional electron systems confined to wide quantum wells. *Phys. Rev. B*, 87:075314, 2013.

[50] J. Gores, G. Gamez, J. H. Smet, L. Pfeiffer, K. West, A. Yacoby, V. Umansky, and K. von Klitzing. Current-induced anisotropy and reordering of the electron liquid-crystal phases in a two-dimensional electron system. *Phys. Rev. Lett.*, 99:246402, 2007.

[51] E. Fradkin and S A. Kivelson. Liquid-crystal phases of quantum Hall systems. *Phys. Rev. B*, 59:8065, 1999.

[52] A. H. MacDonald and Matthew P. A. Fisher. Quantum theory of quantum Hall smectics. *Phys. Rev. B*, 61:5724–5733, 2000.

[53] Q. Qian, J. Nakamura, S. Fallahi, G. C. Gardner, and M. J. Manfra. Possible nematic to smectic phase transition in a two-dimensional electron gas at half-filling. *Nat. Commun.*, 8(1):1536, 2017.

[54] M. Sammon, X. Fu, Y. Huang, M. A. Zudov, B. I. Shklovskii, G. C. Gardner, J. D. Watson, M. J. Manfra, K. W. Baldwin, L. N. Pfeiffer, and K. W. West. Resistivity anisotropy of quantum Hall stripe phases. *Phys. Rev. B*, 100:241303, 2019.

[55] F. D. M. Haldane, E. H. Rezayi, and K. Yang. Spontaneous breakdown of translational symmetry in quantum Hall systems: Crystalline order in high Landau levels. *Phys. Rev. Lett.*, 85:5396, 2000.

[56] N. Shibata and D. Yoshioka. Ground-state phase diagram of 2D electrons in a high Landau level: A density-matrix renormalization group study. *Phys. Rev. Lett.*, 86:5755, 2001.

[57] K. B. Cooper, M. P. Lilly, J. P. Eisenstein, L. N. Pfeiffer, and K. W. West. Insulating phases of two-dimensional electrons in high Landau levels: Observation of sharp thresholds to conduction. *Phys. Rev. B*, 60:11285, 1999.

[58] X. Wang, H. Fu, L. Du, X. Liu, P. Wang, L. N. Pfeiffer, K. W. West, R. Du, and X. Lin. Depinning transition of bubble phases in a high Landau level. *Phys. Rev. B*, 91:115301, 2015.

[59] R. M. Lewis, P. D. Ye, L. W. Engel, D. C. Tsui, L. N. Pfeiffer, and K. W. West. Microwave resonance of the bubble phases in 1/4 and 3/4 filled high Landau levels. *Phys. Rev. Lett.*, 89:136804, 2002.

[60] R. M. Lewis, Y. Chen, L. W. Engel, D. C. Tsui, P. D. Ye, L. N. Pfeiffer, and K. W. West. Evidence of a first-order phase transition between wigner-crystal and bubble phases of 2D electrons in higher Landau levels. *Phys. Rev. Lett.*, 93:176808, 2004.

[61] N. Deng, J. D. Watson, L. P. Rokhinson, M. J. Manfra, and G. A. Csáthy. Contrasting energy scales of reentrant integer quantum Hall states. *Phys. Rev. B*, 86:201301, 2012.

[62] K. A. Villegas Rosales, S. K. Singh, H. Deng, Y. J. Chung, L. N. Pfeiffer, K. W. West, K. W. Baldwin, and M. Shayegan. Melting phase diagram of bubble phases in high Landau levels. *Phys. Rev. B*, 104:L121110, 2021.

[63] M. A. Zudov, R. R. Du, J. A. Simmons, and J. L. Reno. Microwave photoresistance measurements of magneto-excitations near a 2D fermi surface. *arXiv:cond-mat/9711149v1*, 1997.

[64] I. A. Dmitriev, A. D. Mirlin, D. G. Polyakov, and M. A. Zudov. Nonequilibrium phenomena in high Landau levels. *Rev. Mod. Phys.*, 84:1709, 2012.

[65] M. A. Zudov, O. A. Mironov, Q. A. Ebner, P. D. Martin, Q. Shi, and D. R. Leadley. Observation of microwave-induced resistance oscillations in a high-mobility two-dimensional hole gas in a strained Ge/SiGe quantum well. *Phys. Rev. B*, 89:125401, 2014.

[66] Q. Shi, Q. A. Ebner, and M. A. Zudov. Hall field-induced resistance oscillations in a p-type Ge/SiGe quantum well. *Phys. Rev. B*, 90:161301(R), 2014.

[67] D. F. Kärcher, A. V. Shchepetilnikov, Yu. A. Nefyodov, J. Falson, I. A. Dmitriev, Y. Kozuka, D. Maryenko, A. Tsukazaki, S. I. Dorozhkin, I. V. Kukushkin, M. Kawasaki, and J. H. Smet. Observation of microwave induced resistance and photovoltage oscillations in MgZnO/ZnO heterostructures. *Phys. Rev. B*, 93:041410, 2016.

[68] E. Mönch, D. A. Bandurin, I. A. Dmitriev, I. Y. Phinney, I. Yahniuk, T. Taniguchi, K. Watanabe, P. Jarillo-Herrero, and S. D. Ganichev. Observation of terahertz-induced magnetooscillations in graphene. *Nano Lett.*, 20(8):5943, 2020.

[69] V. I. Ryzhii. Photoconductivity characteristics in thin films subjected to crossed electric and magnetic fields. *Sov. Phys. Solid State*, 11:2078, 1970.

[70] A. C. Durst, S. Sachdev, N. Read, and S. M. Girvin. Radiation-induced magnetoresistance oscillations in a 2D electron gas. *Phys. Rev. Lett.*, 91:086803, 2003.

[71] M. G. Vavilov and I. L. Aleiner. Magnetotransport in a two-dimensional electron gas at large filling factors. *Phys. Rev. B*, 69:035303, 2004.

[72] I. A. Dmitriev, A. D. Mirlin, and D. G. Polyakov. Cyclotron-resonance harmonics in the ac response of a 2D electron gas with smooth disorder. *Phys. Rev. Lett.*, 91:226802, 2003.

[73] I. A. Dmitriev, M. G. Vavilov, I. L. Aleiner, A. D. Mirlin, and D. G. Polyakov. Theory of microwave-induced oscillations in the magnetoconductivity of a two-dimensional electron gas. *Phys. Rev. B*, 71:115316, 2005.

[74] S. I. Dorozhkin. Giant magnetoresistance oscillations caused by cyclotron resonance harmonics. *JETP Lett.*, 77:577, 2003.

[75] I. A. Dmitriev, M. Khodas, A. D. Mirlin, D. G. Polyakov, and M. G. Vavilov. Mechanisms of the microwave photoconductivity in two-dimensional electron systems with mixed disorder. *Phys. Rev. B*, 80:165327, 2009.

[76] M. Khodas, H. S. Chiang, A. T. Hatke, M. A. Zudov, M. G. Vavilov, L. N. Pfeiffer, and K. W. West. Nonlinear magnetoresistance oscillations in intensely irradiated two-dimensional electron systems induced by multiphoton processes. *Phys. Rev. Lett.*, 104:206801, 2010.

[77] A. T. Hatke, M. Khodas, M. A. Zudov, L. N. Pfeiffer, and K. W. West. Multiphoton microwave photoresistance in a high-mobility 2D electron gas. *Phys. Rev. B*, 84:241302(R), 2011.

[78] Q. Shi, M. A. Zudov, I. A. Dmitriev, K. W. Baldwin, L. N. Pfeiffer, and K. W. West. Fine structure of high-power microwave-induced resistance oscillations. *Phys. Rev. B*, 95:041403(R), 2017.

[79] J. H. Smet, B. Gorshunov, C. Jiang, L. Pfeiffer, K. West, V. Umansky, M. Dressel, R. Meisels, F. Kuchar, and K. von Klitzing. Circular-polarization-dependent study of the microwave photoconductivity in a two-dimensional electron system. *Phys. Rev. Lett.*, 95:116804, 2005.

[80] T. Herrmann, I. A. Dmitriev, D. A. Kozlov, M. Schneider, B. Jentzsch, Z. D. Kvon, P. Olbrich, V. V. Bel'kov, A. Bayer, D. Schuh, D. Bougeard, T. Kuczmik, M. Oltscher, D. Weiss, and S. D. Ganichev. Analog of microwave-induced resistance oscillations induced in GaAs heterostructures by terahertz radiation. *Phys. Rev. B*, 94:081301, 2016.

[81] Q. Shi, S. A. Studenikin, M. A. Zudov, K. W. Baldwin, L. N. Pfeiffer, and K. W. West. Microwave photoresistance in an ultra-high-quality GaAs quantum well. *Phys. Rev. B*, 93:121305, 2016.

[82] A. T. Hatke, M. A. Zudov, L. N. Pfeiffer, and K. W. West. Microwave photoresistance in a two-dimensional electron gas with separated Landau levels. *Phys. Rev. B*, 84:241304(R), 2011.

[83] Q. Shi, P. D. Martin, A. T. Hatke, M. A. Zudov, J. D. Watson, G. C. Gardner, M. J. Manfra, L. N. Pfeiffer, and K. W. West. Shubnikov - de Haas oscillations in a two-dimensional electron gas under subterahertz radiation. *Phys. Rev. B*, 92:081405(R), 2015.

[84] A. V. Chaplik. Energy spectrum and electron scattering processes in inversion layers. *Sov. Phys. JETP*, 33:997, 1971.

[85] G. F. Giuliani and J. J. Quinn. Lifetime of a quasiparticle in a two-dimensional electron gas. *Phys. Rev. B*, 26:4421, 1982.

[86] V. Ryzhii and R. Suris. Nonlinear effects in microwave photoconductivity of two-dimensional electron systems. *J. Phys.: Condens. Matter*, 15:6855, 2003.

[87] V. Ryzhii, A. Chaplik, and R. Suris. Absolute negative conductivity and zero-resistance states in two-dimensional electron systems: A plausible scenario. *JETP Lett.*, 80:363, 2004.

[88] A. T. Hatke, M. A. Zudov, L. N. Pfeiffer, and K. W. West. Temperature dependence of microwave photoresistance in 2D electron systems. *Phys. Rev. Lett.*, 102:066804, 2009.

[89] C. L. Yang, J. Zhang, R. R. Du, J. A. Simmons, and J. L. Reno. Zener tunneling between Landau orbits in a high-mobility two-dimensional electron gas. *Phys. Rev. Lett.*, 89:076801, 2002.

[90] E. Wigner. On the interaction of electrons in metals. *Phys. Rev.*, 46:1002, 1934.

[91] Y. E. Lozovik and V. I. Yudson. Crystallization of a two-dimensional electron gas in a magnetic field. *Sov. JETPL*, 22:11, 1975.

[92] D. Yoshioka and H. Fukuyama. Charge density wave state of two-dimensional electrons in strong magnetic fields. *J. Phys. Soc. Japan*, 47(2):394, 1979.

[93] H. Fukuyama, P. M. Platzman, and P. W. Anderson. Two-dimensional electron gas in a strong magnetic field. *Phys. Rev. B*, 19:5211–5217, 1979.

[94] E. Y. Andrei, G. Deville, D. C. Glattli, F. I. B. Williams, E. Paris, and B. Etienne. Observation of a magnetically induced wigner solid. *Phys. Rev. Lett.*, 60:2765–2768, 1988.

[95] R. L. Willett, H. L. Stormer, D. C. Tsui, L. N. Pfeiffer, K. W. West, and K. W. Baldwin. Termination of the series of fractional quantum Hall states at small filling factors. *Phys. Rev. B*, 38:7881, 1988.

[96] V. J. Goldman, M. Shayegan, and D. C. Tsui. Evidence for the fractional quantum Hall state at $\nu = \frac{1}{7}$. *Phys. Rev. Lett.*, 61:881, 1988.

[97] W. Li, D. R. Luhman, D. C. Tsui, L. N. Pfeiffer, and K. W. West. Observation of reentrant phases induced by short-range disorder in the lowest Landau level of $Al_xGa_{1-x}As/Al_{0.32}Ga_{0.68}As$ heterostructures. *Phys. Rev. Lett.*, 105:076803, 2010.

[98] R. Moessner and J. T. Chalker. Exact results for interacting electrons in high Landau levels. *Phys. Rev. B*, 54:5006, 1996.

[99] J. P. Eisenstein, K. B. Cooper, L. N. Pfeiffer, and K. W. West. Insulating and fractional quantum Hall states in the first excited Landau level. *Phys. Rev. Lett.*, 88:076801, 2002.

[100] S. Chen, R. Ribeiro-Palau, K. Yang, K. Watanabe, T. Taniguchi, J. Hone, M. O. Goerbig, and C. R. Dean. Competing fractional quantum Hall and electron solid phases in graphene. *Phys. Rev. Lett.*, 122:026802, 2019.

[101] J. S. Xia, W. Pan, C. L. Vicente, E. D. Adams, N. S. Sullivan, H. L. Stormer, D. C. Tsui, L. N. Pfeiffer, K. W. Baldwin, and K. W. West. Electron correlation in the second Landau level: A competition between many nearly degenerate quantum phases. *Phys. Rev. Lett.*, 93:176809, 2004.

[102] G. A. Csáthy, J. S. Xia, C. L. Vicente, E. D. Adams, N. S. Sullivan, H. L. Stormer, D. C. Tsui, L. N. Pfeiffer, and K. W. West. Tilt-induced localization and delocalization in the second Landau level. *Phys. Rev. Lett.*, 94:146801, 2005.

[103] N. Deng, A. Kumar, M. J. Manfra, L. N. Pfeiffer, K. W. West, and G. A. Csáthy. Collective nature of the reentrant integer quantum Hall states in the second Landau level. *Phys. Rev. Lett.*, 108:086803, 2012.

[104] S. Baer, C. Rössler, S. Hennel, H. C. Overweg, T. Ihn, K. Ensslin, C. Reichl, and W. Wegscheider. Nonequilibrium transport in density-modulated phases of the second Landau level. *Phys. Rev. B*, 91:195414, 2015.

[105] A. V. Rossokhaty, Y. Baum, J. A. Folk, J. D. Watson, G. C. Gardner, and M. J. Manfra. Electron-hole asymmetric chiral breakdown of reentrant quantum Hall states. *Phys. Rev. Lett.*, 117:166805, 2016.

[106] V. Shingla, E. Kleinbaum, A. Kumar, L. N. Pfeiffer, K. W. West, and G. A. Csáthy. Finite-temperature behavior in the second Landau level of the two-dimensional electron gas. *Phys. Rev. B*, 97:241105, 2018.

[107] K. Bennaceur, C. Lupien, B. Reulet, G. Gervais, L. N. Pfeiffer, and K. W. West. Competing charge density waves probed by nonlinear transport and noise in the second and third Landau levels. *Phys. Rev. Lett.*, 120:136801, 2018.

[108] B. Friess, V. Umansky, K. von Klitzing, and J. H. Smet. Current flow in the bubble and stripe phases. *Phys. Rev. Lett.*, 120:137603, 2018.

[109] M. O. Goerbig, P. Lederer, and C. Morais Smith. Microscopic theory of the reentrant integer quantum Hall effect in the first and second excited Landau levels. *Phys. Rev. B*, 68:241302, 2003.

[110] M. O. Goerbig, P. Lederer, and C. Morais Smith. Competition between quantum-liquid and electron-solid phases in intermediate Landau levels. *Phys. Rev. B*, 69:115327, 2004.

[111] D. Yoshioka and N. Shibata. Dmrg study of the ground state at higher Landau levels—stripes, bubbles and the wigner crystal. *Physica E Low Dimens*, 12(1):43, 2002.

[112] G. C. Gardner, J. D. Watson, S. Mondal, N. Deng, G. A. Csáthy, and M. J. Manfra. Growth and electrical characterization of $Al_{0.24}Ga_{0.76}As/Al_xGa_{1-x}As/Al_{0.24}Ga_{0.76}As$ modulation-doped quantum wells with extremely low x. *Appl. Phys. Lett.*, 102(25):252103, 2013.

[113] M. M. Fogler and A. A. Koulakov. Laughlin liquid to charge-density-wave transition at high Landau levels. *Phys. Rev. B*, 55:9326, 1997.

[114] D. V. Fil. Piezoelectric mechanism for the orientation of stripe structures in two-dimensional electron systems. *Low Temp. Phys.*, 26(8):581, 2000.

[115] Q. Shi, M. A. Zudov, J. D. Watson, G. C. Gardner, and M. J. Manfra. Evidence for a new symmetry breaking mechanism reorienting quantum Hall nematics. *Phys. Rev. B*, 93:121411, 2016.

[116] J. Falson, D. Tabrea, D. Zhang, I. Sodemann, Y. Kozuka, A. Tsukazaki, M. Kawasaki, K. v. Klitzing, and J. H. Smet. A cascade of phase transitions in an orbitally mixed half-filled Landau level. *Sci. Adv.*, 4:8742, 2018.

[117] M. S. Hossain, M. A. Mueed, Meng K. Ma, Y. J. Chung, L. N. Pfeiffer, K. W. West, K. W. Baldwin, and M. Shayegan. Anomalous coupling between magnetic and nematic orders in quantum Hall systems. *Phys. Rev. B*, 98:081109, 2018.

[118] X. Fu, Q. Shi, M. A. Zudov, G. C. Gardner, J. D. Watson, and M. J. Manfra. Two- and three-electron bubbles in $Al_xGa_{1-x}As/Al_{0.24}Ga_{0.76}As$ quantum wells. *Phys. Rev. B*, 99:161402, 2019.

[119] D. Ro, N. Deng, J. D. Watson, M. J. Manfra, L. N. Pfeiffer, K. W. West, and G. A. Csáthy. Electron bubbles and the structure of the orbital wave function. *Phys. Rev. B*, 99:201111, 2019.

[120] Y. Huang, M. Sammon, M. A. Zudov, and B. I. Shklovskii. Isotropically conducting (hidden) quantum Hall stripe phases in a two-dimensional electron gas. *Phys. Rev. B*, 101:161302, 2020.

[121] F. von Oppen, B. I. Halperin, and A. Stern. Conductivity tensor of striped quantum Hall phases. *Phys. Rev. Lett.*, 84:2937, 2000.

[122] T. Ando and Y. Uemura. Theory of quantum transport in a two-dimensional electron system under magnetic fields. i. characteristics of level broadening and transport under strong fields. *J. Phys. Soc. Jpn.*, 36:959, 1974.

[123] P. T. Coleridge, P. Zawadzki, and A. S. Sachrajda. Peak values of resistivity in high-mobility quantum-Hall-effect samples. *Phys. Rev. B*, 49:10798, 1994.

[124] Qianhui Shi. *Magnetotransport in quantum Hall systems at high Landau levels.* PhD thesis, University of Minnesota, 2017.

[125] M. E. Raikh and T. V. Shahbazyan. High Landau levels in a smooth random potential for two-dimensional electrons. *Phys. Rev. B*, 47:1522, 1993.

[126] A. D. Mirlin, E. Altshuler, and P. Wölfle. Quasiclassical approach to impurity effect on magnetooscillations in 2D metals. *Ann. Phys.*, 5:281, 1996.

[127] M. A. Zudov, I. A. Dmitriev, B. Friess, Q. Shi, V. Umansky, K. von Klitzing, and J. Smet. Hall field-induced resistance oscillations in a tunable-density GaAs quantum well. *Phys. Rev. B*, 96:121301, 2017.

[128] W. Zhang, H.-S. Chiang, M. A. Zudov, L. N. Pfeiffer, and K. W. West. Magnetotransport in a two-dimensional electron system in dc electric fields. *Phys. Rev. B*, 75:041304(R), 2007.

[129] M. G. Vavilov, I. L. Aleiner, and L. I. Glazman. Nonlinear resistivity of a two-dimensional electron gas in a magnetic field. *Phys. Rev. B*, 76:115331, 2007.

[130] P. T. Coleridge, M. Hayne, P. Zawadzki, and A. S. Sachrajda. Effective masses in high-mobility 2D electron gas structures. *Surf. Sci.*, 361:560, 1996.

[131] Y.-W. Tan, J. Zhu, H. L. Stormer, L. N. Pfeiffer, K. W. Baldwin, and K. W. West. Measurements of the density-dependent many-body electron mass in two dimensional GaAs/AlGaAs heterostructures. *Phys. Rev. Lett.*, 94:016405, 2005.

[132] A. T. Hatke, M. A. Zudov, J. D. Watson, M. J. Manfra, L. N. Pfeiffer, and K. W. West. Evidence for effective mass reduction in GaAs/AlGaAs quantum wells. *Phys. Rev. B*, 87:161307(R), 2013.

[133] A. V. Shchepetilnikov, D. D. Frolov, Yu. A. Nefyodov, I. V. Kukushkin, and S. Schmult. Renormalization of the effective mass deduced from the period of microwave-induced resistance oscillations in GaAs/AlGaAs heterostructures. *Phys. Rev. B*, 95:161305, 2017.

[134] X. Fu, Q. A. Ebner, Q. Shi, M. A. Zudov, Q. Qian, J. D. Watson, and M. J. Manfra. Microwave-induced resistance oscillations in a back-gated GaAs quantum well. *Phys. Rev. B*, 95:235415, 2017.

[135] M. Sammon, M. A. Zudov, and B. I. Shklovskii. Mobility and quantum mobility of modern GaAs/AlGaAs heterostructures. *Phys. Rev. Materials*, 2:064604, 2018.

[136] X. Fu, Q. Shi, M. A. Zudov, G. C. Gardner, J. D. Watson, M. J. Manfra, K. W. Baldwin, L. N. Pfeiffer, and K. W. West. Anomalous nematic states in high half-filled Landau levels. *Phys. Rev. Lett.*, 124:067601, 2020.

[137] R. Willett, J. P. Eisenstein, H. L. Störmer, D. C. Tsui, A. C. Gossard, and J. H. English. Observation of an even-denominator quantum number in the fractional quantum Hall effect. *Phys. Rev. Lett.*, 59:1776, 1987.

[138] Y. Kim, A. C. Balram, T. Taniguchi, K. Watanabe, J. K. Jain, and J. H. Smet. Even denominator fractional quantum Hall states in higher Landau levels of graphene. *Nat. Phys.*, 15(2):154, 2019.

[139] M. S. Hossain, M. K. Ma, Y. J. Chung, L. N. Pfeiffer, K. W. West, K. W. Baldwin, and M. Shayegan. Unconventional anisotropic even-denominator fractional quantum Hall state in a system with mass anisotropy. *Phys. Rev. Lett.*, 121:256601, 2018.

[140] J. Xia, J. P. Eisenstein, L. N. Pfeiffer, and K. W. West. Evidence for a fractionally quantized Hall state with anisotropic longitudinal transport. *Nat. Phys.*, 7(11):845, 2011.

[141] Yang Liu, S. Hasdemir, M. Shayegan, L. N. Pfeiffer, K. W. West, and K. W. Baldwin. Evidence for a 5/2 fractional quantum Hall nematic state in parallel magnetic fields. *Phys. Rev. B*, 88:035307, 2013.

[142] G. Gamez and K. Muraki. $\nu = 5/2$ fractional quantum Hall state in low-mobility electron systems: Different roles of disorder. *Phys. Rev. B*, 88:075308, 2013.

[143] M. Samani, A. V. Rossokhaty, E. Sajadi, S. Lüscher, J. A. Folk, J. D. Watson, G. C. Gardner, and M. J. Manfra. Low-temperature illumination and annealing of ultrahigh quality quantum wells. *Phys. Rev. B*, 90:121405, 2014.

[144] X. Fu, A. Riedl, M. Borisov, M. A. Zudov, J. D. Watson, G. Gardner, M. J. Manfra, K. W. Baldwin, L. N. Pfeiffer, and K. W. West. Effect of illumination on quantum lifetime in GaAs quantum wells. *Phys. Rev. B*, 98:195403, 2018.

[145] Q. Shi, M. A. Zudov, B. Friess, J. Smet, J. D. Watson, G. C. Gardner, and M. J. Manfra. Apparent temperature-induced reorientation of quantum Hall stripes. *Phys. Rev. B*, 95:161404, 2017.

[146] Ken Cooper. *New Phases of Two-Dimensional Electrons in Excited Landau Levels*. PhD thesis, California Institute of Technology, 2003.

[147] X. Fu, Y. Huang, Q. Shi, B. I. Shklovskii, M. A. Zudov, G. C. Gardner, and M. J. Manfra. Hidden quantum Hall stripes in $Al_xGa_{1-x}As/Al_{0.24}Ga_{0.76}As$ quantum wells. *Phys. Rev. Lett.*, 125:236803, 2020.

[148] A. P. Smith, A. H. MacDonald, and G. Gumbs. Quasiparticle effective mass and enhanced g factor for a two-dimensional electron gas at intermediate magnetic fields. *Phys. Rev. B*, 45:8829, 1992.

[149] Y. Kwon, D. M. Ceperley, and Richard M. Martin. Quantum Monte Carlo calculation of the fermi-liquid parameters in the two-dimensional electron gas. *Phys. Rev. B*, 50:1684, 1994.

[150] Y. Zhang and S. Das Sarma. Density-dependent spin susceptibility and effective mass in interacting quasi-two-dimensional electron systems. *Phys. Rev. B*, 72:075308, 2005.

[151] R. Asgari, B. Davoudi, M. Polini, Gabriele F. Giuliani, M. P. Tosi, and G. Vignale. Quasiparticle self-energy and many-body effective mass enhancement in a two-dimensional electron liquid. *Phys. Rev. B*, 71:045323, 2005.

[152] R. Asgari and B. Tanatar. Many-body effective mass and spin susceptibility in a quasi-two-dimensional electron liquid. *Phys. Rev. B*, 74:075301, 2006.

[153] N. D. Drummond and R. J. Needs. Quantum Monte Carlo calculation of the energy band and quasiparticle effective mass of the two-dimensional fermi fluid. *Phys. Rev. B*, 80:245104, 2009.

[154] W. Kohn. Cyclotron resonance and de Haas-van Alphen oscillations of an interacting electron gas. *Phys. Rev.*, 123:1242, 1961.

[155] P. T. Coleridge. Small-angle scattering in two-dimensional electron gases. *Phys. Rev. B*, 44:3793, 1991.

[156] M. Hayne, A. Usher, J. J. Harris, and C. T. Foxon. Exchange enhancement of the Landau-level separation for two-dimensional electrons in GaAs/$Ga_{1-x}Al_xAs$ heterojunctions. *Phys. Rev. B*, 46:9515, 1992.

[157] M. Hayne, A. Usher, J. J. Harris, and C. T. Foxon. Quantum versus semiclassical analysis of the conductivity of two-dimensional electrons in a magnetic field. *Phys. Rev. B*, 56:10446, 1997.

[158] J. D. Watson, G. A. Csáthy, and M. J. Manfra. Impact of heterostructure design on transport properties in the second Landau level of *In Situ* back-gated two-dimensional electron gases. *Phys. Rev. Applied*, 3:064004, 2015.

[159] Q. Shi, M. A. Zudov, J. Falson, Y. Kozuka, A. Tsukazaki, M. Kawasaki, K. von Klitzing, and J. Smet. Hall field-induced resistance oscillations in MgZnO/ZnO heterostructures. *Phys. Rev. B*, 95:041411(R), 2017.

[160] S. Peters, L. Tiemann, C. Reichl, and W. Wegscheider. Gating versus doping: Quality parameters of two-dimensional electron systems in undoped and doped GaAs/AlGaAs heterostructures. *Phys. Rev. B*, 94:045304, 2016.

[161] Q. Zhang, T. Arikawa, E. Kato, J. L. Reno, W. Pan, J. D. Watson, M. J. Manfra, M. A. Zudov, M. Tokman, M. Erukhimova, A. Belyanin, and J. Kono. Superradiant decay of cyclotron resonance of two-dimensional electron gases. *Phys. Rev. Lett.*, 113:047601, 2014.

[162] Q. Qian, J. Nakamura, S. Fallahi, G. C. Gardner, J. D. Watson, and M. J. Manfra. High-temperature resistivity measured at $\nu = \frac{5}{2}$ as a predictor of the two-dimensional electron gas quality in the $n = 1$ Landau level. *Phys. Rev. B*, 95:241304, 2017.

[163] G. W. Martin, D. L. Maslov, and M. Yu. Reizer. Quantum magneto-oscillations in a two-dimensional fermi liquid. *Phys. Rev. B*, 68:241309, 2003.

[164] Y. Adamov, I. V. Gornyi, and A. D. Mirlin. Interaction effects on magneto-oscillations in a two-dimensional electron gas. *Phys. Rev. B*, 73:045426, 2006.

[165] X. L. Lei and S. Y. Liu. Radiation-induced magnetoresistance oscillation in a two-dimensional electron gas in faraday geometry. *Phys. Rev. Lett.*, 91:226805, 2003.

[166] Y. M. Beltukov and M. I. Dyakonov. Microwave-induced resistance oscillations as a classical memory effect. *Phys. Rev. Lett.*, 116:176801, 2016.

[167] K. B. Cooper, M. P. Lilly, J. P. Eisenstein, T. Jungwirth, L. N. Pfeiffer, and K. W. West. An investigation of orientational symmetry-breaking mechanisms in high Landau levels. *Solid State Commun.*, 119:89, 2001.

[168] L. Pfeiffer, K. W. West, H. L. Stormer, and K. W. Baldwin. Electron mobilities exceeding $10^7 \mathrm{cm}^2/\mathrm{Vs}$ in modulation-doped GaAs. *Appl. Phys. Lett.*, 55:1888, 1989.

[169] M. Hayne, A. Usher, J. J. Harris, V. V. Moshchalkov, and C. T. Foxon. Remote impurity scattering in modulation-doped GaAs/$\mathrm{Al}_x\mathrm{Ga}_{1-x}$As heterojunctions. *Phys. Rev. B*, 57:14813, 1998.

[170] T. Baba, T. Mizutani, and M. Ogawa. Elimination of persistent photoconductivity and improvement in Si activation coefficient by Al spatial separation from Ga and Si in Al-Ga-As:Si solid system – a novel short period AlAs/n-GaAs superlattice. *Jpn J Appl Phys*, 22:L627, 1983.

[171] L. Pfeiffer and K. W. West. The role of MBE in recent quantum Hall effect physics discoveries. *Physica E Low Dimens*, 20:57, 2003.

[172] V. Umansky, M. Heiblum, Y. Levinson, J. Smet, J. Nübler, and M. Dolev. MBE growth of ultra-low disorder 2Deg with mobility exceeding $> 35 \times 10^6 \mathrm{cm}^2/\mathrm{Vs}$. *J. Cryst. Growth*, 311(7):1658, 2009.

[173] G. C. Gardner, S. Fallahi, J. D. Watson, and M. J. Manfra. Modified MBE hardware and techniques and role of gallium purity for attainment of two dimensional electron gas mobility $> 35 \times 10^6 \mathrm{cm}^2/\mathrm{Vs}$ in AlGaAs/GaAs quantum wells grown by MBE. *J. Cryst. Growth*, 441:71, 2016.

[174] M. Sammon, T. Chen, and B. I. Shklovskii. Excess electron screening of remote donors and mobility in modern GaAs/AlGaAs heterostructures. *Phys. Rev. Materials*, 2:104001, 2018.